



UNIVERSITÀ DEGLI STUDI DI NAPOLI
FEDERICO II



UNIVERSITÀ DEGLI STUDI DI NAPOLI FEDERICO II

PH.D. THESIS IN

INFORMATION TECHNOLOGY AND ELECTRICAL ENGINEERING

**MODELLING OF POWER EXHAUST
IN FUSION PLASMAS**

VINCENZO PAOLO LOSCHIAVO

MARCH 2017

TUTOR: PROF. RAFFAELE ALBANESE

CO-TUTOR: PROF. ROBERTO AMBROSINO

XXIX CICLO

**SCUOLA POLITECNICA E DELLE SCIENZE DI BASE
DIPARTIMENTO DI INGEGNERIA ELETTRICA E TECNOLOGIE DELL'INFORMAZIONE**

Acknowledgements

I want to thank, from the bottom of my heart:

- my tutor, Prof. Eng. Raffaele Albanese for the big opportunity that once more he gave me with the PhD. I thank him for the courteousness, constancy and professionalism used during the last three years to lead me, but above all for the passion he proves every day for his job;
- Prof. Eng. Roberto Ambrosino, my co-tutor, for his kindness and professionalism. It was a pleasure to work with him and I am really grateful to him for the huge professional and moral support;
- the EUROfusion PPPT PMU team, in the person of Dr. Francesco Maviglia, Dr. Ronal Wenninger, Dr. Gianfranco Federici and Dr. Eberhard Diegele for having been extraordinary “landlords” during the months spent in Garching (Germany). I am really thankful for the opportunity to work with them;
- Dr. Davide Bernardi, ENEA Brasimone, always kind and willing. The interactions with him resulted in productive collaborations on the thermo-mechanical tasks;
- Prof. Dr. Marco de Baar and Prof. Dr. Rudolf Neu for the comments and suggestions provided during the revision of this thesis. They spurred me to clarify some concept and, following their suggestions, the thesis resulted more harmonious than in the previous draft;
- Prof. Massimiliano de Magistris, who always supported me during the PhD. He has been always kind and willing. It is always a pleasure to discuss with him not only of academic matter;
- CREATE Consortium and in particular Prof. Vincenzo Coccoresse;

ii

- Prof. Daniele Riccio, Coordinator of the Information Technology and Electrical Engineering PhD course. He has been always courteous and willing;
- all the many contributors I was involved with in submitting scientific papers.

Moreover, thanks to my colleagues Dr Simone Minucci, Dr. Soudeh Yaghouti (Negin), Dr. Salvatore Perna. Dr. Angelo Ambrisi and the others who shared with me the PhD path.

Finally, special thanks go to those who have made all this possible. I thank my father and my mother for the love they always gave me unconditionally, the source of my certainty and my serenity. I dedicate this thesis to my father, in the hope that, although he is no longer among us, wherever he is, he can look me and being proud of me.

I thank my mother, my brother and my aunt for the patience and affection they always prove for me, especially in the difficult moments.

I thank Graziella, my love, for having changed my life. She is my reason for leaving and the source of my strength. Thanks for existing.

A handwritten signature in black ink, appearing to read "Simone Sabatini", is positioned in the bottom right corner of the page. The signature is written in a cursive, flowing style.

Table of contents

Chapter 1

Fusion.....	1
1.1 What is nuclear fusion?.....	4
1.2 The plasma	7
1.3 The plasma physics	8
1.3.1 Lawson criterion	9
1.4 Plasma confinement techniques	11
1.4.1 Evolution of the plasma magnetic confinement techniques.....	14
1.5 The tokamak.....	15
1.5.1 Plasma configurations.....	20
1.6 Plasma heating	24
1.6.1 Main plasma heating.....	24
1.6.2 Additional heating techniques	24
1.7 Energy production in a thermonuclear power plant.....	27
1.8 The present and future of the fusion: from Jet to DEMO through ITER and DTT	30

Chapter 2

The plasma-surface interactions	39
2.1 The plasma sheath.....	39
2.2 Ion/Atom Back-scattering and Recycling	43
2.3 Atomic and molecular processes	45
2.4 Sputtering	48
2.4.1 Physical sputtering.....	49
2.4.2 Chemical sputtering.....	50
2.4.3 Choice of materials	51
2.5 Radiation Losses and Impurity Radiation.....	52

2.6	Conclusions	54
Chapter 3		
	The power exhaust	57
3.1	The plasma exhaust	57
3.2	The scrape-off layer	59
3.2.1	A simple SOL/divertor model.....	59
3.2.2	Radial transport and widths	61
3.2.3	Parallel transport	63
3.2.4	Solution of plasma equations	65
3.2.5	Two-Point Model	66
3.3	Plasma operative regimes.....	69
3.3.1	Sheath-Limited Regime	70
3.3.2	Detached regime	70
3.3.3	High recycling regime	71
3.3.4	Comparison with the experimental results.....	73
3.4	Conclusions	73
Chapter 4		
	The candidate solutions to the power exhaust issue.....	77
4.1	The plasma “detachment”	78
4.2	The alternative magnetic divertor configurations	80
4.2.1	Double-Null (DN) configuration	80
4.2.2	X-Divertor (XD) configuration.....	81
4.2.3	Snowflake Divertor (SFD).....	83
4.2.4	Super-X Divertor (SXD).....	84
4.2.5	Effects of the advanced magnetic configurations on the detachment front stability	85
4.3	The strike-point sweeping and the wobbling techniques .	86
4.4	The liquid metal divertor.....	87
Chapter 5		
	DEMO magnetic alternative configurations design and vertical stability analysis	93
5.1	Theoretical basis.....	94

5.1.1	Magnetohydrodynamic model (MHD).....	94
5.1.2	Ideal MHD.....	97
5.1.3	The equilibrium problem.....	98
5.1.4	Grad-Shafranov equation.....	99
5.2	The free boundary dynamic plasma equilibrium problem	102
5.2.1	An overview of plasma equilibrium simulation codes	103
5.2.2	CREATE-NL+ code	105
5.3	DEMO alternative magnetic configurations design.....	108
5.3.1	PF coil system design constraints.....	109
5.3.2	PF coil system optimization procedure	110
5.3.3	Examples	114
5.4	DEMO alternative configurations Vertical Stability (VS)	analysis
		115
5.4.1	DEMO Single-Null (SN) and Double-Null (DN)	reference equilibria definition
		116
5.4.2	Single-Null perturbed plasma equilibria (development	of the first wall contour).....
		120
5.4.3	DEMO baseline SN and DN Vertical Stability Analysis	123
5.4.4	A DEMO SN-DN “fair comparison”.....	130
5.5	Conclusions.....	133
Chapter 6		
	DEMO divertor target tiles 2D and 3D thermo-mechanical analyses	in the strike-point sweeping case
		137
6.1	The strike-point sweeping technique	138
6.1.1	A preliminary assessment of the sweeping power	requirements and AC losses in DEMO
		139
6.2	Strike-point sweeping 2D thermal analysis	141
6.2.1	Model assumptions	142
6.2.2	Thermal analysis.....	145

6.3	Strike-point sweeping 3D thermo-mechanical analysis .	155
6.3.1	Model assumptions	155
6.3.2	Thermo-mechanical analysis	161
6.4	DEMO DN wobbling: a preliminary analysis.....	168
6.5	Final considerations and further developments.....	172

Synopsis

This PhD thesis deals with the thorny problem of “Modelling of power exhaust in fusion plasmas”, a challenge concerning the development of a system able to withstand the large loads expected in the fusion power plant divertor. Since first days of PhD course, my tutor spurred me to face this challenging mission within the European Roadmap to the next-generation fusion devices, encouraging me to look beyond the state-of-the-art and to think differently.

The outline of the thesis mainly reflects chronologically the path covered within PhD course:

- Chapter 1 mainly represents my background, achieved during the bachelor and master degrees; as winner of a grant promoted by Italian Embassy in London, I had the opportunity to spend in 2013 three months in Culham (UK) at the JET (Joint European Torus), the greatest working fusion experimental device;
- Chapter 2 and 3 report the key concepts modelling the behaviour of the plasma during plasma-surface interactions and describing the power exhaust; both topics are central in the development of this thesis and more in general of whole research activity during the PhD course;
- Chapter 4 is an overview of the state-of-the-art in the research field on power exhaust; the candidate solutions to the power exhaust issue are described starting from the baseline solution for ITER reactor;
- Chapter 5 describes, after a brief introduction on theoretical basis of the plasma boundary reconstruction, my main contributions in the design and vertical stability analysis of plasma alternative magnetic configurations for the DEMO nuclear fusion power station;
- Chapter 6 presents an assessment of the DEMO divertor target tiles lifetime in case of strike-point sweeping; this technique is one of the most promising candidate solution to the power exhaust issue but its main drawback is related to the periodical heating and cooling of the plasma facing components inducing the thermal-fatigue phenomenon. To evaluate the lifetime of the DEMO

viii

divertor target tiles, different 2D and 3D thermo-mechanical models are presented. Finally, a preliminary analysis on the wobbling technique applied to a DEMO Double Null plasma magnetic configuration is illustrated.

Chapter 1

“I ask you to look both ways. For the road to a knowledge of the stars leads through the atom; and important knowledge of the atom has been reached through the stars.”

Sir Arthur Eddington, Stars and Atoms (1928), Lecture 1

Fusion

Introduction

Since the humankind dawn, welfare and development have been closely related to the availability of energy. Throughout history, starting from the pre-history up to our era, the consumption of energy grew up with a very high rate, especially in the last three centuries:

- in the prehistory, man consumed only the energy needed to feed on, about 2500 kcal (i.e. a glass of oil), which is equivalent to the energy still used today to feed on;
- with the discovery of fire and thus the beginning of cooked foods, consumption doubled, reaching 5000 Kcal per day;
- with the beginning and development of the agricultural age, it was necessary to transport goods over significant distances and to use oxen to plough fields, arriving to an energy consumption per person of about 4 times the one needed to just feed on (10000 Kcal/day).

The great leap was made with the industrial revolution (between the end of 1700 and beginning of 1800), after which, with the discovery of the steam engine, the consumption increased by a factor of twenty compared to the one needed only to eat (50000 Kcal/day). Within less than two centuries, the exponential growth resulted, at least in the industrialized countries, in an average consumption of 150000 Kcal/day per person (approximately 600 MJ/day). The most recent estimates state that in 2012 the total annual energy consumption reached almost 12

Gtoe¹; dividing these 12 billion tonne of oil equivalent for nearly 7 billion (the world population) we get a consumption of about 1.8 toe/inhabitant per year (or about 18 million Kcal). If the whole requirement would be covered with oil consumption, it would correspond to the load of about 100 supertankers per day (each one carrying 2 million barrels).

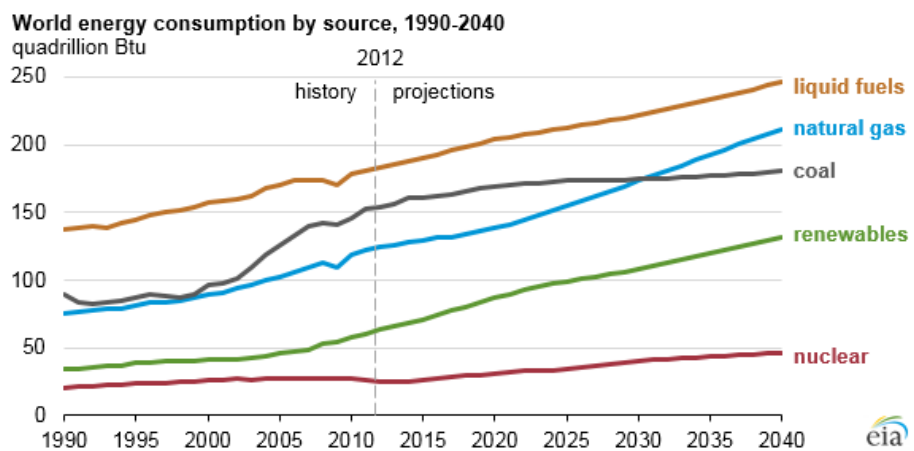


Figure 1.1: World energy consumption by source - EIA² [1.1]

However, oil is not the only source of energy by which fulfil the annual world demand (thankfully!)

Why the fusion?

The energy demand per person is increasing due to the constant increase of both the world population and the demand per person. In particular, according to the International Energy Outlook 2013 (IEO 2013), published on July 25 2013 by the Energy Information Administration (EIA) of the US government, "...over the next three decades, the world

¹ The tonne of oil equivalent (toe) is a unit of energy defined as the amount of energy released by burning one tonne of crude oil. It is approximately 42 gigajoules, although as different crude oils have different calorific values, the exact value is defined by convention; several slightly different definitions exist.

² "EIA" is the independent statistics and analysis Department of the U.S. Energy Information Administration.

energy consumption is expected to increase by 56%, driven by growth in the developing world.”

Currently, the basic sources used worldwide for the supply of such energy are represented by coal, around 28%, and especially by oil, for about 34%; natural gas is the third source, in order of importance, and it is interesting to note that its contribution has steadily and rapidly grown over the past two decades (**Figure 1.1**). Therefore, the three main primary sources are all fossil and hence non-renewable (“non-renewable” means that the sources are exploited at a rate higher than the natural renewal rate) and the deposits of these fossil fuels are continuing decrease. The most optimistic estimates predict that the availability of non-renewable energy sources (such as coal, oil and natural gas) can last at most a few hundred years.

Next to the non-renewable sources, there are the so-called “renewable” sources. Among these sources, there is the nuclear power that matches a great demand for energy, about 5%, being the source grown faster in the last thirty years, with a very large penetration, until the early 80’s, reducing, in the same period, the use of oil by about 10%. Later, this development has almost stopped and even now, many European countries (such as Germany) are planning to abandon their nuclear power plants, because of the management problems, especially related to the waste (these problems affect widely nuclear fission power plants).

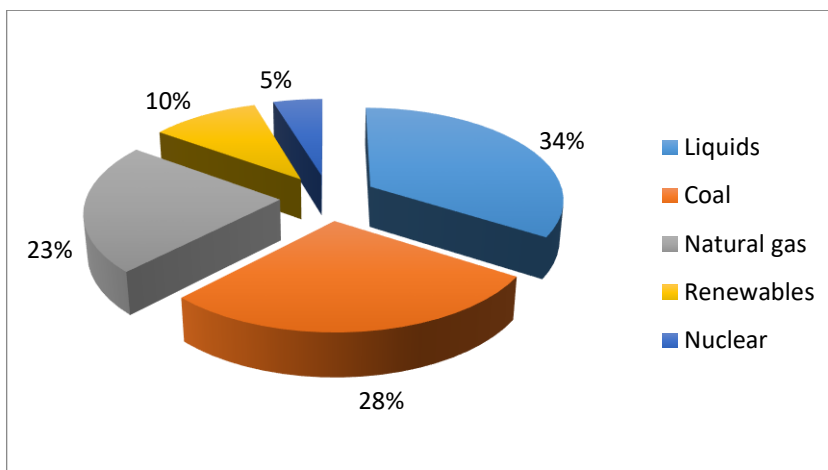


Figure 1.2: Energy consumption based on source type.

The remaining percentage, related to the renewable sources, is unfortunately less significant (**Figure 1.2**). These sources are very abundant, non-polluting and inexhaustible but it is difficult to put them at the base of the energy supply, both for their lack of constancy, and because the current technologies suited to exploit them are expensive and do not allow to have a good energy efficiency. Among these sources, there are biomass, 4%, hydropower, 3%, solar energy, 0.5%, and so on towards even smaller percentage.

To face a world energy demand constantly growing and an extinction, at even more rapid rate, of all major fossil energy (non-renewable) sources, research is focusing more and more on renewables and on new fields as the nuclear fusion. Nuclear fusion is seen as one of the answers to the worldwide energy issues: it is clean, safe and sustainable and does only produce short-living radioactive waste: it is the energy source of the Sun and stars.

The scientific results and continue progress achieved so far in the experimental nuclear fusion field suggest that it will be possible to produce fusion power since the middle of this century. In particular, Europe has become the world leader in the field of fusion through the construction of several experimental machines. The largest experimental machine in the world currently operating is the Joint European Torus (JET) in Culham, whose best result so far achieved (1997) has been producing 16 MW of fusion power, with a fusion energy gain factor Q of about 0.5.

1.1 What is nuclear fusion?

Fusion is the nuclear reaction process by which two nuclei are compressed so that the strong interaction prevails on the electromagnetic repulsion, forming a single more massive nucleus. The fusion is an exo-energetic reaction, emitting more energy than the one required for the compression, up to atomic numbers 26 and 28 (i.e. Iron and Nickel); beyond that limit, it is endo-energetic, absorbing energy. For this reason, the hydrogen or its isotopes are the starting elements for a fusion process (atomic number $Z = 1$).

The nuclear fission is the reaction through which, starting from a heavier atom two lighter atoms are obtained by a process of

bombardment with neutrons or elementary particles. It is an exo-energetic process for “heavy elements”, i.e. atomic number higher than Iron and Nickel (usually uranium and plutonium, whose atomic numbers are respectively 235 and 239, are used), and endo-energetic for lighter elements.

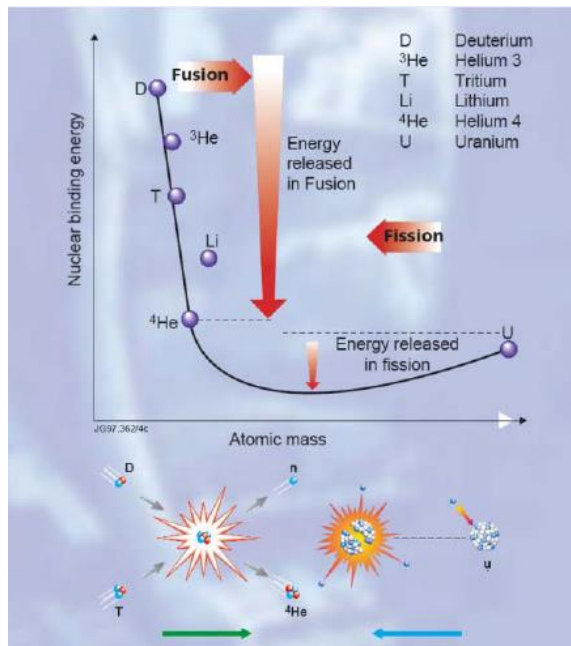


Figure 1.3: energy release through fusion and fission.

Therefore, nuclear reactions release (exothermic) and absorb (endothermic) energy. This amount of energy can be expressed, according to the “theory of relativity” by Albert Einstein, by the famous expression:

$$\Delta E = \Delta M c^2$$

The energy released is proportional to the mass defect ($\Delta M = M_{initial} - M_{final}$) between the initial mass of reactants $M_{initial}$ and the product final one M_{final} . For equal quantities of reactive substances, a fusion reaction produces an energy much greater than that obtained by classical chemical reactions (such as combustion).

The reaction of interest in nuclear environment is the fusion of deuterium (D or ^2H) and tritium (T or ^3H). This reaction is the most

simple to implement (**Figure 1.4**) and the most efficient for the purpose of energy production.

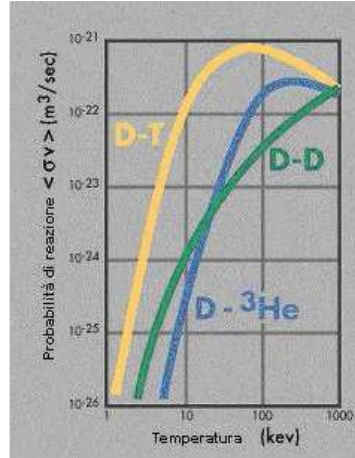


Figure 1.4: reaction probability for different types of fuel.

Deuterium and Tritium are two hydrogen isotopes and in particular, while hydrogen is formed by an electron and a proton, the deuterium has also a neutron whereas the tritium has two neutrons; in other words, the core of all three contains a proton ($Z = 1$), which characterizes them as forms of hydrogen element. When Deuterium and Tritium are forced to join³, they produce a nucleus of an isotope of helium (${}^4\text{He}$), also called “alpha particle”, carrying, in the form of kinetic energy, 1/5 of the total energy produced in the reaction (3.5 MeV ⁴) and the release of a neutron, which carries the remaining 4/5 (14.1 MeV). **Figure 1.5** briefly summarizes the fusion reaction described (the red balls represent protons whereas neutrons are represented by the blue ones).

³ Deuterium and Tritium can be forced to join in different ways, analysed in the following; in a thermonuclear fusion, the extremely high temperatures are used for the aim.

⁴ The definition of temperature for hot systems comes out from the kinetic theory of ideal gases ($E=3/2 kT$). The temperature is related through the average of the kinetic energy to the degree of thermal agitation of the system. By multiplying the temperature with the Boltzmann constant one formally gets $1\text{eV} \sim 11600\text{K}$.

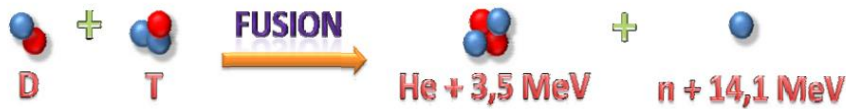


Figure 1.5: Deuterium-Tritium reaction scheme.

It is worth to say that the deuterium is abundant in the seawater while the tritium, radioactive material with a half-life of 12.3 years, does not exist in appreciable quantities in nature and must therefore be generated.

1.2 The plasma

In order to obtain a fusion reaction, the Deuterium and Tritium atoms must be forced to join. The two nuclei interact only at very small distances, equivalent to the size of the atomic nucleus ($10^{-13}cm$); at this distance, the nuclear forces are predominant on the electrostatic repulsion due to the positive charge of the nuclei (forces that grow moving closer the nuclei in inverse proportion to the square of the distance). To bring the two nuclei at sufficiently short distances, the speed with which they collide and therefore their kinetic energy (and temperature) must be very high.

Different methods have been used in the past trying to achieve this particles high speed. However, the most promising technique, therefore used on the modern devices for triggering these fusion reactions is the heating of the fuel (Deuterium and Tritium) at extremely high temperature for a sufficiently long confinement time in a confined environment. In this way, the nuclei have enough time to collide with each other, thus increasing the probability of giving rise to fusion reactions, without energy dispersion.

The fusion obtained in this way is defined *thermonuclear fusion*.

In this case, to get in the lab such controlled thermonuclear fusion, with a positive energy balance, it is necessary to heat a mixture of Deuterium-Tritium at extremely high temperatures, around 100 million degrees Celsius (more than six times the temperature of the solar core!).

At such temperature, the fuel is fully *ionized* and this is the reason why it is no longer called gas but instead *plasma*.

In a gas at ordinary temperature, the particles are neutral; vice versa, at temperatures higher than a few eV, since the particles tend to split into their components (ions and electrons) the gas is transformed into a mixture of charged particles, called plasma, even if it still remains globally neutral.

In 1928, the American scientist Irving Langmuir suggested that electrons, protons and other ions in an ionized gas could be regarded as the corpuscles that are dragged into a kind of fluid that he defined as “*plasma*”.

The plasma constitutes the 99% of the matter of Universe being often defined as the *fourth state of matter* (substantially resorting the theories of Empedocles). It is, also, the main constituent of the stars. Today everyone commonly deals with plasmas, e.g. the neon or the fluorescent lamps.

The density⁵ of the plasmas varies between 10^0 (intergalactic medium) and $10^{32} m^{-3}$ (inertial confinement plasma).

Plasmas faced in this thesis are just those produced during a fusion process.

1.3 The plasma physics

Once the Deuterium-Tritium plasma reaches 100 million degrees⁶, it must be kept confined in a limited space, with a confinement good enough to provide time for a sufficiently large number of collisions, allowing the energy released by the fusion reactions to compensate both the losses and the external energy.

In other words, it is necessary to satisfy the conditions expressed by the Lawson criterion, conditions depending on the plasma temperature.

⁵ Density here means the number of particles per cubic meter. It is useful to compare this density to that of the air which, under standard conditions, is $\sim 2.7 \cdot 10^{25} m^{-3}$.

⁶ Given the order of magnitude of these temperatures, it is unnecessary to specify whether they are expressed in °C or K.

1.3.1 Lawson criterion

The Lawson criterion is a criterion formulated by the English engineer and physicist John D. Lawson around 1955 to characterize the set of parameters that allows a fusion reactor to *produce more energy than the one it absorbs*.

It comes out from a fundamental question in the design of a reactor, and more in general it is valid for all the sources of energy: *the system produces more energy than the one requested for maintaining the reaction active?*

The energy balance for the plasma can be determined by considering the energy sources that feed it and the losses that lower the temperature. In order to keep plasma in stationary conditions, the sources must balance the losses.

The fusion power P_{fusion} produced by the D-T reactions is given by the sum of the power of reaction products: neutrons and alpha particles (or helium nuclei).

$$P_{fusion} = P_{alpha} + P_{neut}$$

The charged alpha particles are affected by the magnetic field applied to achieve the confinement, remaining within the plasma and transferring energy to the other particles through collisions. Conversely, the neutrons not undergoing the action of the field move quickly away without being able to transfer their energy to the plasma reaching the plasma facing components and penetrating into their volume.

The magnetic confinement of the plasma (Section 1.4) is not perfect; therefore, particles and heat diffuse outside from the plasma core. The losses due to heat and particles transport are considerable. As a hot body, the plasma also cools by radiation. If the energy produced by the reaction is not sufficient to compensate the losses, it is necessary to introduce external energy to maintain the plasma in its state. The power supplied from the outside will be indicated with $P_{external}$ whereas P_{losses} will indicate the leaks. The energy balance could be written as:

$$\frac{dW}{dt} = P_{alpha} + P_{external} - P_{losses}$$

The left hand side (LHS) considers the plasma energy W time variation. If the applied power exceeds losses ($\frac{dW}{dt} > 0$), the plasma energy increases; in the opposite case ($\frac{dW}{dt} < 0$) it decreases. Finally, if the sources exactly compensate the losses ($\frac{dW}{dt} = 0$), the plasma is in steady-state conditions.

Following, the definition of some plasma physics relevant parameters is provided:

- the *energy confinement time* (τ_E) is the average time taken for the energy to escape the plasma, usually defined as the total amount of energy stored in the plasma divided by the rate at which energy is lost:

$$\tau_E = \frac{W}{P_{losses}}$$

- the *fusion energy gain factor* (Q), is the ratio of fusion power produced in a nuclear fusion reactor to the power required to maintain the plasma in steady state:

$$Q = \frac{P_{fusion}}{P_{external}}$$

Three distinct situations may occur depending on the value of the fusion energy gain factor:

- $Q < 1$: fusion power is less than the external power; this situation summarizes the current state of the art in thermonuclear fusion, whose best result was achieved at JET with 16 MW of fusion power produced from about 24 MW input power and $Q \cong 0.7$.
- $Q = 1$: fusion power is equal to the external power. This condition is referred to as “*breakeven*”.
- $Q > 1$: fusion power is higher than the external power. At the limit, Q could become also infinite; at this condition, the fusion reaction is self-sustaining since the plasma heats itself by fusion energy without any external input ($P_{external} = 0$). In such conditions, the so-called “*plasma ignition*” takes place: the alpha particles,

confined by the magnetic field, transfer their energy to the plasma allowing it to reach, after the initial heating by external sources, the ignition point; from this point the thermonuclear reaction goes on alone. Meanwhile, neutrons transfer their energy to the reactor shell (consisting essentially of lithium), generating tritium (or regenerating it, as previously mentioned), and transforming their kinetic energy into heat exploitable to produce electricity.

The Lawson criterion states that the power obtained from the fusion will be greater than the input power into the reactor as soon as the triple product density (n), the confinement time (τ_E) and temperature (T) exceeds a certain value, itself function of the plasma temperature. This figure of merit is defined “*triple product*” of density, temperature, and confinement time. In particular, characterizing this criterion for the situation in which one has the ignition, i.e. $Q = \infty$, and for a temperature between 10 and 20 keV, it results:

$$n \cdot T \cdot \tau_E \geq 2.6 \cdot 10^{21} \text{ keV s m}^{-3}$$

This figure of merit has become over the years a fundamental expression that must be met by fusion reactors (reactors are designed taking into account it): it means that, essentially, the particles must be many (high density), very energetic (high temperature), and stay together for a sufficient time (high confinement time) to give a sufficient amount of fusion power. Although obtaining significant values of one of the three parameters has been achieved in present day devices, getting all three at the same time is a difficult task.

Furthermore, the problem of how to confine the plasma within physical walls to such high temperatures remains.

1.4 Plasma confinement techniques

There are different plasma confinement techniques:

- *gravitational confinement*: it is based on gravitational interaction property whereby each mass creates an attractive force on another mass. Gravitational forces within the stars, for example, maintain the matter (essentially hydrogen) compressed allowing it to reach very high densities and temperatures. Thanks to this gravitational

field, nuclear reactions could occur generating thermal expansion forces capable of balancing the compression action of gravity. For this reason, it is usual to say that the stars regulate themselves; if, for example, the speed of the fusion reactions grows, the star would expand thus slowing down the reactions. The Sun density (n) is much higher than the one obtainable experimentally on Earth and hence the temperature needed to reach the ignition on the Sun is much lower (10 -15 million degrees in the Sun, 100 million degrees on Earth). Simple mathematical calculations, in fact, show that the nuclear fuel mass necessary to create a star (based on the D-D reaction) on Earth is approximately similar to the mass of the Moon. The gravitational confinement is therefore impossible to achieve on Earth.

- *inertial confinement*: it is a method in which a pellet, with a few mm diameter, consisting of deuterium and tritium, of about 10 mg, is quickly radiated from several high-power laser beams or atomic nuclei compressing and heating it. The pellet then ablates, producing a reaction force on the remaining part whereby its particles are re-accelerated inwards making possible the occurrence of fusion reactions (**Figure 1.6**). The main challenge is to achieve powerful and homogenous irradiation of high frequency pellet: about 10-20 pellets per second must be heated and burned in a typical reactor. However, this technique has been for a long time under military secrecy because it is the principle of the hydrogen bomb. In a hydrogen bomb, a powerful explosion caused by a nuclear fission bomb generates a series of X-rays that create a thermal wave propagating in the header and compressing a small cylinder of fusion fuel, usually a mixture of deuterium and tritium, up to a temperature such as to generate the fusion of the nuclei.

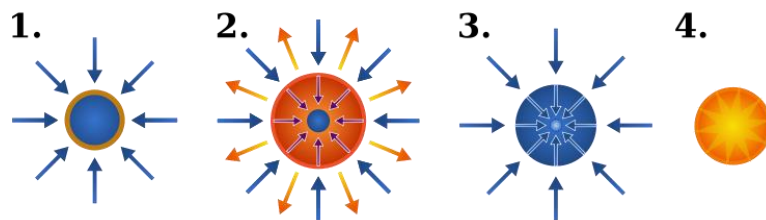


Figure 1.6: Inertial confinement fusion: 1. Heating; 2. Ablation; 3. Compression; 4. Fusion

- **magnetic confinement:** this is the most promising technique in the field of controlled thermonuclear fusion and hence it has been the most studied over the last years. The plasma, being composed of charged particles, namely ions and electrons, is a good conductor of electrical current and can be confined using magnetic fields. Without magnetic fields, the particles would be free to move in any direction, reaching the walls of the container, cooling the plasma and inhibiting the fusion reaction. However, a suitable configuration of the magnetic fields⁷ (**Figure 1.7**) may force the particles to follow helical trajectories around the magnetic field lines, preventing the contact with the walls.

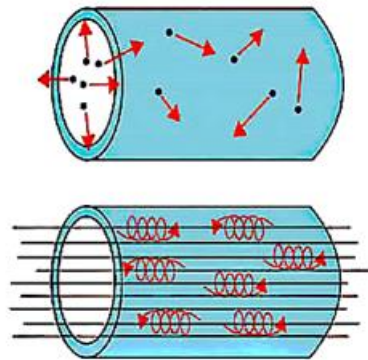


Figure 1.7: Charged particles that move: randomly (up) without a magnetic field; with a helical motion (down) around the field lines in presence of a magnetic field.

In particular, the charged particles in a magnetic field follow a helical path around the magnetic field lines according to the equation of motion taking into account the Lorentz Force, which precisely defines the *Larmor radius* (or *gyroradius*) as:

$$r = \frac{mv}{qB}$$

in which, v is the velocity of the particle perpendicular to the magnetic field, m is its mass, B is the magnetic field and q is the charge of the

⁷ Usually, the magnetic field used in an experimental fusion device is given by the superposition of magnetic fields produced with coils external to the main chamber, and the one produced by the current flowing within the plasma.

ion. The gyration radius of the particle, called Larmor radius, depends on the intensity of the magnetic field, the mass and charge of the particle and its energy. The stronger the magnetic field, the smaller the Larmor radius, the particle staying “stuck” near the field line. Moreover, the electrons, much lighter than the ions, have a much smaller Larmor radius for the same energy. Finally, very energetic particles have a much larger Larmor radius than low energy particles, and are therefore more difficult to confine. The Larmor radius may typically vary from several millimetres for not very energetic particles with an intense magnetic field to tens of centimetres for very energetic particles. The *confinement solution thus consists in closing the magnetic field line on itself to trap the particle.*

All the modern fusion experimental devices resort to plasma magnetic confinement techniques. Therefore, it is useful to analyse, albeit briefly, the evolution over the years of the different magnetic confinement techniques.

1.4.1 Evolution of the plasma magnetic confinement techniques

There are mainly two different plasma magnetic confinement techniques:

- **Magnetic mirrors** represent chronologically the first plasma magnetic confinement technique developed by scientists. It involves an “*open*” *configuration*. The original idea, in fact, was based on the consideration that an electric current generates a magnetic field and the currents flowing in the plasma are able to “pinch” the plasma, keeping it within its magnetic field. However, the magnetic force is two-dimensional and only acts perpendicular to the current direction. Thus, the plasma confined with such devices assumed a cylindrical configuration with obvious loss in correspondence of its ends. In order to reduce these plasma losses, two coils capable to produce a stronger magnetic field near the ends of the tube were introduced (**Figure 1.8**). These coils created a “bottleneck” for the plasma at its ends, thus preventing its escape. The plasma then reflected itself (hence the nickname “mirror”) at the ends thanks to such stronger fields.

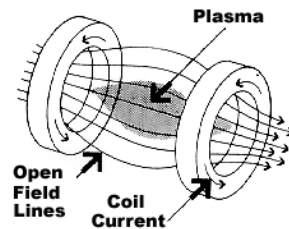


Figure 1.8: magnetic field lines in a "magnetic mirror".

- **Toroidal chamber:** the following idea was to move from a linear, and therefore "open", configuration to a "closed" configuration. This idea led to a toroidal chamber (a sort of donut), hence without any open end, that rather could ensure the continuity of the plasma. Since this confinement technique has been proven to be the most efficient, all the present and future experimental devices are based on this key concept (just take a look at the design of the next generation fusion devices Section 1.8).

1.5 The tokamak

The so-called "tokamak", a Russian acronym for TOroidalnaya kamera ee MAgnitnaya Katushka ("тороидальная камера с магнитными катушками"), which translated literally means "Toroidal Chamber with Magnetic Coils", is nowadays the most used configuration for the plasma confinement.

In this experimental device, the current flowing in the turns of the toroidal field coils surrounding the reactor generates a toroidal magnetic field (**Figure 1.9**).

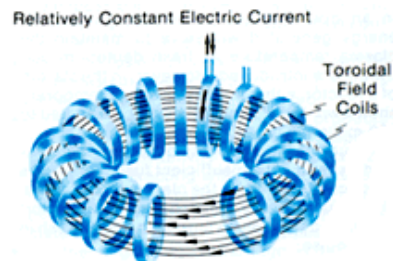


Figure 1.9: Toroidal magnetic field and related coils.

Unlike what happens in the case of magnetic mirrors, this toroidal magnetic field is inversely proportional to the distance from the axis of symmetry of the torus. In fact, considering a torus (which can be thought as a solenoid bent into a donut shape), like the one in **Figure 1.10**:

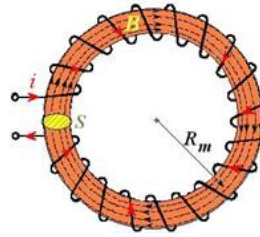


Figure 1.10: Solenoid wound on a toroidal core.

on which N turns are wound, if i is the current flowing through them, by applying the Ampère's law to the generic concentric circumference with R radius, chosen as a closed line, it is:

$$(B_{tor})(2\pi R) = \mu_0 i N$$

and then the toroidal magnetic field B_{tor} is:

$$B_{tor} = \frac{\mu_0 i N}{2\pi R}$$

B_{tor} is inversely proportional to the distance R from the axis of symmetry of the system.

Since a charged particle describes a helical trajectory around magnetic field lines (**Figure 1.11**):

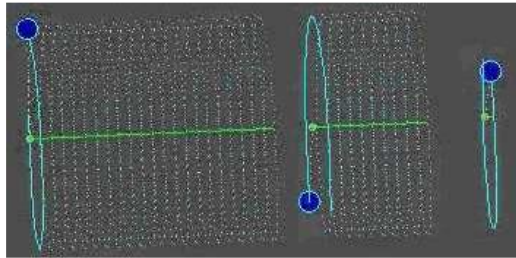


Figure 1.11: Trajectory of a charged particle around a magnetic field line.

on a simple circular trajectory of this type, the particle undergoes a slow cross drift, due to the drift gradient of the magnetic field and centrifugal

force, depending on the sign of its charge. For example, the ions will drift up (as illustrated on the diagram opposite) and the electrons down (**Figure 1.12**).

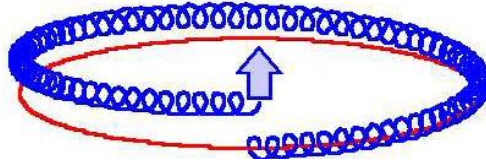


Figure 1.12: positive ion drift.

This suggests that, by itself, the toroidal field is not sufficient to allow the plasma confinement. Therefore, to compensate this effect the idea is to stabilise the configuration by adding a poloidal component to the toroidal magnetic field (**Figure 1.13**). In a tokamak this field, with closed force lines lying in planes perpendicular to the toroidal direction, is produced mainly by a current flowing in the plasma (in the toroidal direction, **Figure 1.13**).

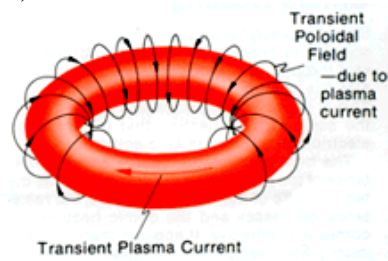


Figure 1.13: Poloidal magnetic field due to the plasma current.

The superposition of toroidal and poloidal magnetic fields produces magnetic field lines that are helices twisted round stacked toroidal surfaces having a helical path around the torus (**Figure 1.14**).

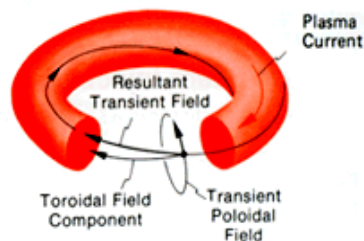


Figure 1.14: Magnetic field line trajectories in the plasma.

A family of nested toroids formed by the magnetic field lines arise. The inner toroid, degenerated into a single closed curve, is defined *magnetic axis*.

Even in this case, the particle undergoes a drift, because of its charge, which distances it from the field line. The particle then spends half its time head upwards, where the vertical drift moves it away from the magnetic surface, and the other half head down, where the vertical drift pulls it back to the magnetic surface. The drift effect is thus on average compensated.

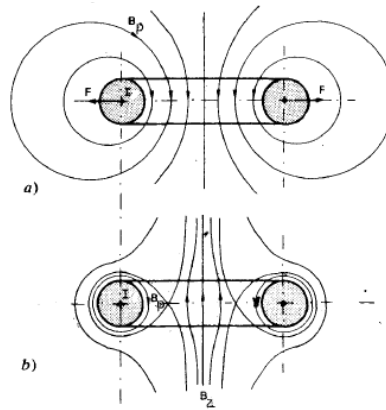


Figure 1.15: Configuration of the poloidal magnetic field
a) before and b) after the application of a vertical field.

A third, vertical magnetic field B_z fixes the position of the current in the plasma and prevent a drifting of the plasma due to the magnetic field gradient from the region of high magnetic field on the inside of the toroid to the region of lower magnetic field on its outside (**Figure 1.15**). The coils generating the vertical field are defined “poloidal field coils” (**Figure 1.16**).

In a tokamak, toroidal and vertical magnetic fields are produced by external coils, whereas the poloidal magnetic field is induced by a current flowing toroidally in the plasma. This plasma current I_p is generated by transformer effect, from a primary circuit of which the secondary, in a single turn, is the plasma. In a tokamak, the “central solenoid” is the magnet that drives the current in the plasma.

Figure 1.16 illustrates the whole structure of a tokamak.

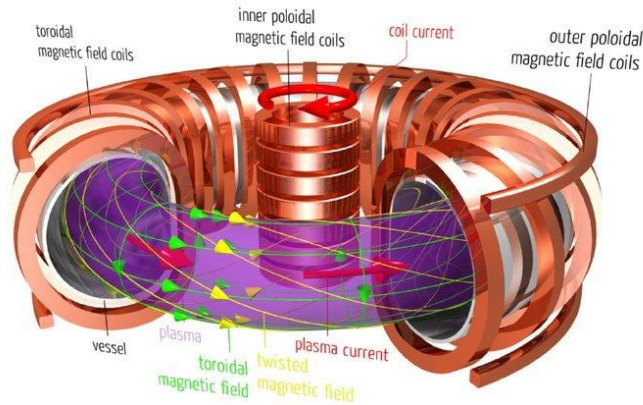


Figure 1.16: Coils and magnetic fields in a Tokamak.

Another magnetic confinement configuration is the “stellarator”, in which the magnetic field is provided completely by external toroidal as well as poloidal coils. In this experimental device, in addition to the standard toroidal coils, helical windings around the vacuum chamber that contains the plasma are employed. These additional windings (**Figure 1.17**) create a helical magnetic field in the toroidal chamber.

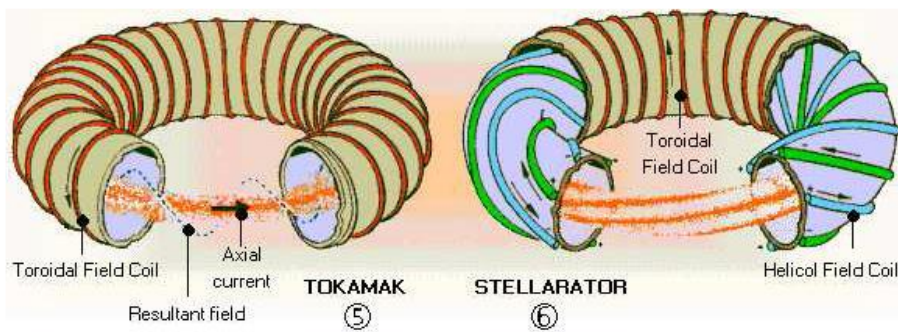


Figure 1.17: Comparison between tokamak and stellarator.

The fact of not having an intense current flowing in the plasma is an advantage in the event of *plasma disruptions*⁸, but the drawback is the

⁸ A disruption is a violent event that terminates a magnetically confined plasma, usually the consequence of a rapidly growing instability, often of the MHD type. In a disruption, the temperature drops drastically and heat and particles are released from confinement on a short timescale and dumped on the vessel wall, causing damage in

complexity of the necessary magnetic coils. Moreover, a tokamak operates in a pulsed mode since the plasma current is generated by transformer effect; the pulse duration is thus limited by the capacity of the primary circuit generating the plasma current. Conversely, a stellarator can operate continuously, since the fields come entirely from external coils and there is no plasma current.

1.5.1 Plasma configurations

In the magnetic confinement devices, in order to reduce the entry of impurities into the plasma, which usually give rise to radiation losses and also dilute the fuel, the plasma is confined inside closed magnetic flux surfaces. Two techniques are used. The first is to define an outer boundary of the plasma with a material limiter. The second is to keep the particles away from the vacuum vessel by means of a modification of the magnetic field.

When the plasma is directly in contact with the wall, the first point of contact with a solid object, which thus “limits” the plasma, defines the so-called “Last Closed Flux Surface” (LCFS) which determines the plasma boundary. The name “*limiter*” defines both this configuration and the components that are in direct contact with the plasma. It is also possible to produce a “*divertor*” configuration in which the contact between plasma and wall takes place on the divertor plates that consequently have to be designed to withstand a large power flux. Typically, this configuration is generated by producing a null point in the poloidal magnetic field within the chamber (**Figure 1.18**).

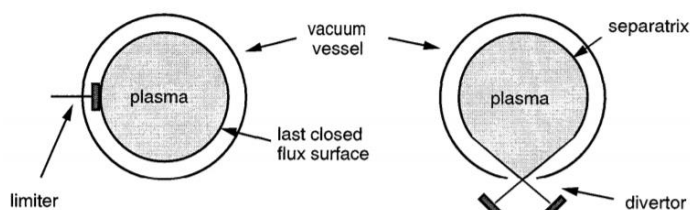


Figure 1.18: Limiter (left) and Divertor (right) plasma configurations. [1.2]

proportion to the stored energy. The loss of confinement is associated with the production of runaway electrons, which may also produce damage

Limiter configuration

In the *limiter configuration*, the charged particles close to the outer edge of the plasma, orbit around to the field lines impinging on the limiter: this is defined “plasma-wall interaction” (Chapter 2). When the plasma particle hits a plasma facing component, it is neutralized (it becomes atom or molecule recovering electrons) becoming unaffected by the magnetic field and thus free to move, colliding with the walls of the chamber or with other particles, until it will be ionized again. At this point, it begins once more to orbit around the field lines continuing to feed the plasma, if it has been ionized in the plasma core, otherwise it impinges on the wall again (**Figure 1.19**).

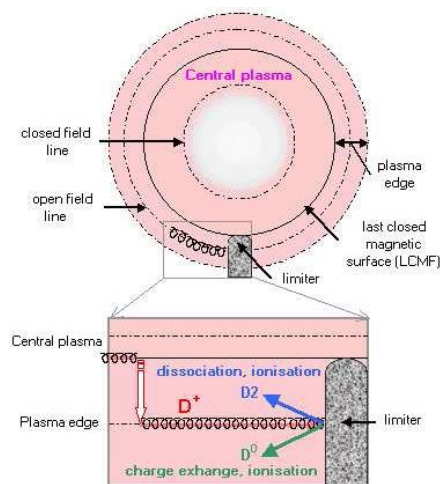


Figure 1.19: Plasma-wall interaction

This process goes on until the particle leaves the system, absorbed from the wall or from an external pumping system. During this cycle, it is possible to observe the coexistence of the four states of matter: plasma, walls (solid) of the chamber, gases that result from the interaction of the plasma with the wall and liquid coolants. Furthermore, in a tokamak a very wide range of temperatures is covered: from million-degrees in the plasma core, tens of thousands of degrees at the plasma edge, to hundreds on the components surfaces up to temperatures near absolute zero of superconductors (e.g., in ITER superconducting magnets will be employed).

With the development of plasmas at increasingly higher performance, the importance of plasma-wall interactions has been taken into account. With the increase of the power coupled to the plasma, then, it has been observed that the walls, under the bombardment of high energy particles, emit impurities. These impurities give rise to radiation losses and also dilute the fuel reducing the overall performance of the machine.

A first solution to this drawback, in addition to an accurate limiter design, has been the development of new materials.

Divertor configuration

The reduction of impurities entering the plasma plays a key role in the successful operation of tokamaks. This requires a separation of the plasma from the vacuum vessel. Therefore, after the optimization of limiter materials, the second idea was to keep the particles away from the plasma core by means of a modification of the magnetic field to produce a magnetic divertor. This idea led to the *divertor axisymmetric configuration* (Figure 1.20), where the LCFS is no longer defined as the point of contact with a solid surface, as in the limiter configuration, but rather it coincides with a magnetic boundary created by adding a suitable coil around the tokamak⁹.

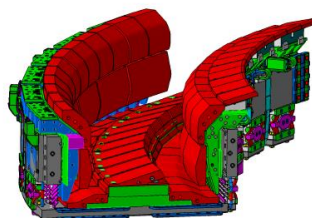


Figure 1.20: Example of a typical divertor in a tokamak.

The aim of the divertor is to lead the outgoing particles to a “target” surface well separated from the plasma, and to restrict the impurity back-flow. A difficult problem associated with the divertor is that of limiting the power density flowing to the target surface (Chapter 3).

⁹ In such a way, the contact of the plasma with the vessel surfaces is limited to the initial instants of a discharge in which the plasma is formed.

This is necessary to avoid high surface temperatures which can lead to surface melting or catastrophic impurity release by evaporation or other processes.

The required magnetic field is produced by toroidal conductors that create a null (also called “X-point”) in the poloidal field and a separation of open and closed magnetic surfaces. These divertors have the advantage of preserving the essential axisymmetry of the tokamak and can be combined with D-shaped or elliptical cross-sections (**Figure 1.21**).

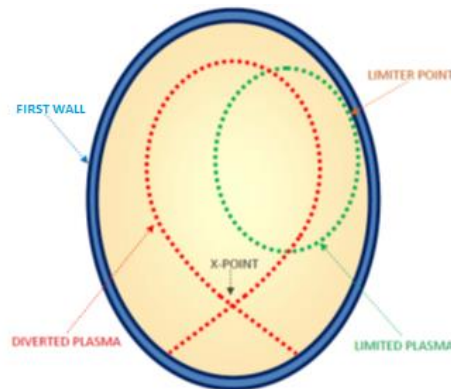


Figure 1.21: Limiter and divertor plasma configurations.

In **Figure 1.22**, the particle flow leaving the plasma by radial diffusion is represented by the white arrow. In the limiter configuration (left), the charged particles escaped from the plasma central region follow the field lines impinging on the limiter. The impact can neutralize these charged particles, and on the other hand can remove neutral impurities from the wall. The neutral particles do not follow the magnetic field lines until they are ionized, most likely in the plasma core.

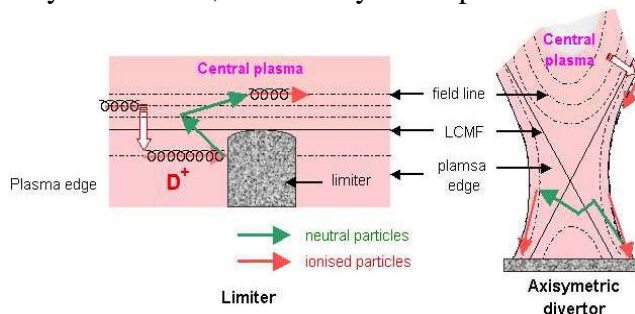


Figure 1.22: Differences between the limiter and divertor plasma configurations.

In the divertor configuration (right), the particle flow moving further away from the plasma is guided by the field lines up to the neutralization regions, far away from the plasma core. More likely, the impurities are ionized again in this marginal region and in this way, following the field lines, are intercepted again by neutralization divertor plates. Therefore, they remain closed in a circuit that prevents them from interfering with the central plasma region and can be effectively removed through cryocondensation pumps.

1.6 Plasma heating

In order to heat the plasma up to 100 millions degrees, the temperature needed to trigger the fusion reactions, different techniques are used.

1.6.1 Main plasma heating

The plasma is self-heated by ohmic effect (“ohmic heating”), thanks to the (toroidal) plasma current I_p induced by the central solenoid.

At low temperatures, the energy transferred to the plasma is considerable and, in large tokamaks, easily produces temperatures of a few keV. This energy, expressed for convenience in terms of specific power dissipation, is given by:

$$P_{\Omega} = \eta J^2$$

Where η is the plasma resistivity and J is the current density. However, as the temperature increases the frequency of collisions and the resistivity drop. Consequently, at the temperatures required for ignition the ohmic heating is greatly reduced requiring additional heating.

1.6.2 Additional heating techniques

The main additional heating techniques employed to achieve the temperatures necessary for the plasma fusion are essentially two:

- the Neutral Beam Injection (NBI);
- the Radio Frequency Heating (RF).

Neutral beam injection (NBI)

This technique involves the introduction of highly energetic neutral particles. Such particles injected into the plasma should be necessarily neutral because if they were charged, e.g. ions, would be reflected by the tokamak magnetic field. This heating process is rather articulated: firstly, one must produce the ions of hydrogen isotopes and subsequently accelerate them, by means of high voltage; such ions are then neutralized by passing through a thin hydrogen gas. At this step, called “charge-exchange” (CX), through collisions electrons are transferred from neutral atoms to those ionized appropriately accelerated. Once neutralized, the particles can cross the magnetic field and reach the plasma. Colliding with the plasma, they transfer their energy mainly to the electrons. Doing so, they become charged again and for this reason, being again subject to the magnetic field, they remain confined becoming part of the plasma. It is desirable that most of particles are deposited in the plasma core. In this way, both an excessive absorption, which would lead to the heating of the edges of the plasma, and a low absorption, that would allow the transmission of particles through the plasma producing heating and sputtering of materials on the surface of the chamber, should be avoided.

Radio frequency heating (RF)

With the radio frequency heating technique, high-frequency electromagnetic waves transfer energy to the plasma mixture. Since in a tokamak the ions and electrons of the plasma move rotating around the magnetic field lines with a regular frequency, electromagnetic waves having the right frequencies (typically in the radio-frequency range of the electromagnetic spectrum) are able to resonate with the rotation, transferring their energy to the plasma particles. As an electromagnetic wave propagates through a plasma, the wave electric field resonates with the cyclotron motion of plasma particles by accelerating the charged particles that heat the plasma through collisions. Since the energy is transferred to the plasma at the exact location where radio waves resonate with the ion/electron rotation, the antennas, which produce the waves responsible for the heating, are

mounted inside the vacuum chamber¹⁰. The system design must be such as to allow the waves to propagate in the central region of the plasma where the absorption is improved.

The radio frequency heating has been used since the early days of fusion research. The plasma particles have different resonance frequencies, depending on their mass and charge and the magnetic field strength at their location. Therefore, the heating can be applied selectively to a defined group of particles in a defined location in the plasma, by injecting radiation at just the right frequency. In such a way, it is possible to distinguish among the three different cyclotron frequencies: ion, lower hybrid and electrons. Each method has been tested to the megawatt level in major experimental tokamak facilities.

The model with the lowest frequency is the Ion Cyclotron Resonance Heating (ICRH). In this case, a resonance frequency occurs only when there are two or more species of ions. It is called ion-ion, or Buchsbaum, hybrid resonance. The resonant frequency with two species of ions is in the range 30-120 MHz, depending on the magnetic field and the species. The Lower Hybrid Resonance Heating (LHRH) frequency is located between the cyclotron frequency of the ion and the electron. This defines the heating system for lower hybrid resonance that uses the frequency range 1-8 GHz.

Finally, the scheme with the highest frequency is the Electron Cyclotron Resonance Heating (ECRH). The heating scheme for electron cyclotron resonance requires sources within the frequency range 100-200 GHz.

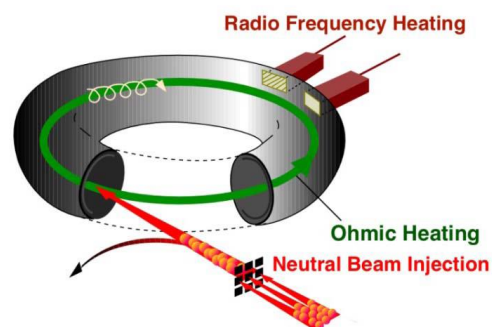


Figure 1.23: Plasma heating techniques.

¹⁰ Except for the ECRH case.

Figure 1.23 shows the two additional heating techniques (red) in addition to the plasma ohmic heating (green).

1.7 Energy production in a thermonuclear power plant

How is it possible to obtain energy from a tokamak reactor? A tokamak reactor is considerably more complex than the present experimental devices. The **Figure 1.24** illustrates conceptually the structure of such a thermonuclear fusion device.

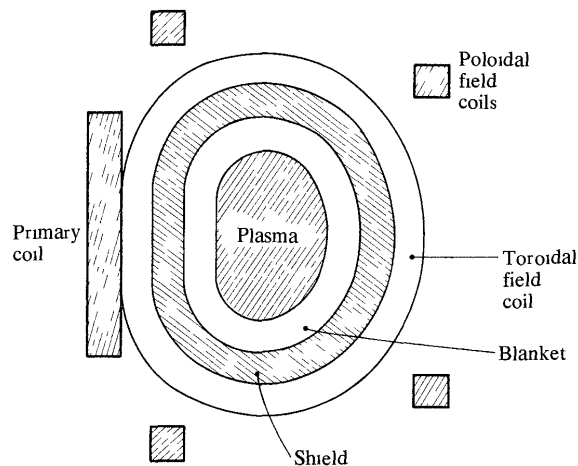
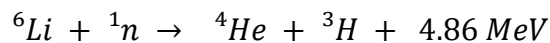
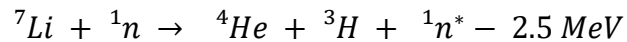


Figure 1.24: Layout of the main components in a conceptual fusion reactor device. [1.2]

A blanket surrounds the plasma. The blanket has mainly three roles. First, it absorbs the 14 MeV neutrons, carrying 80% of the energy produced in the fusion reaction, transforming their energy (essentially kinetic) into heat then removed by a suitable cooling liquid. Secondly, by absorbing neutrons, the blanket protects the superconducting coils and the other external components. Finally, the blanket allows the breeding of tritium, which is practically non-existent in nature, feeding the fusion reaction. The blanket is therefore made of light metal lithium (Li, which abounds in the rocks of the Earth's crust and is also present,

even though in low concentrations, in the oceans), which is transformed, once the neutron produced in the fusion reaction reaches the blanket, into tritium and helium according to the reactions:



(n^* is a slow neutron). The sign ‘-’ in the first equation expresses the need to provide energy from the outside.

A tritium atom is produced in each reaction neutron-lithium, as described in the previous expressions, but it is not possible to design the blanket so that all neutrons undergo such a reaction. In order to overcome this lack and create a overall breeding ratio higher than one, a neutron multiplier as beryllium or lead has to be used. The neutron flux from the plasma decays in the blanket; a blanket thickness between 0.6 and 1.0 m is usually sufficient to absorb most of the neutrons. The flow of neutron energy passing through the outer wall of the blanket in the form of heat must be reduced by a factor of $10^6 \div 10^7$ before reaching the superconducting coils to prevent both the radiation damage and the heating of such coils. This protection is obtained by placing a shield of about 1 m thick of material, such as the steel, between the blanket and the coils.

In an experimental tokamak, such as JET, the surface surrounding the plasma is rather defined “first wall”. The direct contact between the plasma and this first wall is limited to the divertor region during the main stages of a discharge whereas the main plasma touches the “limiter”, only in the early formation stages of the plasma.

In a nuclear power plant, capable of producing energy by nuclear fusion, the power load that reaches the solid surfaces and must be dissipated will be very large. The consequent need to minimize the flow of impurities in the plasma along with a greater design flexibility, favours the divertor configuration.

The idea of a tokamak reactor operating with a current generated by an induced electric field, and therefore as a pulsed device, has substantial drawbacks related to the fatigue stress produced by the thermal cycling and the interruption of the power output. These problems could be removed by a non-inductive current drive system that would make continuous operation feasible. Part of plasma current can be earned in

the form of the plasma self-generated bootstrap current. Such operating scenarios bring the efficiency demanded of the non-inductive current drive system within the range of technical feasibility. Current drive in the plasma centre can be provided by fast waves, high energy neutral beam injection or electron cyclotron waves, whereas efficient current drive at large minor radius is more difficult because of the lower electron temperature and the deleterious effects of trapped electrons. The heat leaving the plasma and the one produced in the fusion power plant blanket should be removed through a suitable liquid or gaseous coolant and then transformed into electricity by conventional means, as shown in **Figure 1.25**.

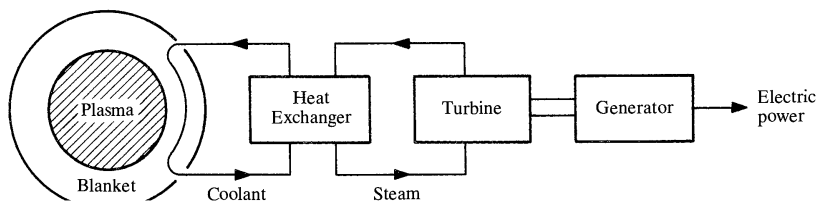


Figure 1.25: How thermonuclear power absorbed by the blanket could be converted into electrical power by conventional means (in the example, a steam turbine). [1.2]

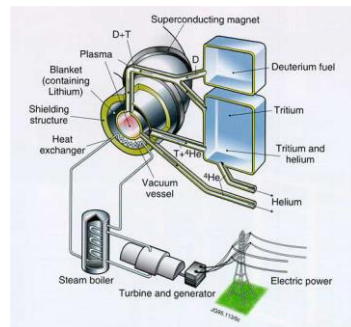


Figure 1.26: Scheme of a fusion power plant.

1.8 The present and future of the fusion: from Jet to DEMO through ITER and DTT

JET (Joint European Torus), operating since 1983, is currently the largest tokamak in the world (**Figure 1.27**) and the only operational fusion experiment capable of producing fusion energy. In 1997, JET produced 16 MW of fusion power from a total input power of 24 MW (fusion energy gain factor $Q = 0.67$). This record was set by using a Deuterium–Tritium plasma.



Figure 1.27: the JET machine during construction (1985). [1.4]

Since 2000, the scientific and technical programme has been conducted under the European Fusion Development Agreement (EFDA) and the device has been operated on behalf of EFDA by the United Kingdom Atomic Energy Authority. The principal aims of the experiment are the investigation of heating and confinement in reactor relevant plasma conditions, the investigation of plasma-wall interactions and the study of α -particle production, confinement, and consequent plasma heating.

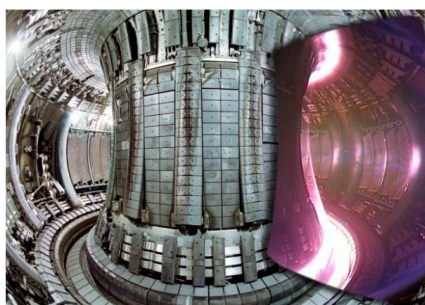


Figure 1.28: the JET vacuum chamber. [1.5]

The heart of the structure is the Vacuum Vessel¹¹ (**Figure 1.28**) in which the pressure could reach up to a millionth of a millionth of the density of air (*usually* $> 1^{-6} Pa$). The machine main parameters are listed in **Table 1-I**:

Table 1-I: JET main parameters.

Parameter	Value
Major radius	2.96 m
Minor Radius	1.25–2.10 m
Plasma volume	100 m ³
Magnetic field	3.45 T (toroidal)
Plasma current	3.2 MA (circular), 4.8 MA (D-shape)

During experiments, the interaction between currents and magnetic fields produces very intense forces. A D-shaped poloidal cross-section (**Figure 1.29**) tends to overcome these forces minimizing stresses in the toroidal field coils and maximizing at the same time the plasma volume.

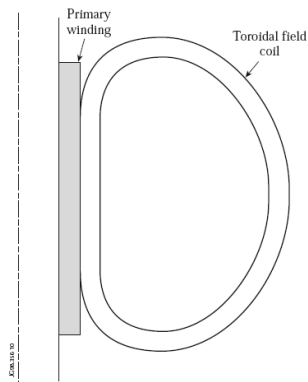


Figure 1.29: D-shaped geometry. [1.2]

The experiments in JET are carried out with pulsed approach. Usually, during the experimental campaign every twenty minutes there is a shot

¹¹ Low background pressure (hence the name “Vacuum Vessel”) is necessary to minimize the presence of impurities inside the chamber.

of the ITER Project”. On 28 June 2005, the seven members of the Project unanimously agreed on the site proposed by Europe, a 180-hectare stretch of land adjacent to one of France’s largest nuclear research centres, and close to the small Provençal village of Saint-Paul-lez-Durance. Construction of the ITER Tokamak complex (**Figure 1.31**) started in 2013 and the first plasma is foreseen in 2025.



Figure 1.31: ITER site. [1.6]

The amount of fusion energy a tokamak is capable of producing is a direct result of the number of fusion reactions taking place in its core. The larger is the vessel, the larger is the volume of the plasma and therefore the greater is the potential for fusion energy.

With ten times the plasma volume of the largest machine operating today, the ITER Tokamak will be a unique experimental tool, capable of longer plasmas and better confinement. **Table 1-II** shows the machine main parameters [1.3].

Table 1-II: ITER main parameters.

Parameter	Value
Major radius	6.2 m
Minor Radius	2.0 m
Plasma volume	840 m ³
Magnetic field	5.3 T (toroidal)
Plasma current	15 MA

ITER has been designed specifically to [1.6]:

1) Produce 500 MW of fusion power

The world record for fusion power is held by the European tokamak JET. ITER is designed to produce a ten-fold return on energy ($Q = 10$), or 500 MW of fusion power from 50 MW of input power. ITER will not capture the energy it produces as electricity, but - as first of all fusion experiments in history to produce net energy gain - it will prepare the way for the machine that can.

2) Demonstrate the integrated operation of technologies for a fusion power plant

ITER will bridge the gap between today's smaller-scale experimental fusion devices and the demonstration fusion power plants of the future. Scientists will be able to study plasmas under conditions similar to those expected in a future power plant and test technologies such as heating, control, diagnostics, cryogenics and remote maintenance.

3) Achieve a deuterium-tritium plasma in which the reaction is sustained through internal heating

Fusion research today is at the threshold of exploring a "burning plasma" - one in which the heat from the fusion reaction is confined within the plasma efficiently enough for the reaction to be sustained for a long duration. Scientists are confident that the plasmas in ITER will not only produce much more fusion energy, but will remain stable for longer periods of time [1.6].

4) Test tritium breeding

One of the missions for the later stages of ITER operation is to demonstrate the feasibility of producing tritium within the vacuum vessel. The world supply of tritium (used with deuterium to fuel the fusion reaction) is not sufficient to cover the needs of future power plants. ITER will provide a unique opportunity to test mockup in-vessel tritium breeding blankets in a real fusion environment.

5) Demonstrate the safety characteristics of a fusion device

ITER achieved an important landmark in fusion history when, in 2012, the ITER Organization was licensed as a nuclear operator in France based on the rigorous and impartial examination of its safety files. One of the primary goals of ITER operation is to demonstrate the control of the plasma and the fusion reactions with negligible consequences to the environment.

Despite the size, the aim and the cost of ITER (originally expected to cost approximately 5 billion €) EUROfusion is already designing its successor. DEMO (DEMONstration Power Station) is a proposed nuclear fusion power station. The objectives of DEMO are usually understood to lie somewhere between those of ITER and a “first of a kind” commercial station. The following parameters are often used as a baseline for design studies: DEMO should produce at least 2 gigawatts of fusion power on a continuous basis, and it should produce 25 times as much power as required for breakeven. DEMO’s design will be on the scale of a modern electric power station [1.7].

To achieve its goals, DEMO must have linear dimensions about 15% larger than ITER, and a plasma density about 30% greater than ITER.

At the beginning of 2012, the European Commission requested EFDA to prepare a *technical roadmap* to fusion electricity by 2050. The realisation of fusion energy has to face a number of technical challenges. For all of them candidate solutions have been developed and the goal of the programme is to demonstrate that they will also work at the scale of a reactor. *Eight different roadmap missions* have been defined and assessed. They will be addressed by universities, research laboratories and industries through a goal-oriented programme during the Horizon 2020 period [1.8]. According to the present roadmap, a demonstration fusion power plant (DEMO), producing net electricity for the grid at the level of a few hundred Megawatts is foreseen to start operation in the early 2040s. Following ITER, it will be the single step to a commercial fusion power plant.

The mission number two, related to the development of an adequate solution for the enormous plasma heat exhaust of DEMO, is one of the most challenging among the roadmap missions. The design of a new

machine named “Divertor Tokamak Test facility” (DTT), capable of integrating all relevant physics and technology issues has been promoted by EUROfusion. The DTT project proposal has been realized by the Italian Research agency ENEA (Italian National Agency for New Technologies, Energy and Sustainable Economic Development). DTT facility will assess possible alternative solutions to the power exhaust issue, including advanced magnetic configurations and liquid metal divertors [1.9]. DTT should operate integrating various aspects, with significant power loads, flexible divertors, plasma edge and bulk conditions approaching as much as possible those planned for DEMO, at least in terms of dimensionless parameters. An optimal balance between these requirements and the need to realize the new experiment accomplishing the DEMO timescale, leads to the choice of the machine parameters listed in **Table 1-III**.

Table 1-III: DTT main parameters.

Parameter	Value
Major radius	2.15 m
Aspect ratio (R/a)	3.1
Magnetic field	5.3 T (toroidal)
Plasma current	15 MA
Additional power	45 MW

The machine will have the possibility to test several different magnetic divertor topologies, in reactor relevant regimes. Different plasma facing materials will be tested (tungsten, liquid metals) up to a power flow of the order of $20 \text{ MW}/\text{m}^2$. The final target of this experiment is the realization of an integrated solution (bulk and edge plasma) for the power exhaust in view of DEMO. The related studies and experiments will allow a valuable development of innovative technologies in several different fields, with relevant spin off for the industries of all European Countries. According to the European Roadmap, the DTT experiment should start its operation in 2022. To be coherent with this plan, the realization of the device will cover a time of around 7 years, starting from the first tender (during 2016) up to full commissioning and the first plasma (during 2022). The operations should then cover a period

of more than 20 years, up to the initial phases of the DEMO realization [1.9].

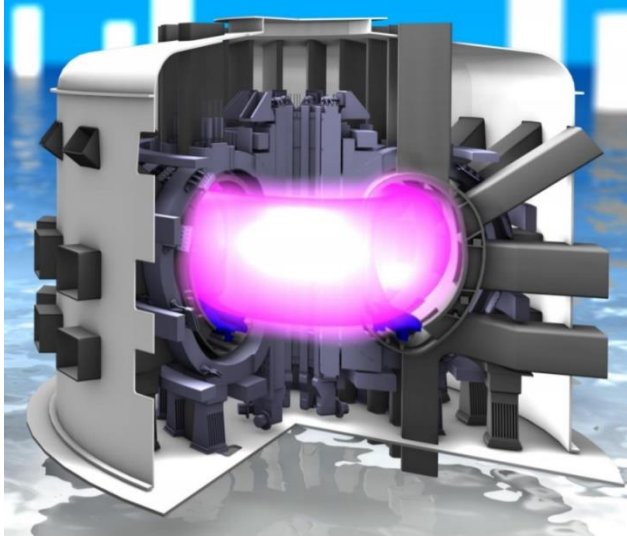


Figure 1.32: DTT design. [1.9]

Figure 1.32 shows the DTT conceptual design.

References

- [1.1] <http://www.eia.gov/todayinenergy/detail.php?id=26212>
- [1.2] Wesson J., “Tokamaks – third edition”, Clarendon Press-Oxford 2004, ISBN 0 19 8509227
- [1.3] <http://fusionwiki.ciemat.es/wiki/ITER>
- [1.4] <https://www.euro-fusion.org/2011/09/construction-of-the-jet-machine-3/?view=gallery-428>
- [1.5] <http://www.bbc.com/news/science-environment-27138087>
- [1.6] <https://www.iter.org/proj/inafewlines#2>
- [1.7] “Demonstration Fusion Reactors”. Fusion for Energy. European Joint Undertaking for ITER and the Development of Fusion Energy,
https://web.archive.org/web/20070708082042/http://www.fusionforenergy.europa.eu/3_4_demo_en.htm
- [1.8] EFDA, “Fusion Electricity - A roadmap to the realisation of fusion energy”,
<https://www.euro-fusion.org/wpcms/wp-content/uploads/2013/01/JG12.356-web.pdf>
- [1.9] “DTT - Divertor Tokamak Test facility”, ISBN: 978-88-8286-318-0

Chapter 2

“[...] The first and fourth state of matter do not co-exist easily. Plasma erodes solids and the eroded material enters the plasma, degrading its desired properties. Much of the challenge for magnetic confinement fusion is to find a solution that will allow these two mutually irritating states of matter to cohabit a small space.”

Stangeby P. C., “The Plasma Boundary of Magnetic Fusion Devices” [2.1]

The plasma-surface interactions

In the previous chapter, the physics of plasma has been treated as if it were isolated from the rest of the universe, but they are not. In fact, plasmas interact strongly with the surrounding materials constituting the tokamak or, more in general, an experimental device. Ions, electrons and radiation from the plasma are incident on the surrounding solid surfaces, heating them and producing neutral atoms and molecules of plasma and wall materials, which return to the plasma to undergo a variety of reactions with plasma ions and electrons, producing further charged and neutral particles incident upon the wall surfaces. The surfaces surrounding the plasma, therefore, behave both as a source and sink for the plasma, refuelling and cooling it, greatly affecting also its composition. In this chapter, the various physical processes that are involved in plasma–material interactions will be examined.

2.1 The plasma sheath

At the interface between the plasma and the surfaces there is a complex situation. As already seen in Chapter 1, some plasma ions, flowing along the magnetic field lines, impinge on a solid surface. If the “upstream” regime is collisional, or in other terms ions and electrons have similar temperatures, the thermal speed of the much less massive electrons is much greater than the one of the ions, $v_{th(e)} \gg v_{th(i)}$. This

circumstance leads the electrons to reach the surface much faster, creating a large negative charge relative to plasma. However, an electric field establishes equalizing the two flows by accelerating the ions and decelerating the electrons. Such an electric field is located at the surface in a thin “*sheath*”, few Debye lengths thick. Moreover, a smaller electric field extends into a more deep “*pre-sheath*” region of the plasma (**Figure 2.1**).

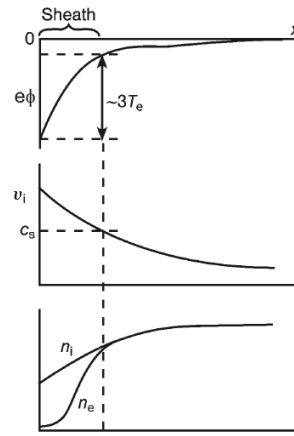


Figure 2.1: Spatial variation of the electrostatic potential, ϕ , the ion speed, v_i , and the ion and electron densities across the sheath from the wall (on the left) to the pre-sheath (on the right) [2.2]

The electrostatic potential satisfies Poisson’s equation:

$$\frac{d^2\phi}{dx^2} = \frac{e}{\epsilon_0}(n_e - n_i) \quad (2.1)$$

where n_e and n_i are, respectively, the electron and ion densities.

Defining the “sheath potential” to be zero at the sheath boundary, if n_0 is the average value of the electron or ion density at the entrance to the sheath from the pre-sheath region (i.e. the value at the dashed vertical line in **Figure 2.1**), then the electron distribution is described by the Boltzmann distribution:

$$n_e = n_0 \exp\left(\frac{e\phi}{T_e}\right) \quad (2.2)$$

Defining as v_0 the speed with which ions enter the sheath from the pre-sheath region, then conservation of energy provides an expression for the ion velocity in the sheath

$$\frac{1}{2}m_i v_i^2 = \frac{1}{2}m_i v_0^2 - e\phi \quad (2.3)$$

If no sources or sinks of ions are assumed in the sheath, $n_i v_i$ must be constant across the sheath, which leads to an expression for the ion density in the sheath

$$n_i = n_0 \left(\frac{\frac{1}{2}m_i v_0^2}{\frac{1}{2}m_i v_0^2 - e\phi} \right)^{1/2} \quad (2.4)$$

Combining these equations yields an equation for the electrostatic potential in the sheath region

$$\frac{d^2\phi}{dx^2} = \frac{n_0 e}{\epsilon_0} \left[\exp \frac{e\phi}{T_e} - \left(\frac{\frac{1}{2}m_i v_0^2}{\frac{1}{2}m_i v_0^2 - e\phi} \right)^{1/2} \right] \quad (2.5)$$

The ion velocity at the pre-sheath, v_0 , is determined by requiring that the solution of Eq. (2.5) at the pre-sheath boundary matches the slowly varying potential outside the sheath. For small ϕ , Eq. (2.5) becomes:

$$\frac{d^2\phi}{dx^2} = \left(1 - \frac{T_e/m_i}{v_0^2} \right) \frac{\phi}{\lambda_D^2} \quad (2.6)$$

where λ_D is the Debye length. A slowly varying solution of Eq. (2.6) requires:

$$v_0 \cong (T_e/m_i)^{1/2} \quad (2.7)$$

The calculations carried out so far neglected the ion temperature. Therefore, include ion temperature effects in the achieved results yields:

$$v_0 = [(T_e + T_i)/m_i]^{1/2} \cong c_s \quad (2.8)$$

Thus, *the plasma enters the sheath at the speed of sound* [2.2].

The potential across the sheath, ϕ_0 , is determined imposing the total current to the surface to be zero. The ion current density into and across the sheath into the surface is:

$$j_i = n_0 e c_s \quad (2.9)$$

The electron flux to the surface is $n_e \bar{c}_e / 4$, where $\bar{c}_e = (8T_e / \pi m_e)^{1/2}$ is the average electron speed for a Maxwellian electron distribution. Using Eq.(2.2), the electron current density into the surface is:

$$j_e = -\frac{1}{4} n_0 e \bar{c}_e \exp \frac{e\phi_0}{T_e} \quad (2.10)$$

The requirement $j_i + j_e = 0$ then leads to:

$$-\frac{e\phi_0}{T_e} = \frac{1}{2} \ln \left[\frac{m_i/m_e}{2\pi(1 + T_i/T_e)} \right] \quad (2.11)$$

For a deuterium plasma with $T_i = T_e$, this yields $-e\phi_0 = 2.8T_e$.

Secondary electrons are produced at the surface by ion and electron bombardment, with emission coefficient δ , and are accelerated out of the sheath into the pre-sheath by the electric field. Including this effect in the above derivation leads to:

$$-\frac{e\phi_0}{T_e} = \frac{1}{2} \ln \left[\frac{(1 - \delta)^2 m_i/m_e}{2\pi(1 + T_i/T_e)} \right] \quad (2.12)$$

Plasma ions enter the sheath with their thermal energy and are accelerated across the sheath into the surface by the electric field. Similarly for the electrons, except that they are decelerated. The distributions can be approximately represented by Maxwellians, but at temperatures that are lower than the pre-sheath temperature for the electrons and higher for the ions. However, only the higher energy pre-sheath electrons actually survive the deceleration and reach the surface. The energy transported to the surface in a Maxwellian distribution of ions or electrons is $2T$ per particle. Including the acceleration of ions in the sheath, the *power flux to the surface* is:

$$P = n_e c_s T_e \left[\frac{2T_i}{T_e} + \frac{2}{1-\delta} + \frac{1}{2} \ln \left(\frac{(1-\delta)^2 m_i/m_e}{2\pi(1+T_i/T_e)} \right) \right] \quad (2.13)$$

Eq. (2.13) could also be written easily as:

$$P = \gamma_s \Gamma T_e \quad (2.14)$$

where Γ is the ion flux and $\gamma_s \approx 7$ to 8 is an effective sheath power transmission coefficient.

2.2 Ion/Atom Back-scattering and Recycling

A plasma ion or neutral atom colliding with a surface could undergo, mainly, one or more *elastic* or *inelastic scattering* events with the atoms of the surface material:

- in the *elastic* case, it may be *back-scattered* or reflected keeping a significant fraction of its original energy after one or more collisions;
- in the *inelastic* case, it may lose essentially all of its energy in collisions and come into equilibrium with the atoms of the surface and near-surface material and subsequently diffuse (preferentially) to the incident surface and be “re-emitted” into the plasma as a *thermal particle* (usually after molecule formation) with the thermal energy of the surface.

Usually, there are no particular differences between incident atoms and ions. An ion approaching a solid surface extracts an electron as it enters the solid, undergoing the process also known as *surface recombination*, and so the interaction with the solid is the same as for an atom. Moreover, when the particle is reflected, the probability that it will do so as a neutral is quite high. In fact, although initially it was a charged particle, since the velocity of the separation between the reflected particle and the surface is slow compared with typical electron speeds,

there is enough time for an electron to be released from the surface and to neutralize a departing ion.

The *back-scattering* of incident ions or atoms depends on the energy of the incident particle, on the ratio of masses of the incident particle and the surface atom and on the angle of incidence. Particle reflection is characterized by a particle coefficient $R_p(E)$, defined as the ratio of the particle flux returning to the plasma to the incident particle flux, and an energy reflection coefficient $R_E(E)$, defined as the ratio of the energy flux returning to the plasma to the incident energy flux. The energy and particle reflection coefficients are related by:

$$R_E(E_0) = \frac{\bar{E}(E_0)}{E_0} R_p(E_0) \quad (2.15)$$

where E_0 is the energy of the incident particle and \bar{E} is the average energy of the reflected particles. Values of R_p and R_E are given in **Figure 2.2**. The reflected particles are primarily neutral atoms and are distributed continuously in energy with mean reflected energy of 30% to 50% of the incident energy.

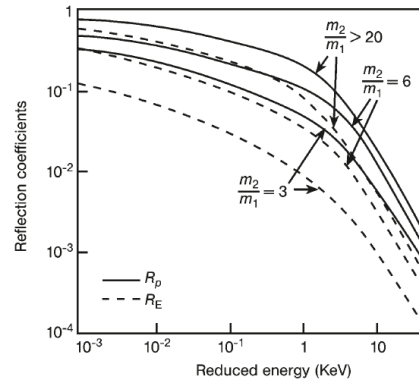


Figure 2.2: Particle and energy reflection coefficients for particles reflected from solid surfaces.

(The reduced energy is defined as $\varepsilon = 32.5m_w E / \left((m_i + m_w) z_i z_w (z_i^{2/3} + z_w^{2/3})^{1/2} \right)$ with E in eV) [2.2]

The $(1 - R_p)$ fraction of the incident particles that are not reflected are thermalized within the solid and reside in interstitial sites or defects, such as vacancies, in the metal. For hydrogen isotopes, diffusion readily

occurs at room temperature and above in many materials. Notable exceptions are carbon, carbides and oxides.

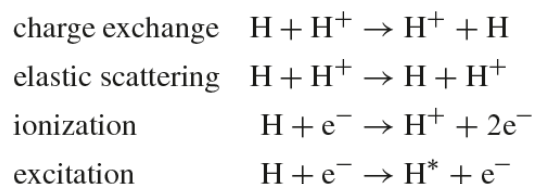
When diffusion occurs, the behaviour of the hydrogen depends on the heat of solution of hydrogen in the material. In the exothermic case, there is, effectively, a potential barrier at the surface that prevents the release of hydrogen back into the plasma, in which case it diffuses back and is distributed over the material volume. In the endothermic case, hydrogen atoms reaching the plasma surface form molecules and are released back into the plasma with an energy distribution similar to that of the atoms in the solid.

In most tokamaks, the pulse length is at least an order of magnitude longer than the particle replacement time. Thus on average each plasma ion goes to the divertor target plate or limiter and returns to the plasma many times during the discharge. This process is called *recycling*. A recycling coefficient can be defined as the ratio of the total particle flux returning to the plasma (reflection plus re-emission) to the incident particle flux. The instantaneous recycling coefficients for a given machine will vary considerably with operating history.

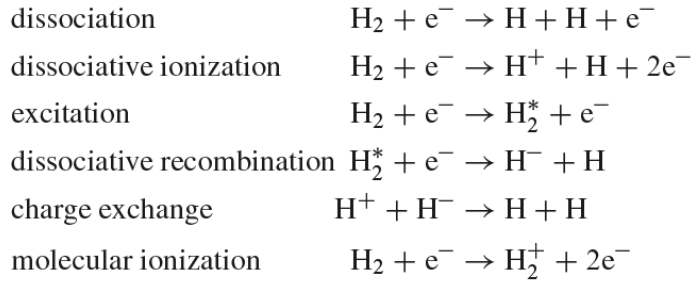
2.3 Atomic and molecular processes

In the recycling and fuelling processes, atomic and molecular reactions occur in the boundary layer when the incoming hydrogen isotopes meet the energetic ions and electrons of the plasma. Further reactions occur when impurities created by sputtering and by other plasma-surface interactions enter the plasma. *The dominant atomic reactions* are, in most cases, *excitation and ionization*. These *give rise to radiation and hence cooling of the edge plasma*. This is beneficial since it lowers the incident ion energy and reduces the physical sputtering rate.

For the reflected hydrogen (or deuterium or tritium) atoms the main processes are:



For the re-emitted and gas injected hydrogen (or deuterium or tritium) molecules the important processes are:



The reaction rates for these various processes are functions of plasma temperature and density, as indicated by the rate coefficients shown in **Figure 2.3**.

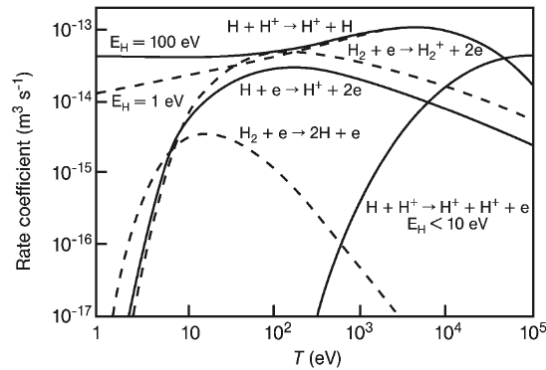


Figure 2.3: Rate coefficients for various common reactions for hydrogen atoms and molecules [2.2]

Multi-step processes are important in determining overall ionization and recombination rates at lower temperatures, depending on the plasma density. Atomic ionization and recombination rate coefficients, averaged over Maxwellian distributions, are shown for hydrogen in **Figure 2.4**.

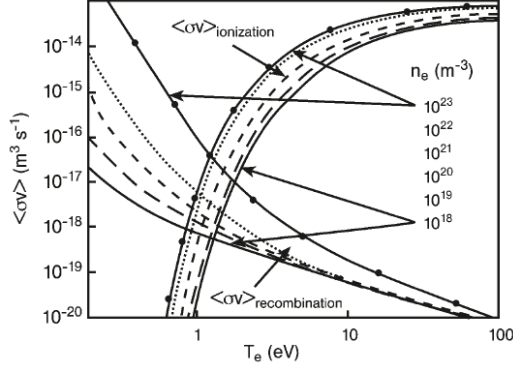


Figure 2.4: Hydrogen ionization and recombination rate coefficients [2.2]

The various molecular reactions involved in the eventual production of H atoms and H^+ ions from a H_2 molecule in the ground state constitute a rather complicated multi-step process. Because of differences in reaction rate coefficients, certain steps in multi-step processes are rate limiting. Some simplification can be achieved by identifying the rate limiting steps and summing reactions that lead to the same outcome. Ionization and, at very low temperatures, recombination are, respectively, important atomic cooling and heating mechanisms for plasma electrons

$$P_{cool}^H = P_{cool,iz}^H + P_{cool,rec}^H = (P_{rad,iz}^H + I_{iz}\langle\sigma v\rangle_{iz,H}) + (P_{rad,rec}^H - I_{iz}\langle\sigma v\rangle_{rec,H}) \quad (2.16)$$

where $I_{iz} = 13.6 \text{ eV}$ is the ionization potential of hydrogen, $\langle\sigma v\rangle$ are the Maxwellian averaged rate coefficients for ionization and recombination given in **Figure 2.4**, and the P_{rad} are the radiation emission rates for ionization and recombination given in **Figure 2.5** and **Figure 2.6**.

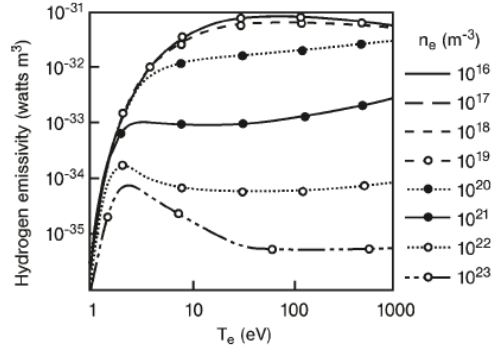


Figure 2.5: Hydrogen radiation emission coefficients due to ionization [2.2]

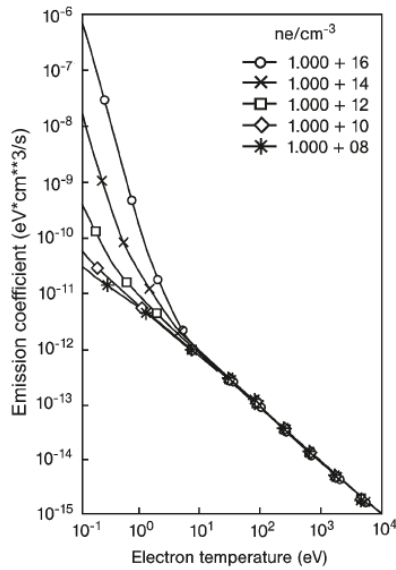


Figure 2.6: Hydrogen radiation emission coefficients due to recombination.
(Multiply by 1.6×10^{-25} for $W m^3$ units) [2.2]

2.4 Sputtering

The removal of atoms from the surface of a solid as a result of impact by ions or atoms is known as “sputtering”. It gives rise to impurities that cause power to be radiated from the plasma making ignition more difficult. It also leads to erosion of surfaces at a rate which is expected

to be a limiting factor in tokamak reactor design. Sputtering can occur due to both physical and chemical processes.

2.4.1 Physical sputtering

An energetic ion or neutral atom incident on a solid surface produces a collision cascade among the lattice atoms [2.3]. Physical sputtering takes place when this cascade results in a surface atom receiving sufficient energy to exceed the surface binding energy. Thus, sputter yields decrease with increasing surface binding energy of the solid and increase with increasing energy transferred from the incident ion to the lattice atom. For light ions, such as hydrogen and helium, the sputter yields are small due to low energy transfer and the energy is dissipated mainly in inelastic processes.

There is in general a threshold energy, E_T , of the incident ion below which the energy transferred to the lattice atoms is insufficient for sputtering to occur. Its theoretical value is

$$E_T = \frac{E_s}{\gamma_{sp}(1 - \gamma_{sp})}$$

where E_s is the sublimation energy of the target solid and $\gamma_{sp} = 4m_1m_2/(m_1 + m_2)^2$, where m_1 and m_2 are the masses of the incident and target atoms respectively. The energy necessary to transfer E_s to the target atom in a head-on collision is E_s/γ_{sp} . The additional fraction of $(1 - \gamma_{sp})$ takes account of the reflection process, which is important for light ions.

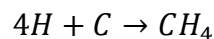
The dominant effect in determining the absolute magnitude of the sputter yield in different targets for the same incident ion is the surface binding energy and the atomic mass of the target atoms. There is some spread in the measured values of sputter yields for nominally the same system. This is due to uncontrolled factors such as surface structure and impurity levels, which can effectively change the binding energy of the surface atoms.

The sputter yield increases as the angle of incidence, θ , increases from the normal ($\theta = 0$). To first order this increase varies as $\cos^{-1} \theta$. However for light ions incident on heavier substrates the yield $S(\theta)$ increases faster than $\cos^{-1} \theta$ and $dS(\theta)/d\theta$ increases with incident

energy. This behaviour can be explained qualitatively by the increased probability of the incident ions being backscattered to the surface. Numerical codes based on both transport theory and Monte Carlo calculations give good agreement with laboratory experiments. At low energies, $E < 300 \text{ eV}$, the variation of yield with incident angle is negligible and this is the region of most interest in many plasma surface interactions. In practice, it is difficult to calculate the distribution in angle of incidence of ions arriving at a limiter or divertor target. The situation is complicated by the effects of the ion Larmor radius, the acceleration in the plasma sheath and the surface roughness. The surface roughness also varies with time during operation. Typically when comparing code results with tokamak experiments it is found that the effective yield is about twice that predicted for normal incidence [2.3].

2.4.2 Chemical sputtering

Chemical reactions between incident ions or neutrals and a solid surface can also lead to erosion of surfaces. In fusion devices, the most common of such reactions is that between hydrogen isotopes and carbon, for example:



Carbon is widely used as a limiter and divertor material because of its refractory qualities and the fact that it does not melt (unlike the tungsten). However, it has chemical sputtering yields which are comparable and sometimes higher than physical sputtering yields in terms of atoms removed per incident ion or atom. The chemistry depends on hydrogen atoms, on or in the surface, combining with one or more carbon atoms to form a hydrocarbon molecule. Because the hydrocarbons have a low binding energy to the surface they may be thermally released at temperatures as low as 300 K. The chemical reaction rate depends on the surface temperature of the solid as well as the energy of the incident ions [2.3].

2.4.3 Choice of materials

The final choice of plasma facing materials is very difficult and in general represents a compromise among many different criteria. These could include:

- impurity production rates;
- structural strength;
- neutron activation;
- thermal shock resistance

and other criteria. The increase of radiation from an impurity atom with increasing nuclear charge makes it desirable to minimize both Z and the sputter yield. A suggested figure of merit [2.3], M_m , is

$$M_m = f_l \frac{1 - Y_m}{Y_p} \quad (2.17)$$

where f_l is the maximum allowed impurity concentration in the plasma, Y_m and Y_p are respectively the impurity and plasma sputtering coefficients. The larger M_m is, the less power will be radiated.

Both the sputter yield and f_l are functions of T_e . A plot of M_m is shown as a function of edge plasma temperature for various materials in **Figure 2.7**. It is possible to see that, for low plasma edge temperatures, high Z refractory metals are best while at high edge temperatures only low Z materials are practical. This conclusion is consistent with the sputter yield curves shown in **Figure 2.7**.

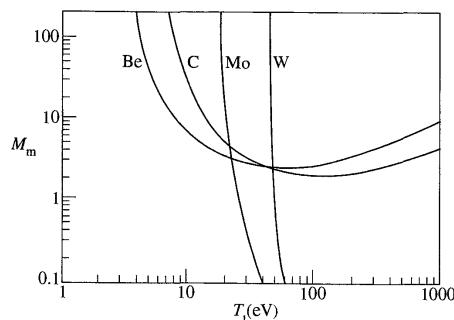


Figure 2.7: The figure of merit M_m , (equation (2.17)), as an estimate of the degree of contamination of the plasma by limiter or divertor target materials M_m is calculated as a function of plasma ion temperature for Be, C, Mo, and W. An ion charge Z of 3 is assumed. (From Laszlo, J. and Eckstein, W., *Journal of Nuclear Materials IM*, 22 (1991)) [2.3]

The plasma edge temperature increases with increasing power and decreases with increasing plasma density. A further factor to be considered is the probability of an impurity entering the confined plasma. Detailed analysis would also take into account impurity transport in the plasma.

2.5 Radiation Losses and Impurity Radiation

In a pure hydrogen plasma, the electromagnetic radiation is due to the acceleration of the charged particles. Because of their lighter mass the *electrons undergo larger acceleration than the ions radiating much more strongly*. The electrons are accelerated in two ways:

- firstly they are accelerated by collisions, the resulting radiation is known as “*bremstrahlung*”;
- secondly they are subject to the acceleration of their cyclotron motion and the associated radiation is called cyclotron or synchrotron radiation.

The presence of sputtered wall “impurity” atoms in the plasma produces further energy losses through radiation. Two types of process are involved:

- the first is the enhancement of *bremstrahlung* due to the higher value of the ionic charge for impurities;
- the second is the radiation which occurs through the atomic processes of line radiation and recombination.

In a steady state with negligible transport effects (coronal equilibrium) [2.3], the power radiated from a given impurity species is proportional to the electron density n_e and to the impurity density n_I , and the radiated power density may be written as

$$P_R = n_e n_I R$$

where the radiation parameter R is a function of the electron temperature. Graphs of $R(T_e)$ are given in **Figure 2.8** for a number of elements. The $R(T_e)$ curves have a principal maximum together with subsidiary maxima at higher temperatures. For light impurities, the principal maximum occurs at a low temperature and above this temperature the radiation is substantially reduced. As the temperature increases, electrons are successively removed from the impurity ions and when the ions are fully stripped only bremsstrahlung remains. In a reactor low Z atoms would be fully stripped. At a particular temperature a given impurity species will have a distribution of charge states Z . A mean value \bar{Z} , can be defined by

$$\bar{Z} = \sum n_z Z / n_I$$

where $n_I = \sum n_z$, n_z being the density of ions in the charge state Z . Some graphs of $\bar{Z}(T_e)$ are given in **Figure 2.8**.

For low Z impurities such as carbon and oxygen the maximum radiation occurs at a very low temperature, of the order of tens of eV . The ions of these impurities are fully stripped at a temperature of 1 keV and in the hot plasma of a reactor they would only radiate through bremsstrahlung. At the plasma edge radiation losses arise from the incompletely stripped impurities which enter the plasma as neutral atoms.

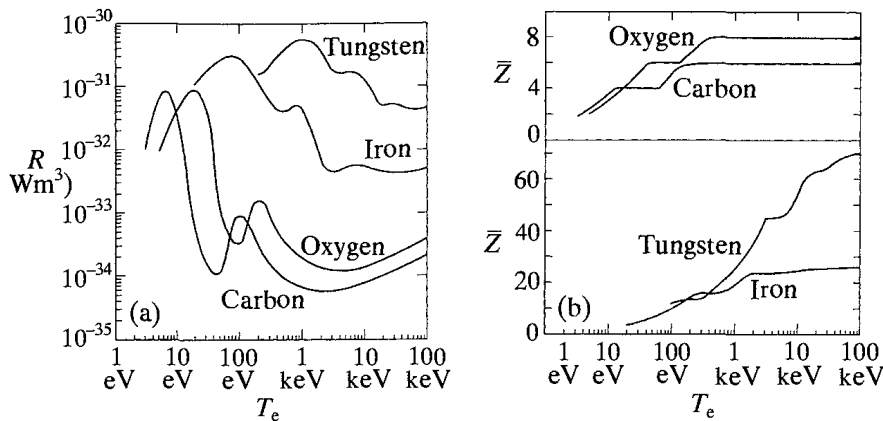


Figure 2.8: (a) The radiation parameter R and (b) the mean charge Z as functions of electron temperature for carbon, oxygen, iron, and tungsten, [2.3]

For high Z impurities, and these include the metals of which the tokamak is constructed, the first maximum in radiated power occurs at a somewhat higher temperature. For temperatures above 100 eV the radiation per ion is much greater than for low Z impurities. Even at reactor temperatures these ions are not fully stripped and the radiated power is such that the level of high Z impurities must be very small in a reactor.

2.6 Conclusions

One of the most difficult design issues for the next-generation fusion reactors is the choice of plasma facing materials, both for the first wall (or blanket) and divertor components.

The blanket is one of the most critical and technically challenging components in ITER. Due to its unique physical properties, i.e. low plasma contamination and low fuel retention, beryllium has been chosen as the element to cover the first wall. The rest of the ITER blanket modules will be made of high-strength copper and stainless steel. Furthermore, ITER will be the first fusion device to operate with an actively water cooled blanket.

In DEMO beryllium will not be suitable because of radiation damage, thus tungsten or alternative materials will be employed.

In most present-day tokamaks, carbon is used as divertor material due to the good heat flux handling capacity combined with the relatively low Z . It has, however, disadvantages, which might be unacceptable in a future fusion device as ITER or DEMO. Graphite suffers from an enhanced erosion by chemical processes even at low temperatures resulting in deposited layers around the vessel. The corresponding tritium enrichment would be too high for a reactor. Tungsten exhibits much more favourable properties with respect to erosion and other physical properties. Therefore, tungsten, with the highest melting point of all the metals, has been chosen as the armour material for the ITER divertor. Moreover, in ITER the heat load in which the kinetic energy of high-energy plasma particles striking the divertor targets is transformed will be removed by active water cooling. The heat flux sustained by the ITER divertor targets is estimated at 10 MW/m^2 (steady state) and 20 MW/m^2 (transients).

References

- [2.1] Stangeby P. C., “The Plasma Boundary of Magnetic Fusion Devices”, IOP Publishing Ltd 2000, ISBN 0 7503 0559 2
- [2.2] Stacey W. M., “Fusion Plasma Physics”, Wiley-VHC, ISBN 978-3-527-41134-4
- [2.3] Wesson J., “Tokamaks – third edition”, Clarendon Press-Oxford 2004, ISBN 0 19 8509227

Chapter 3

“[...] The centre of a fusion plasma is more than 100 million °C hot. The cooler, but still very hot edge plasma flows into a remote area of the reactor, called divertor, where it is exhausted. The divertor must be designed to withstand the high heat and particle fluxes from the plasma.”

“Fusion Electricity – EFDA, November 2012” [3.1]

The power exhaust

In reactor-sized fusion devices, the problem of the power and particles exhaust is mainly related to the α -particles [3.2]. The α -particle heating, as already analysed in the Chapter 1, amounts to 20% of the fusion power and it is contained in the plasma. It is necessary to transfer this huge heat load outside the plasma, transmitting it to the solid surfaces. These surfaces can be either surfaces facing the main plasma, when this one is in the limiter configuration, or surfaces constituting a divertor system¹.

The divertor is therefore subject to a severe difficulty arising from the narrowness of the scrape-off layer channel, which transmits an enormous heat flux. For this reason, addressing the power exhaust is one of the most challenging issues for the future reactors realisation.

3.1 The plasma exhaust

In a tokamak, the magnetic confinement of the plasma is the result of the superposition of the toroidal magnetic field, generated by external conductors, and the poloidal one created by the toroidal current induced into the plasma by an external transformer. The latter is not sufficient to confine the plasma; therefore, additional external conductors are

¹ In the following, only the divertor configuration will be analysed in detail.

needed to produce a stronger poloidal magnetic field. This allows the realization of a poloidal magnetic field null point inside the chamber, confining the plasma into a closed region delimited by the so called “Last Closed Flux Surface” (LCFS). The resulting plasma magnetic configuration, called “divertor”, is one of the most promising. **Figure 3.1** shows a single-null poloidal divertor configuration establishing some of the divertor nomenclature that will be used in the following.

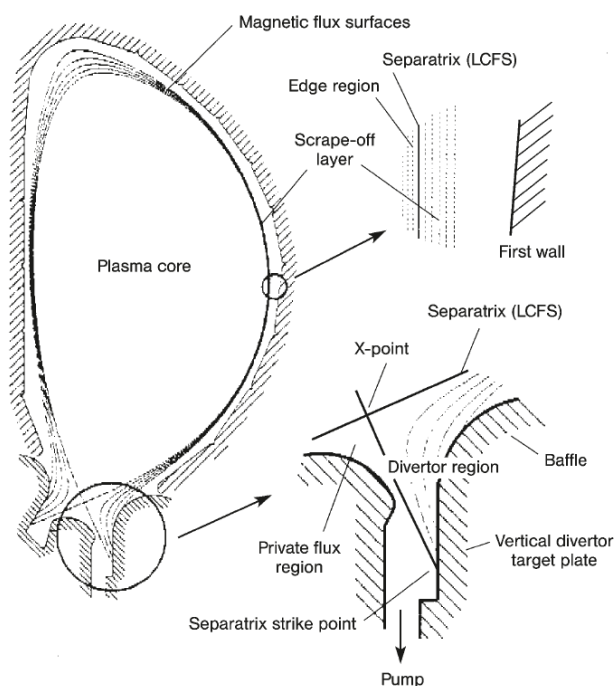


Figure 3.1: A single-null poloidal divertor configuration.

Despite the “closed nature” of the divertor plasma, a certain amount of charged particles leaves the confined plasma because of the gradients existing in the core region and is transported outside the LCFS, perpendicularly to the magnetic field, in the Scrape off layer region. The particle flow to the solid surfaces is primarily due to diffusion from the plasma core into the boundary region but also to the ionization of neutrals in the boundary plasma. Indeed, once in the boundary layer, the plasma spiral down along the magnetic field and then interacts with a solid surface. Ions, which are incident at this surface, may be

neutralized and go back or be released in other ways re-entering the plasma (*recycling*) [Section 2.2].

The Scrape-Off Layer (SOL) is a plasma region, situated just outside the plasma Last Closed Flux Surface (LCFS), characterized by open field lines starting or ending on a solid surface.

Once in this narrow region, the plasma exhaust (particles and heat) is transported, in a divertor plasma, along the magnetic field lines to the divertor plates. Transport in the SOL is very different from transport in the confined plasma due to the open field lines: it is predominantly convective (rather than diffusive) and typically, the density decays exponentially away from the LCFS. In the following, the main SOL models will be analysed in detail.

3.2 The scrape-off layer

3.2.1 A simple SOL/divertor model

The physics and the geometry of the scrape-off layer and, most in general, the divertor are rather complex and there exist many models which take into account all the phenomena occurring in that region to fully describe the behaviour of the plasma. In this thesis, a simple one-dimensional “strip model” is presented to depict the SOL and the divertor behaviour and have a rough estimate of the main plasma quantities.

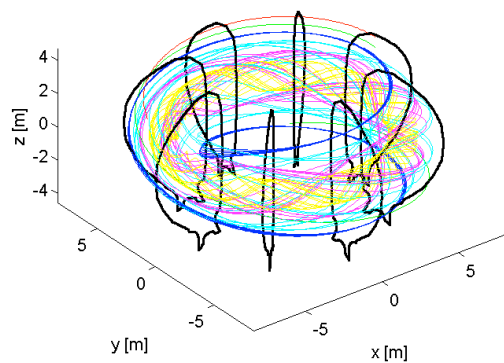


Figure 3.2: 3-D plot of typical field lines in a Tokamak. [3.4]

In the one-dimensional “strip model” [3.3] the SOL and divertor are described as a one-dimensional strip running all along the field lines, and hence sweeping the torus toroidally while gradually spiralling down in the poloidal direction (**Figure 3.2**).

According to the sheath conditions at the divertor target plates, the plasma flow reaches both the target plates and hence there must be a “flow stagnation point” ($v_{\parallel} = 0$) in the SOL²; usually, in a lower single-null (LSN) divertor configuration, this point is situated in the upper part of the plasma, and conventionally it is assumed at the outer mid-plane.

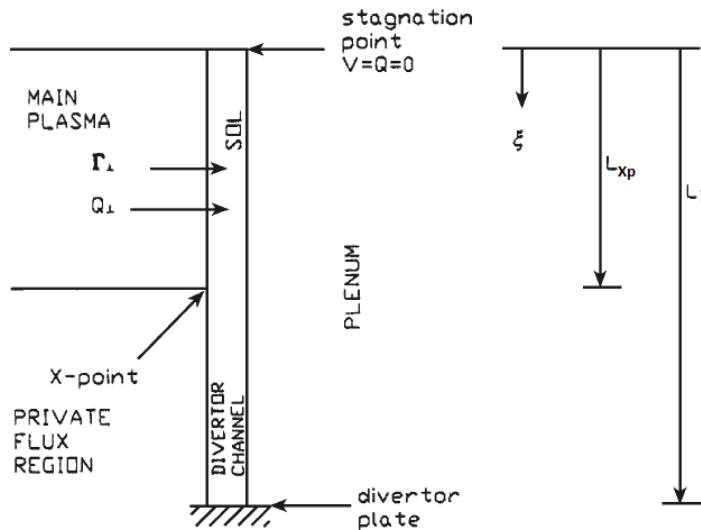


Figure 3.3: “Strip” model for SOL/divertor plasma calculation. [3.3]

It is, therefore, possible to define a coordinate ξ running along the field lines, starting at the mid-plane ($\xi = 0$) and achieving the divertor at $\xi = L_D$; this distance is also known as “connection length” (**Figure 3.3**). Between the stagnation point and X-point ($0 \leq \xi \leq L_{Xp}$), two perpendicular particles (Γ_{\perp}) and heat (Q_{\perp}) fluxes penetrate into the SOL from the core.

² Based on these considerations, it is also possible to assume the outer mid-plane as a symmetry plane for the particle and heat fluxes.

3.2.2 Radial transport and widths

It is possible to assume for the density and temperature a profile decreasing exponentially with the radius within the SOL and divertor region. Considering a radial coordinate (x) originating at the plasma separatrix ($x = r - a$)³, it results:

$$n(x) = n_{sep} \exp\left(\frac{-x}{\lambda_n}\right)$$

$$T(x) = T_{sep} \exp\left(\frac{-x}{\lambda_T}\right)$$

where the subscript “*sep*” indicates the values at the separatrix ($x = 0$). Imposing the continuity across the separatrix of both the plasma particles and heat fluxes from the core into the SOL, it is possible to determine the λ_n and λ_T widths. Furthermore, assuming that the two coefficients D_\perp (cross-field diffusion coefficient) and χ_\perp (cross-field thermal diffusivity) are independent of radius, it is possible to write the two equations:

$$\Gamma_\perp = -D_\perp \left. \frac{dn}{dx} \right|_{x=0} = \frac{D_\perp n_{sep}}{\lambda_n}$$

$$Q_\perp = -n_{sep} \chi_\perp \left. \frac{dT}{dx} \right|_{x=0} - 3T_{sep} D_\perp \left. \frac{dn}{dx} \right|_{x=0}$$

$$= \frac{n_{sep} T_{sep} \chi_\perp}{\lambda_T} + 3 \frac{n_{sep} T_{sep} D_\perp}{\lambda_n}$$

which give the two widths:

$$\lambda_n = \frac{D_\perp}{(\Gamma_\perp / n_{sep})} \tag{3.1}$$

$$\lambda_T = \frac{\chi_\perp}{(Q_\perp / n_{sep} T_{sep}) - 3D_\perp / \lambda_n}$$

The equations just obtained express the particle (λ_n) and temperature (λ_T) widths in terms of cross-field transport coefficients. Those coefficients are difficult to evaluate⁴ and hence, in practice, λ_n and λ_T are usually measured and used to deduce D_\perp and χ_\perp .

³ The parameter “*a*” is the plasma minor radius.

⁴ Usually the absolute value of D_\perp and χ_\perp is comparable to the Bohm diffusion coefficient: $D_\perp \approx \frac{T}{16eB}$ and $\chi_\perp \approx \frac{5T}{32eB}$.

In the tokamak plasmas, another width of interest is the energy width λ_q (also known as “e-folding length”) which determines the decrease of the parallel heat flux along the field lines within the SOL:

$$Q_{\parallel} \approx -k_0 T^{\frac{5}{2}} \frac{dT}{d\xi} \quad (3.2)$$

or in other words, the effective width over which power from the core plasma is distributed in the heat strike regions at the target.

A rough estimate of the energy width λ_q is given by:

$$\lambda_q \approx \frac{2}{7} \lambda_T \quad (3.3)$$

A more accurate estimate of the e-folding length is obtained with a balance between the radial heat flux crossing the separatrix from the core into the SOL, Q_{\perp} , and the parallel heat flux along the field lines in the SOL, Q_{\parallel} :

$$-\nabla \cdot Q_{\perp} \approx \frac{Q_{\perp}}{\lambda_q} = \nabla \cdot Q_{\parallel} \approx \frac{Q_{\parallel}}{L_D}$$

Achieving:

$$\lambda_q = \left[\frac{\chi_{\perp}/\lambda_T + 3D_{\perp}/\lambda_n}{\chi_{\parallel}/L_D} \right] L_D$$

As it is possible to observe in **Figure 3.1**, because of the low value of the poloidal magnetic field in the divertor region, the field lines leaving the SOL expand in front of the target tiles. This “flux expansion” could be roughly taken into account applying a flux expansion factor (f_x) to the e-folding calculated in the SOL region.

More recently, experimental measurements by means of infrared thermography of the SOL power decay length (λ_q) have been estimated from analysis of fully attached divertor heat load profiles from two tokamaks, JET and ASDEX Upgrade [3.5]. An empirical scaling reveals the parametric dependency $\lambda_q (mm) = 0.73 B_T^{-0.78} q_{cyl}^{1.2} P_{SOL}^{0.1} R_{geo}^0$, where $B_T (T)$ describes the toroidal magnetic field, q_{cyl} the cylindrical safety factor, $P_{SOL} (MW)$ the power crossing the separatrix and $R_{geo} (m)$ the major radius of the device. A comparison of these measurements to a heuristic particle drift-based

model shows satisfactory agreement in both absolute magnitude and scaling. Extrapolation to ITER gives $\lambda_q = 1 \text{ mm}$ [3.5].

3.2.3 Parallel transport

In order to properly model the parallel transport along the field lines, most of the phenomena occurring in the SOL and the divertor region (e.g. ionization, recycling, atomic and molecular processes, etc.) are taken into account. Note that the electron and ion temperature and density are always assumed to be equal ($T_e = T_i = T$ and $n_e = n_i = n$).

A one-dimensional continuity equation can be derived, neglecting the drifts, from the two-dimensional (ξ, x) fluid continuity equation for the strip by integrating over x :

$$\frac{d(nv)}{d\xi} = \frac{\Gamma_{\perp} H_{SOL}}{\lambda_n} + n(n_0 \langle \sigma v \rangle_{ion} - n \langle \sigma v \rangle_{rec}) \quad (3.4)$$

and using the boundary condition of an incident particle flux from the core for $0 \leq \xi \leq L_{Xp}$,

$$\begin{aligned} n(\xi = 0) &= n_{SOL} \\ n(\xi = L_D) &= n_D \end{aligned}$$

Γ_{\perp} is the perpendicular particle flux from the core across the separatrix into the SOL (distributed across a radial particle width λ_n to take into account the radial transport particle loss). This flux is multiplied by the quantity H_{SOL} , the Heaviside function, which is unity for $0 \leq \xi \leq L_{Xp}$ and zero elsewhere, indicating that the particles penetrate from the core into the SOL only in the region starting from the stagnation point and ending at the X-point. The term $nn_0 \langle \sigma v \rangle_{ion}$ represents the ionization sources whereas $n^2 \langle \sigma v \rangle_{rec}$ are the recombination losses of the ions. The quantity n_0 is the total neutral atom density.

Similarly, it is possible to obtain a one-dimensional momentum equation:

$$\frac{d(2nT + nmv^2)}{d\xi} = -mnvn_0^c \langle \sigma v \rangle_{at} - mn^2 v \langle \sigma v \rangle_{rec} \quad (3.5)$$

in which the quantities $p = nT$ and n_0^c represent respectively the ion pressure and the “cold” or previously uncollided neutral atom density, with the boundary conditions:

$$v(\xi = 0) = 0$$

$$v(\xi = L_D) = c_{sD}$$

respectively at the stagnation point and at the divertor. For this second condition, the plasma velocity is assumed equal to the speed of sound (c_s), according to the sheath theory. The term $n_0^c \langle \sigma v \rangle_{at}$ refers to the charge exchange and elastic scattering phenomena.

The one-dimensional energy equation can be written as:

$$\begin{aligned} \frac{dQ}{d\xi} = \frac{Q_{\perp}(0)}{\lambda_E} H_{SOL} - n_z n L_z + E_{ion} n n_0 \langle \sigma v \rangle_{ion} \\ - f I_{ion} n^2 \langle \sigma v \rangle_{rec} \\ + \frac{3}{2} (T - T_0^c) n n_0^c \langle \sigma v \rangle_{at} \end{aligned} \quad (3.6)$$

with the stagnation and sheath boundary conditions:

$$Q(\xi = 0) = 0$$

$$Q(\xi = L_D) = n_D c_{sD} (\gamma_{SH} T_D)$$

Q_{\perp} is the perpendicular heat flux from the core across the separatrix into the SOL (distributed across a radial particle width λ_E to take into account the radial transport heat loss). The second term represents the impurity radiation (and bremsstrahlung) cooling (f is the fraction of the ionization potential released upon recombination that is adsorbed in the plasma) whereas the last three atomic physics terms represent ionization cooling, recombination heating, and charge-exchange plus elastic scattering cooling of the plasma. The quantity $\gamma_{SH} \approx 7 \div 8$ is the sheath heat transmission coefficient.

In the attached plasmas, as those considered so far, the electron conduction dominates the ion transport (as already seen in formula (3.2)), therefore the heat transport parallel to the magnetic field lines can be written as:

$$Q_{\parallel} \approx Q_e = -k_0 T^{\frac{5}{2}} \frac{dT}{d\xi} \quad (3.2)$$

with boundary conditions:

$$T(\xi = 0) = T_{SOL}$$

$$T(\xi = L_D) = T_D$$

Where k_0 is the electron conduction coefficient.

3.2.4 Solution of plasma equations

Solutions to the equations so far obtained can be found under simplifying assumptions. For example, assuming the plasma in a “sheath-limited” regime, the density derivatives in the Eqs. (3.4) and (3.5) can be neglected and therefore, integrating under the boundary conditions already provided, it is possible to obtain an equation for the normalized velocity (Mach number) as a function of position:

$$M(\xi) = \alpha^{0.5} \tan \left[\frac{\alpha(\xi)}{\alpha_D} \right]^{0.5} \tan^{-1} \left(\frac{1}{\alpha_D^{0.5}} \right) - 0.5 \int_{\xi}^{L_D} \frac{v_{tot} d\xi'}{c_s(\xi')} \quad (3.7)$$

where:

$$M(\xi) \equiv \frac{v(\xi)}{c_s(\xi)} \equiv \frac{v(\xi)}{\sqrt{2T(\xi)/m}}$$

with sheath boundary condition of a sonic velocity at the divertor target plates, $M(L_D) = 1$, and

$$\alpha(\xi) \equiv \frac{n_0 \langle \sigma v \rangle_{ion} - n \langle \sigma v \rangle_{rec} + \frac{\Gamma_{\perp} H_{SOL}}{n \lambda_n}}{n_0 \langle \sigma v \rangle_{ion} + n_0^c \langle \sigma v \rangle_{at} + \frac{\Gamma_{\perp} H_{SOL}}{n \lambda_n}}$$

The quantity $v_{tot} = n_0 \langle \sigma v \rangle_{ion} + n_0^c \langle \sigma v \rangle_{at}$.

Differently, the equations. (3.4) and (3.5) could also be solved for the density as a function of the Mach number:

$$n(\xi) = n_D M^2(\xi) e^{A(\xi)} \quad (3.8)$$

where:

$$A(\xi) = 0.5(1 - M^2(\xi)) + \int_{\xi}^{L_D} \sqrt{\frac{2m}{T}} M v_{tot} d\xi'$$

The heat conduction equation (3.2) can be used in the (3.6) to obtain the temperature distribution in the strip as a ξ function:

$$\begin{aligned} T(\xi) = & \left[T_D^{\frac{7}{2}} + \frac{7}{2k_0} \left\{ \int_{\xi}^{L_D} d\xi' \int_0^{\xi'} n_z n L_z d\xi'' \right. \right. \\ & + \int_{\xi}^{L_D} d\xi' \int_0^{\xi'} n \left(\frac{3}{2}(T - T_0^c) v_{at} \right. \\ & \left. \left. + E_{ion} v_{ion} \right) \xi'' \right. \\ & \left. \left. - \int_{\xi}^{L_D} d\xi' \int_0^{\xi'} \frac{Q_{\perp}(0)}{\lambda_E} H_{SOL} d\xi'' \right\} \right]^{\frac{2}{7}} \end{aligned} \quad (3.9)$$

3.2.5 Two-Point Model

The equations (3.4) - (3.6) can be integrated over the SOL-divertor “strip” in the range $0 \leq \xi \leq L_D$ with the suitable boundary conditions. This procedure leads to a set of equations that can be solved for the temperature and density in two relevant points of the strip:

- “upstream” at the stagnation point or plasma mid-plane (now denoted by the “U” subscript);
- “downstream” at the divertor target plate (denoted by “D” subscript).

Integrating the equation (3.6), it is possible to obtain an integral energy balance equation:

$$n_D c_{SD} \gamma_{SH} T_D = \frac{\langle Q_{\perp} \rangle L_{SOL}}{\lambda_E} - \Delta Q_{rad} - \Delta Q_{at} \quad (3.10)$$

where:

$$\langle Q_{\perp} \rangle = \int_0^{L_{xp}} Q_{\perp}(0, \xi) d\xi / L_{xp}$$

is the average value of the heat flux entering from the core into the SOL,

$$\Delta Q_{rad} = \int_0^{L_D} n_z n L d\xi \equiv f_z \int_0^{L_D} n^2 L_z d\xi$$

is the total impurity radiation in the SOL-divertor divided by the width, and

$$\Delta Q_{at} = \int_0^{L_D} n \left(\frac{3}{2} (T - T_0^c) v_{at} + E_{ion} v_{ion} - f I_{ion} v_{rec} \right) d\xi$$

is the net energy loss by atomic physics reactions in the SOL-divertor region, divided by the width.

Integrating the equation (3.4), it is possible to obtain an integral particle balance equation:

$$n_D c_{sD} = \frac{\langle \Gamma_{\perp} \rangle L_{SOL}}{\lambda_n} + \Delta N_{at} \quad (3.11)$$

where:

$$\langle \Gamma_{\perp} \rangle = \int_0^{L_{xp}} \Gamma_{\perp} (0, \xi) d\xi / L_{xp}$$

is the average value of the particle flux entering from the core into the SOL,

$$\begin{aligned} \Delta N_{at} &= \int_0^{L_D} n (n_0 \langle \sigma v \rangle_{ion} - n \langle \sigma v \rangle_{rec}) d\xi \\ &= n_D \int_0^{L_D} M^2 e^A (n_0 \langle \sigma v \rangle_{ion} - n_D M^2 e^A \langle \sigma v \rangle_{rec}) d\xi \end{aligned}$$

is the net ionization minus recombination rate in the SOL-divertor region, divided by the width.

Equations (3.10) and (3.11) can be solved for the plasma temperature just in front of the divertor target plate

$$T_D = \frac{1}{\gamma_{SH}} \frac{\langle Q_{\perp} \rangle \lambda_n}{\langle \Gamma_{\perp} \rangle \lambda_E} \left[\frac{1 - \frac{(\Delta Q_{rad} + \Delta Q_{at})}{\langle Q_{\perp} \rangle L_{Xp} / \lambda_E}}{1 + \frac{\Delta N_{at}}{\langle \Gamma_{\perp} \rangle L_{Xp} / \lambda_n}} \right] \quad (3.12)$$

The “upstream” temperature, at the core mid-plane separatrix, T_U , can be found by using the equation (3.2) to evaluate the (3.6) at $\xi = 0$ (assuming that the temperature does not vary too much between the stagnation point and the mid-plane):

$$T_U = \left\{ T_D^{\frac{7}{2}} + \frac{7}{2k_0} \left[\langle Q_{\perp} \rangle L_{Xp} \left(L_D - \frac{1}{2} L_{Xp} \right) - (\Delta Q_{rad} + \Delta Q_{at}) \frac{1}{2} L_D \right] \right\}^{\frac{2}{7}} \quad (3.13)$$

Integrating the equation (3.5), it is possible to obtain an integral momentum balance equation:

$$n_U = n_D \left[\frac{2T_D + \frac{1}{2} (\Delta M_{at} / n_D) (\lambda_n / \lambda_{nT})}{T_U} \right] \equiv n_D K_D SOL \quad (3.14)$$

where:

$$\lambda_{nT} = \frac{\lambda_n}{1 + \lambda_n / \lambda_{nT}}$$

and

$$\begin{aligned} \frac{\Delta M_{at}}{n_D} &= \int_0^{L_D} \frac{n}{n_D} (n_0^c \langle \sigma v \rangle_{at} + n \langle \sigma v \rangle_{rec}) m v d\xi \\ &= \int_0^{L_D} M^2 e^{A(\xi)} (n_0^c \langle \sigma v \rangle_{at} - n \langle \sigma v \rangle_{rec}) m v d\xi \end{aligned}$$

is the momentum loss by the flowing plasma due to charge-exchange, elastic scattering and recombination reactions, in which the resulting neutral carries the momentum to the wall.

Finally, these equations can be used to obtain an explicit solution for the plasma density just in front of the divertor target plate

$$\begin{aligned}
n_D &= \frac{1}{c_{SD}^{0.5}} \left[\frac{\langle \Gamma_{\perp} \rangle L_{Xp}}{\gamma_n K_{D \text{ SOL}}} + \frac{\Delta N_{at}}{n_D} \right]^{0.5} \\
&= \frac{1}{c_{SD}^{0.5}} \left[\frac{\langle \Gamma_{\perp} \rangle L_{Xp} + \Delta N_{at} / \beta}{\lambda_n f_x} \right]
\end{aligned} \tag{3.15}$$

where $\gamma_n = \lambda_n / n_U = D_{\perp} / \Gamma_{\perp}$, $\beta = B_{\theta} / B_{\phi}$ and f_x is a flux expansion factor.

The set of nonlinear Eq. (3.12) for T_D , Eq. (3.13) for T_U , Eqs. (3.1) for the lambda's, Eq. (3.15) for n_D , and Eq. (3.14) for n_U constitute a self-consistent model for calculating the plasma density and temperature along the separatrix at two points (the mid-plane, or stagnation point, and in front of the divertor target).

3.3 Plasma operative regimes

Divertor plasmas are observed to operate in three main “regimes”:

- 1) a “*sheath-limited*” or “*linear*” regime in which the plasma pressure is essentially constant along the field lines and there is little difference in the plasma temperatures at the SOL (stagnation point) mid-plane and just in front of the divertor target;
- 2) a “*high recycling*” regime in which pressure is essentially constant along the field lines but the density increases significantly at the divertor in inverse proportion to the decrease in temperature;
- 3) a “*detached*” regime in which both the density and temperature decrease sharply just in front of the divertor target plate.

It is possible to relate some of the model parameters to more familiar experimental parameters. The radial heat flux across the separatrix $\langle Q_{\perp} \rangle = P_{sep} / A_{sep}$, where P_{sep} is the total power crossing the separatrix and $A_{sep} \approx 2\pi R 2\pi a \sqrt{k}$ is the area of the separatrix. The radial particle flux across the separatrix $\langle \Gamma_{\perp} \rangle = n_p V_p / \tau_p A_{sep}$, where $V_p = 2\pi R 2\pi a^2 k$ is the plasma volume within the separatrix and τ_p is the particle confinement time within this volume. The parallel distance along the

field lines from the stagnation point to the X-point is $L_{Xp} = \pi q_{95} R$ for a single null divertor.

3.3.1 Sheath-Limited Regime

The condition that the plasma temperature will be almost the same at the mid-plane (stagnation point) and the divertor target requires that the second term in Eq. (3.13) be small compared to $T_D^{\frac{7}{2}}$. This condition may be written as:

$$\begin{aligned} & \frac{7}{2k_0} \left(\frac{n_p V_p}{\tau_p} \right)^{\frac{7}{2}} \frac{q_{95}}{4\pi^2 \alpha \sqrt{k} \Delta_E} \\ & \times \left[\left(L_D - \frac{1}{2} L_{Xp} \right) - \frac{(\Delta Q_{rad} + \Delta Q_{at}) \Delta_E 4\pi^2 \alpha \sqrt{k} L_D}{q_{95} P_{sep}} \right] \\ & \times \left[P_{sep} \left(\frac{1}{\gamma_{SH}} \frac{\Delta n}{\Delta_E} \right)^{\frac{7}{2}} \left(\frac{1 - \frac{(\Delta Q_{rad} + \Delta Q_{at}) \Delta_E 4\pi^2 \alpha \sqrt{k}}{q_{95} P_{sep}}}{1 + \frac{\Delta N_{at} 2 \Delta_n \tau_p}{n_p \alpha \sqrt{k} q_{95} \pi R}} \right)^{\frac{7}{2}} \right]^{-1} < 1 \end{aligned}$$

From this relation it is easy to understand why *the sheath-limited regime is associated experimentally with high power crossing the separatrix and low core plasma density, n_p* . Atomic physics cooling is more significant in reducing the denominator (enters to 7/2 power) than in reducing the numerator in Eq. (3.16), so the presence of recycling neutrals and impurities would be expected to shift the boundary between the sheath-limited and high recycling regimes towards higher powers crossing the separatrix and lower core plasma densities. Recycling neutrals further shift this boundary in the same direction by contributing to the build up of the plasma density (the ΔN_{at} term).

3.3.2 Detached regime

At the other limit, *detached plasma operation requires that essentially all of the heat transported across the separatrix into the SOL be radiated or otherwise removed by atomic physics processes, i.e. that*

$$\frac{\Delta Q_{rad} + \Delta Q_{at}}{\langle Q_{\perp} \rangle L_{xp} / \Delta_E} \rightarrow 1 \quad (3.17)$$

which may be written in the limit $n_D T_D \rightarrow 0$ in a form

$$\frac{(\Delta Q_{rad} + \Delta Q_{at}) \chi_{\perp} \frac{1}{2} \Delta M_{at}}{(P_{sep}/A_p)^2 q_{95} \pi R} \left(\frac{1}{1 - 3n_p V_p T_U / P_{sep} \tau_p} \right) \rightarrow 1 \quad (3.18)$$

This relation illustrates the requirement for momentum exchange of the plasma with the recycling neutrals (the ΔM_{at} term) in order to detach. Equation (3.18) is also important because it suggests *four possible paths to detachment*:

- (1) increase impurity concentration or L_z (impurity species);
- (2) increase the recycling neutral concentration to increase ΔQ_{at} and ΔM_{at} ;
- (3) reduce the power flux (P_{sep}/A_{sep}) transported across the separatrix (e.g. by increased radiation inside the separatrix, by reduced auxiliary heating or by increased plasma surface area);
- (4) increase the connection length $L_{xp} = \pi q_{95} R$.

The fraction of the heat transported across the separatrix into the SOL that is radiated or otherwise removed to the wall by atomic physics processes is

$$\begin{aligned} f_{ex} &\equiv \frac{(\Delta Q_{rad} + \Delta Q_{at})}{\langle Q_{\perp} \rangle L_{xp} / \Delta_E} \\ &= 1 - \frac{2}{7} n_D \frac{\left(2T_D + \frac{1}{2} \frac{\Delta N_{at}}{n_D} \frac{\Delta n}{\Delta n_T} \right) \left(\chi_{\perp} + 3D_{\perp} \frac{\Delta T}{\Delta n} \right) (\gamma_{SH} T_D)}{\langle Q_{\perp} \rangle^2 L_{xp}} \end{aligned} \quad (3.19)$$

This expression makes clear that *the fraction of the plasma exhaust power that is “radiated” in the divertor and SOL can approach unity for a detached plasma ($n_D \rightarrow 0$).*

3.3.3 High recycling regime

Also in the high recycling regime the exhaust fraction, f_{ex} , approaches unity as $T_D \rightarrow 0$. The maximum fraction of the power transported across

the separatrix that can be “radiatively” exhausted in the divertor and SOL decreases with increasing core plasma density and with increasing power across the separatrix, and decreases with recycling neutral concentration when ionization dominates recombination ($\Delta N_{at} > 0$). The frictional plasma momentum dissipation due to reactions with recycling neutrals is important for maximizing the fraction of the power radiated by impurities from the divertor and SOL plasma. Note that Eq. (3.19) describes the fraction radiated by impurities and plasma plus the fraction transferred to the wall by neutrals that have gained energy from plasma ions by charge-exchange and elastic scattering. Although impurity radiation is usually dominant, other atomic physics reactions with recycling neutrals can exhaust up to half the power crossing the separatrix in some tokamaks.

In contrast to the situation for the detached regime, where plasma momentum loss to the recycling neutrals increases f_{ex} , in the high recycling regime plasma momentum loss to recycling neutrals decreases f_{ex} , unless recombination dominates ionization ($\Delta N_{at} < 0$).

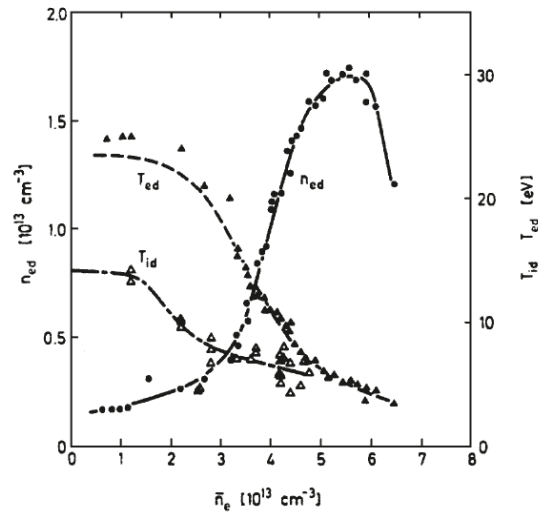


Figure 3.4: Scaling of the electron temperature and density measured by a Langmuir probe, and the ion temperature deduced from Doppler-broadened CIII radiation in the ASDEX divertor plasma.

(The decrease in $n_{ed} = n_D$ at the highest density is attributed to divertor detachment) [3.3]

3.3.4 Comparison with the experimental results

The three regimes of divertor operation are illustrated in **Figure 3.4**, where the electron density and the ion and electron temperatures measured just in front of the divertor plate for a set of ASDEX discharges with different plasma densities ($n_p = n_e$) are plotted [3.3].

3.4 Conclusions

The power produced in the plasma by ohmic heating, additional heating or fusion reactions, impinge the solid surfaces. Radiation and convection of neutrals tend to result in a uniform deposition of the power. Transport of charged particles, either by conduction or convection, results in localized power deposition at the limiters or in the divertor since the power transfer is predominantly along field lines. It is common in high power tokamak systems that the power transported to the divertor or limiter is close to the limits which solid materials can withstand. The main factors determining the integrity of a solid are firstly evaporation, leading to erosion of the surface and contamination of the plasma and secondly thermal shock, leading to the loss of structural strength of the component.

In steady state the maximum tolerable heat flux is determined by the stress due to temperature gradients between the heated surface and the coolant. Consequently, high thermal conductivity is important. Attempts have been made to combine a low sputter yield plasma-facing surface with a high heat conduction substrate. In these cases thermal stress at the brazed joint may be the limiting factor in the design.

One of the most important issues when designing divertor surfaces is the power distribution. Possible ways of reducing the power density are:

- I. transferring the energy to neutral particles before impinging the divertor targets;
- II. radiating power before impinging the divertor targets;
- III. flux expansion of the field lines as they approach the divertor target (within prescribed limits on the grazing angle);
- IV. magnetically sweeping the strike point over a width that is large compared to λ_q ;

- V. placing the target tiles at an oblique angle to the field lines (within prescribed limits on the grazing angle).

Approaches I-IV will be analysed in detail in the next sections. However, they have not yet led to a fully acceptable solution for a fusion power plant and the design of the divertor remains one of the most difficult problems in DEMO.

Concerning point V, since the power density falls approximately exponentially with radius outside the last closed flux surface, by varying the angle of the surface to magnetic field lines, it is possible to design the surface of the divertor so that the power per unit area is uniform. Since the target tiles are heated to high temperatures, there is a significant thermal expansion. This is a particular problem because the heating is non-uniform, due to the gradient of the power distribution in the scrape-off layer. To minimize stress in the tiles they are normally small. The angle of the tiles with respect to the field lines at the target is made as small as possible in order to increase the effective area of the target surface. Angles as low as 1° have been used [3.2]. However, due to the finite gap between the tiles, when the angle comes close to grazing a fraction of the tile edge is exposed to the field lines at normal incidence. This problem may be overcome by machining a chamfer on each tile and displacing each one with respect to its neighbour, so that the edges are shielded, as shown in **Figure 3.5** [3.2].

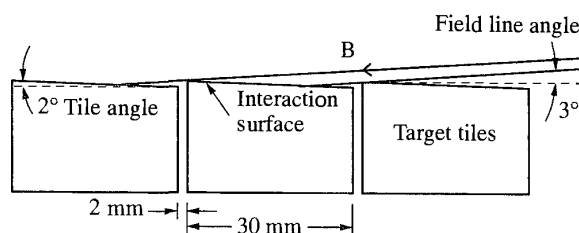


Figure 3.5: Diagram of target tiles, showing adjacent tiles displaced to protect the edges at gaps. The effective interaction area is reduced depending on the accuracy of the tile placement. [3.2]

This has the drawbacks that it works for only one field direction and it reduces the effective area of the tiles. The optimum design depends on how well the tiles can be aligned. Alignment is difficult due to thermal expansion, movement due to magnetic and vacuum forces and the large area over which the alignment is necessary.

A further problem is the erosion of the divertor target surface. Although in a divertor configuration the impurities produced by sputtering or other erosion processes are prevented from entering the confined plasma, the target erosion can still be serious. Changes in the target thickness, due both to erosion and to deposition of the eroded material elsewhere, make design of cooling systems very difficult.

References

- [3.1] “Fusion Electricity – EFDA, November 2012”
- [3.2] Wesson J., “Tokamaks – third edition”, Clarendon Press-Oxford 2004, ISBN 0 19 8509227
- [3.3] Stacey W. M., “Fusion Plasma Physics”, Wiley-VHC, ISBN 978-3-527-41134-4
- [3.4] R. Albanese et al., “Numerical Formulations for Accurate Magnetic Field Flow Tracing in Fusion Tokamaks”, CEM 2014, DOI: 10.1049/cp.2014.0211
- [3.5] T. Eich, et al., “Inter-ELM Power Decay Length for JET and ASDEX Upgrade: Measurement and Comparison with Heuristic Drift-Based Model”, PRL 107, 215001 (2011)

Chapter 4

“[...] Materials that resist heat fluxes up to 20 MW/m², which is of the same order as the heat load on the sun’s surface, have been produced for ITER. Alternative, backup divertor concepts are under investigation and need to be brought to sufficient maturity by 2030 through a dedicated experimental programme.”

“Fusion Electricity – EFDA, November 2012” [4.1]

The candidate solutions to the power exhaust issue

A reliable solution to the problem of heat exhaust is probably the main challenge towards the realisation of magnetic confinement fusion [4.1]. The main risk is that the baseline strategy pursued in ITER cannot be extrapolated to a fusion power plant. Hence, in parallel to the programme in support of the baseline strategy, a dedicated research programme on alternative solutions for the divertor was promoted by EFDA and represents one of the key points in the European roadmap pursued by EUROfusion, EFDA successor. Some concepts have already been tested at proof-of-principle level and their technical feasibility in a fusion power plant is being assessed. Since the extrapolation from proof-of-principle devices to ITER/DEMO based on modelling alone is considered too large, a dedicated test on specifically upgraded existing facilities or on a dedicated Divertor Tokamak Test (DTT) facility [4.1] will be necessary.

In this Chapter, the key concepts and the main ideas, on which the proposed techniques are based, are illustrated. One possible classification can be obtained distinguishing among:

- *Plasma “detachment”*, a physical phenomenon by which the plasma materially “detaches” from the PFCs creating a neutral gas “blanket” (also called “front”) in which the momentum and the energy are transferred from the plasma to the neutral gas;

- *Magnetic alternative configurations*, whose fundamental aim is to produce magnetic fields by which the charged particles, following the field lines, spread their energy on a broader area once they reach the plasma-facing components or dissipate great part of their energy before reaching the solid surfaces;
- *Strike-point sweeping and wobbling techniques*, by which respectively part of or the whole plasma boundary is moved periodically by external coils spreading the thermal load on a wider area;
- *Liquid metal divertor*, which solve the problem of the melting of the divertor solid surfaces occurring at the high temperatures reached in steady-state conditions. This technique, resorting to a divertor composed by liquid metals, takes advantage of melting since a liquid metal divertor does not suffer from thermal stresses and embrittlement, and no thick armour is needed.

In the following, an analysis of the principles on which each candidate solution is based and a more detailed overview will be given.

4.1 The plasma “detachment”

The so called “plasma detachment” is based on the physics analysed in the Section 3.3.2, where a “detached plasma regime” has been defined. Essentially, the divertor detachment occurs with both target density and temperature dropping to low levels. In fact, once the target is at a sufficiently low temperature, volume recombination and ion-neutral frictional drag on the parallel plasma flow become important, also reducing the density at the target, and thereby “detaching the plasma from the target” [4.3]. The “detachment” can be achieved through impurity injection and radiative cooling at high upstream plasma density.

For the reasons just mentioned, the detached plasma regime is attractive for the next generation fusion reactors, since it allows distributing the power exhaust on a much broader area and hence reducing the heat flux

on the divertor plate. Furthermore, phenomena as erosion and melting of the PFCs are avoided or, at least, reduced.

The achievement of a partially detached state at both targets represents the baseline solution for the ITER divertor. The physics and technological challenge of the ITER divertor is to demonstrate that these conditions can be sustained in a controlled manner and hence detachment will be tested, providing an assessment of its adequacy for DEMO. However, in DEMO the larger core radiation fraction required could make incompatible a comparison with ITER. If ITER will show that the baseline strategy cannot be extrapolated to DEMO, the lack of an alternative solution would delay the realisation of fusion by 10-20 years. Hence, in parallel with the necessary programme to optimise and understand the operation with a conventional divertor, e.g. by developing control methods for detached conditions, in view of the test on ITER, an aggressive programme to extend the performance of water-cooled targets and to develop alternative solutions for the divertor is necessary as risk mitigation for DEMO [4.2].

However, experimental observations ([4.4]) show that, in a low SN standard configuration, impurity and hydrogen radiation regions could move towards the X-point bringing the cold plasma to the boundary of the main plasma (**Figure 4.1**).

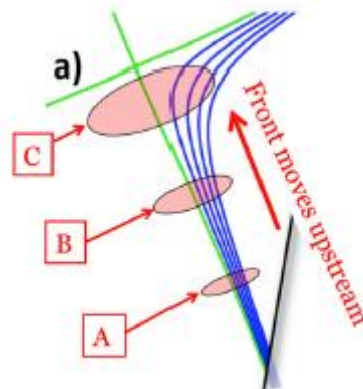


Figure 4.1: The plasma-neutral interaction area of a Standard Divertor increases as the detachment front moves toward the main X-point. Thus, energy losses increase, leading to an unstable feedback, so that the front moves toward the core X-point. [4.6]

The influx of impurities into the confined plasma cause high radiation levels from this region, which may result in the thermal instability of the whole plasma, known as MARFE (Multi-faceted Asymmetric Radiation From the Edge). Thus, ITER needs to operate in a state called partial-detachment under active feedback control [4.5] in order to balance the need for acceptable divertor target heat loads and core stability (Section 4.2.5).

4.2 The alternative magnetic divertor configurations

Conventionally, the “alternative” or “advanced” divertors are defined as magnetic geometries where a second X-point is added in the divertor region to address the serious challenges of burning plasma power exhaust¹ [4.6]. The position of the second X-point allow distinguishing among the alternative solutions. In the following, the history and the main characteristics of the fundamental magnetic alternative configurations will be described.

4.2.1 Double-Null (DN) configuration

The DN is chronologically the first alternative (to the Single Null) magnetic configuration introduced in fusion plasmas. Double null configuration produces a second first order null point in the poloidal magnetic field in the upper part of the main chamber (**Figure 4.2**).

¹ This definition is valid for the plasma realized in experimental machines. In fact, conceptually an ideal Snowflake configuration is obtained forming a second-order null point at the main plasma X-point. However, in the experimental machines, it is impossible to realize a second order null point and hence two first-order null points as close as possible are created in the poloidal magnetic field.

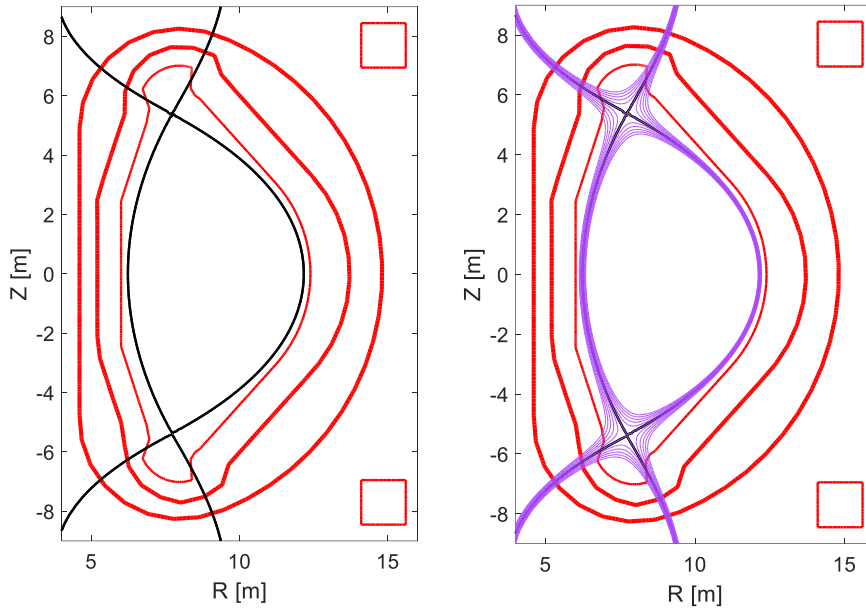


Figure 4.2: Plasma separatrix in a DEMO Double Null configuration.

The presence of a second X-point involves the need of a second divertor in the upper part of the chamber, allowing the wall interaction area to be doubled and halving the heat load reaching the divertor (compared to the SN case) [4.7] but also halving the connection length to the target. It also allows a more triangularly shaped plasma to be obtained, which is beneficial in obtaining high β and high energy confinement [4.7]. A detailed comparison between the main advantages and the stability properties of DN and SN configurations will be presented in Chapter 4.

4.2.2 X-Divertor (XD) configuration

The XD was introduced in 2004 [4.8]. In **Figure 4.3**, a few of the representative 2004 XD configurations from the original paper are displayed; (a) NSTX and (b) ITER.

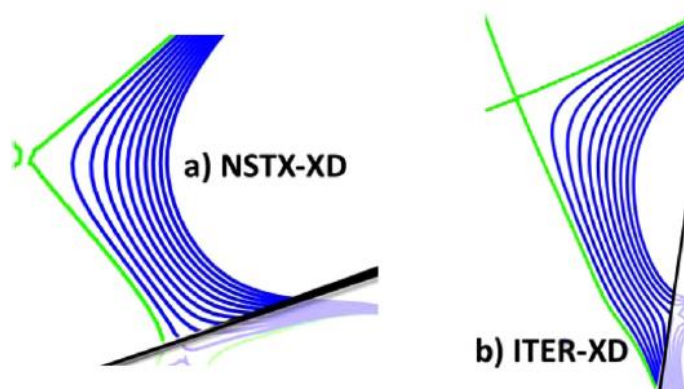


Figure 4.3: Flux plots of the 2004 XD equilibria, regenerated using CORSICA for (a) NSTX and (b) ITER. To emphasize the physically relevant regions where power is exhausted, only SOL field lines are shown in bold. [4.6]

The most important characteristics of the XD are listed below:

- a) The XD configuration is created by “inducing a second axisymmetric X-point downstream of the main plasma X-point.” [4.8]
- b) The beneficial result is that “field line lengths from the core X-point to the wall can be increased and flux expansion can be increased.” The physical consequence of these characteristics was predicted to be a greatly reduced heat flux on the divertor plate. It was also suggested in [4.7] that the XD may allow a stable detached operation.
- c) The new X-point produced a new geometry in the SOL flux surfaces—the flux surfaces flared outward, rather than contract inward as in a Standard Divertor (**Figure 4.4**).
- d) The name X-Divertor succinctly describes the physical essence of the configuration - the downstream SOL interacting with a new X-point.

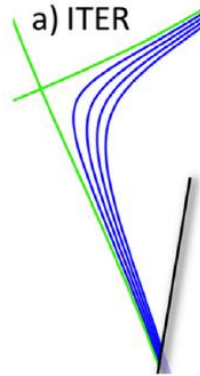


Figure 4.4: Standard Divertor flux surfaces, for ITER equilibria generated with the free boundary code CORSICA. Standard Divertors have convergent flux surfaces [4.6]

4.2.3 Snowflake Divertor (SFD)

The SFD family, built around the basic configuration (to be called pure Snowflake) that creates a second order null at the main plasma X-point, was introduced in 2007. Such a second order null in the core X-point produces a six-fold symmetry in the magnetic field within the divertor region, leading to the succinctly descriptive name “Snowflake.” The pure Snowflake was complemented by two variants— “plus” and “minus” in the first publications on the subject [4.9] and [4.10] (see **Figure 4.5**).

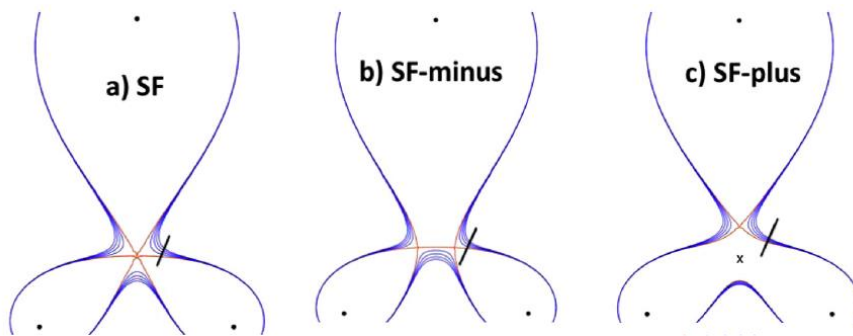


Figure 4.5: The exact Snowflake (SF), the Snowflake minus (SFm), and the Snowflake plus (SFp) configurations from 2007–2008 [4.9], [4.10]. The flux expansion is greatly increased in the region near the core X-point, but rapidly decreases downstream so that the SOL is strongly convergent (even more than for a Standard Divertor). [4.6]

These variants do not have one second order null; instead, they have two first order nulls (like the XD). The two nulls are placed relative to each other so that the advantages of the pure Snowflake, as the enormous flux expansion and increase in the line length in the vicinity of the two nearby X-points, may be maintained while its major problem -instability to small perturbations- is overcome.

Unlike the X-Divertor (**Figure 4.3**), in the Snowflake Divertors the flux surfaces in the power exhausting SOL region are all convergent in **Figure 4.5**.

4.2.4 Super-X Divertor (SXD)

In the same year as the Snowflake (2007), a more advanced variant of the XD, named the “Super-X” divertor (SXD, **Figure 4.6**), was presented; the latter reaches even a greater flux expansion by superposing toroidal expansion (by placing the divertor plate at the maximum possible major radius) on the poloidal flux expansion [4.11]-[4.13]. The name reflects the intended function: modification of the X-Divertor concept for “superior” flux expansion and line length.

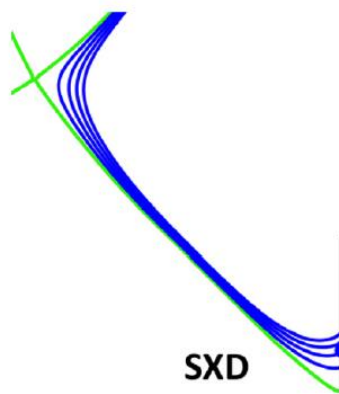


Figure 4.6: SXD with both poloidal and toroidal flux expansions near divertor plate at large major radius R . [4.6]

4.2.5 Effects of the advanced magnetic configurations on the detachment front stability

As already mentioned in the Section 4.1, experimental observations [4.4] show that, in a low SN standard configuration, impurity and hydrogen radiation regions in divertor plasmas can move towards the X-point as detachment proceeds bringing the cold plasma [sometimes termed an X-point Multifaceted Asymmetric Radiation From the Edge (MARFE)] to the boundary of the main plasma. The presence of a cold, highly radiating plasma at the edge is suspected of causing deleterious effects on H-mode confinement, and on disruption likelihood.

The advanced divertors, as described so far, modify the magnetic field structure in the same region where the detachment front progresses from the divertor plate to the core X-point. Physical arguments supported by preliminary experiments on the Snowflake (TCV) and X-Divertor (NSTX and DIII-D) magnetic advanced configurations [4.6] show that the differences in the stability behaviour of the detachment front depend on the divertor geometry. It is therefore possible distinguishing the three classes of divertor geometries:

- the geometries with convergent flux surfaces (like a Standard Divertor);
- the geometries where field lines are even more rapidly convergent (SFD);
- the geometries with flux surfaces more slowly convergent, or divergent, near the plate (XD).

The stabilizing effect on the movement of the detachment front from upstream thermal conduction results being largest for the X-Divertor, smallest for the SFD, and intermediate for the Standard Divertor (**Figure 4.7**).

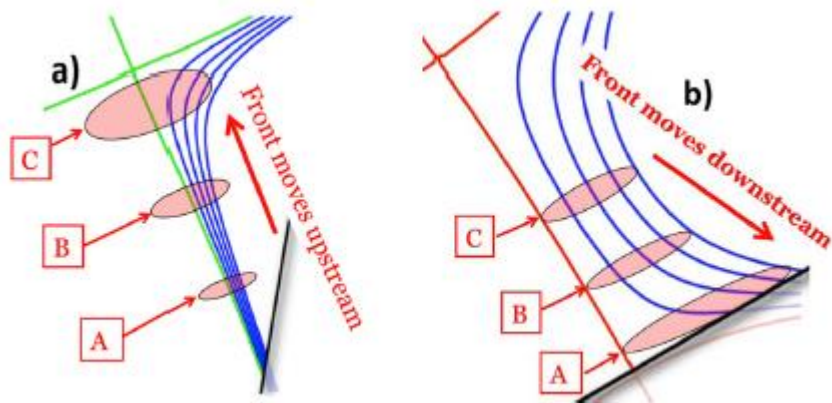


Figure 4.7: The plasma-neutral interaction area of (a) a Standard Divertor increases as the detachment front moves toward the main X-point. Thus, energy losses increase, leading to an unstable feedback, so that the front moves toward the core X-point. An XD geometry (b) with flared field lines near the plate reverses this feedback so the front could be arrested near the divertor plate. [4.6]

This leads to the prediction that *the X-Divertor configuration can attain higher levels of radiative dissipation than a Standard Divertor, without suffering degradation of H-mode confinement.*

Therefore, the plasma detachment coupled to an alternative magnetic configuration offers a promising solution to the power exhaust issue although an active feedback control system [4.5] could be necessary for an efficient detachment front stabilization.

4.3 The strike-point sweeping and the wobbling techniques

Another possibility for the mitigation of power exhaust is to perform a movement of part or whole plasma boundary, spreading the thermal load over a wider area.

- The so-called “strike point sweeping” is a periodical movement of the strike points realized through dedicated coils [4.14]. This technique has been applied to JET in the past, showing significant advantages for various configurations of the divertor. An efficient

strike point sweeping provides a movement of the only region of plasma boundary close to the X-point, keeping the rest of the shape practically unchanged. Conversely, any movement of the strike points would have an undesired effect on the rest of the shape, e.g. leading to loss of coupling with additional heating sources, or at least requiring an extra effort to the shape controller;

- Unlike the strike-point sweeping, in the “wobbling” technique the whole plasma is displaced periodically in a rigid way.

Further details on strike-point sweeping and wobbling techniques are given in Chapter 6.

4.4 The liquid metal divertor

The challenging requirements imposed on divertors by the steady state operational conditions of the fusion reactors motivated examination of alternatives to solid surface divertors, such as liquid metals as divertor neutralizer materials [4.15]. Ignoring re-deposition (to be more conservative, since it may not be spatially uniform) and self-sputtering, the physical sputtering leads to a very high erosion rate. For a tungsten plate (the most promising among solid divertor materials) the erosion rate may be very high. Liquid metal divertors have some unquestionable advantages, as the self-cooling and self-annealing properties, which eliminate the design conflict between the desirability of a thicker plate to withstand sputtering erosion and a thin plate to meet the heat transfer limits associated with the solid surface divertors.

Liquid metal divertors have also other merits, examples of which are:

- 1) providing a degree of capability in controlling neutral particle recycling to the plasma, which may yield a cleaner main plasma and, therefore, a longer energy confinement time [4.15]; on the other hand, this can also lead to unwanted retention;
- 2) providing a liquid metal vapour cloud which enhances the protection of the divertor system and may also block the flight of sputtered or evaporated liquid metal plate atoms into the main plasma [4.15];

3) an expected lower edge plasma temperature compared with that of the promising solid metal divertor materials [4.15].

Several reference designs have been proposed during the last years [4.15]. These include the liquid metal protective film divertor (**Figure 4.8**), the Ga droplet curtain (shower) divertor (**Figure 4.9**) and the liquid metal pool divertor (**Figure 4.10**).

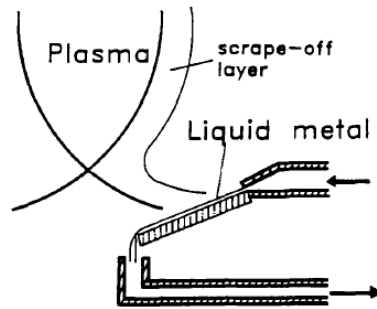


Figure 4.8: Liquid metal protective film divertor.

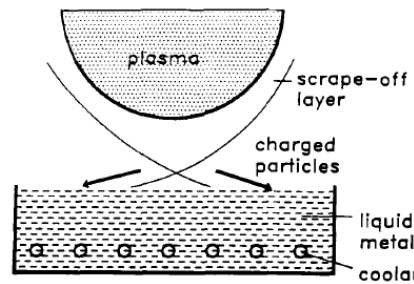


Figure 4.10: Liquid metal pool type divertor.

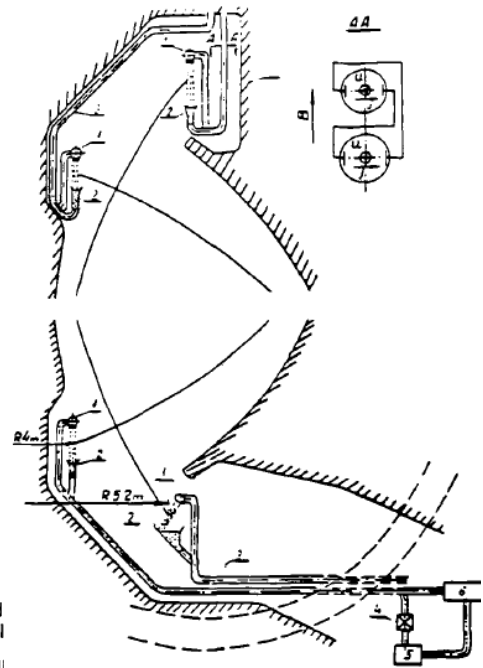


Figure 4.9: Liquid gallium droplet curtain divertor.

The crucial question to solve is how to counteract the Lorentz force as it was put in evidence in the DIII-D experiments with a lithium sample exposed in the lower divertor region [4.16]. The problem of the mechanical stabilization of liquid metal against $j \times B$ forces has been faced and solved in the Russian Federation where a new concept for the metal confinement based on a capillary porous system (CPS) in limiter configuration [4.17] has been developed and implemented using lithium as liquid element. In particular, the idea of combined lithium limiter with thin CPS coating as a solution of the heat removal problem was realized in the T-11M tokamak [4.18], as shown in **Figure 4.11** and

Figure 4.12. The ability of capillary forces to confine the liquid Li in the CPS limiter during disruption was demonstrated.

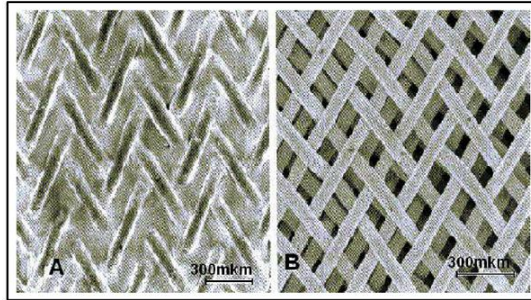


Figure 4.11: View of the 100 μm (mkm) CPS with (A) and without (B) Li filling (top). [4.18]

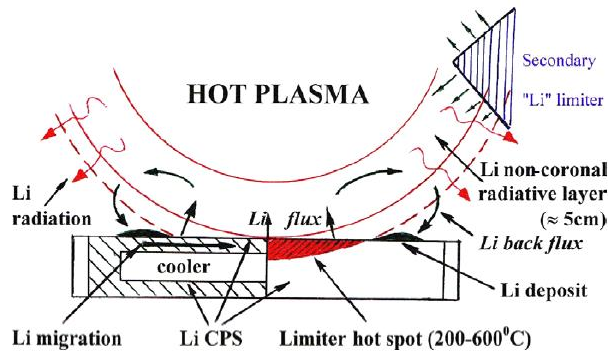


Figure 4.12: A principal scheme of lithium-limiter interaction with a tokamak plasma. [4.18]

This configuration for a liquid metal divertor is also under analysis in FTU², in which a liquid lithium limiter has been experimentally tested [4.19], and in EAST³ [4.20].

The results of the experimental tests will determine if liquid metals are a serious candidate to solve the problem of plasma wall interaction.

² The Frascati Tokamak Upgrade (FTU) is a tokamak operating in Frascati, Italy.

³ The Experimental Advanced Superconducting Tokamak (EAST) is reactor device in Hefei, China.

References

- [4.1] “Fusion Electricity – EFDA, November 2012”
- [4.2] “DTT - Divertor Tokamak Test facility”, ISBN: 978-88-8286-318-0
- [4.3] Stangeby P. C., “The Plasma Boundary of Magnetic Fusion Devices”, IOP Publishing Ltd 2000, ISBN 0 7503 0559 2
- [4.4] Krasheninnikov S. I., et al., “Stability of the detachment front in a tokamak divertor”, *Journal of Nuclear Materials* 266±269 (1999) 251±257
- [4.5] E. Kolemen et al. “Heat Flux Management via Advanced Magnetic Divertor Configurations and Divertor Detachment”, *J. Nucl. Mater.* 463 1186 (2015)
- [4.6] Kotschenreuther M., et al., “Magnetic geometry and physics of advanced divertors: The X-divertor and the snowflake”, *PHYSICS OF PLASMAS* 20, 102507 (2013)
- [4.7] Wesson J., “Tokamaks – third edition”, Clarendon Press-Oxford 2004, ISBN 0 19 8509227
- [4.8] Kotschenreuther M., et al., in “Proceedings of the 20th International Conference on Fusion Energy”, Vilamoura, Portugal (International Atomic Energy Agency, Vienna, 2004), IC/P6-43.
- [4.9] D. Ryutov, *Phys. Plasmas* 14, 064502 (2007).
- [4.10] D. Ryutov, R. Cohen, T. Rognien, and M. Umansky, *Phys. Plasmas* 15, 092501 (2008).
- [4.11] M. Kotschenreuther, P. Valanju, and S. Mahajan, *Bull. Am. Phys. Soc.* 53, 11 (2007).
- [4.12] P. Valanju, M. Kotschenreuther, and S. Mahajan, in Invited talk at APSDPP Meeting (2008) [*Phys. Plasmas* 16, 056110 (2009)].
- [4.13] P. Valanju, M. Kotschenreuther, and S. Mahajan, *Fusion Eng. Des.* 85(1), 46 (2010).
- [4.14] Fabio Villone and contributors to the EFDA-JET Workprogramme, “A model-based strike point sweeping technique applied to JET”, *Plasma Phys. Control. Fusion* 46 (2004) 1375–1392
- [4.15] Liao C., Kazimi M.S., “On the Design of Liquid Metal Divertors”, *Journal of Fusion Energy*, Vol. 13, No. 1, 1994
- [4.16] J.N. Brooks et al *Fus. Sci. Tech.* 47 (2005) 669-677

-
- [4.17] V.A. Evtikhin et al. *Fus. Eng. Des* 56-57 (2001) 363-367
- [4.18] Mirnov S. V. et al., “Experiments with lithium limiter on T-11M tokamak and applications of the lithium capillary-pore system in future fusion reactor devices”, *Plasma Phys. Control. Fusion* 48 (2006) 821–837
- [4.19] G. Mazzitelli et al., “Status and Perspectives of the Liquid Material Experiments in FTU and ISTTOK”, <http://www.afs.enea.it/vlad/Papers/mazzitelli08iaea.pdf>
- [4.20] J. S. Hu, et al., “First results of the use of a continuously flowing lithium limiter in high performance discharges in the EAST device”, *Nucl. Fusion* 56 (2016) 046011 (14pp)

Chapter 5

“The courage to imagine the otherwise is our greatest resource [...].”

Daniel J. Boorstin

DEMO magnetic alternative configurations design and vertical stability analysis

To improve the performances of the fusion process and protect the device components, the knowledge of position and shape of the plasma column inside the vacuum chamber represents a critical issue playing a key role in large scale fusion devices efficient and safe operation. There are several reasons for optimizing plasma shape and position, namely, to maintain adequate clearance from the chamber wall to avoid high densities of power and particle deposition, to be sufficiently close to the wall to ensure adequate passive stabilization, to achieve efficient radio frequency (RF) heating by maximizing antenna coupling, and finally, to reduce magnetohydrodynamic (MHD) activity [5.1].

In order to design an optimized plasma shape and position during the different phases of a plasma discharge¹, different tools modelling both static and dynamic behaviour of a fusion plasma are required. The same models constitute also the starting point of real-time plasma boundary reconstruction in an operating fusion device. The plasma shape is unfortunately a quantity not directly measurable; it can only be calculated using data provided by the diagnostic sensors, such as magnetic measurements of currents and fields. Therefore, whether to improve fusion performance or to protect the machine components, the problem of reconstructing the plasma boundary is critical for both diagnostic and control purposes.

¹ The so-called “plasma scenario”.

In this thesis only the first point will be tackled, since DEMO is still at the stage of conceptual design. In particular, after a brief introduction on the models dominating the plasma behaviour, the main results achieved concerning the DEMO magnetic alternative configurations (introduced in Section 4.2) optimized shape and position design together with a vertical stability analysis are illustrated.

5.1 Theoretical basis

The plasma mathematical description can be performed at different levels of abstraction. The starting point proposed here is represented by the magnetohydrodynamic (MHD) that allows an analysis under a macroscopic point of view. Since all processes involving microscopic actions are neglected, the model is sufficiently accurate when applied to appropriate temporal and spatial scales, e.g. the distances must be much larger than the Debye length.

5.1.1 Magnetohydrodynamic model (MHD)

Plasma is globally electrically neutral. However, since at least two species of charged particles (a kind totally or partially ionized, and an equivalent number of electrons) compose a plasma, its dynamic behaviour is different from that of a neutral gas. In a fusion plasma the two forces acting on particles are short-range interactions due to collisions, which are predominantly elastic Coulomb collisions and long-range Lorentz forces originating from macroscopic \mathbf{E} and \mathbf{B} fields, which requires a coupling of the Boltzmann equations to Maxwell's equations. The full set of equations then provides a very detailed description of the plasma behaviour ranging from the orbits of individual particles to the macroscopic behaviour of fusion experiments. However, the broadness of information is coupled with the complexity, which makes even a numerical solution practically impossible. Therefore, a simpler model, like the magnetohydrodynamic (MHD), which leads to a reduction of the dimensionality of the problem or in other words to a single fluid description of the plasma is necessary.

The MHD model describes the time evolution of electrically conducting fluids, i.e. plasmas. The fundamental concept behind MHD is that magnetic fields can induce currents in a moving conductive fluid, which in turn polarizes the fluid and reciprocally changes the magnetic field itself. It substantially simplifies the description of a plasma by two important assumptions. In the first assumption, the low-frequency approximation, the displacement current and net charges are neglected in Maxwell's equations. Displacement currents can be neglected if the phase velocity of the electro-magnetic wave of interest, as well as the ion

and electron thermal velocities are much slower than the speed of light $\frac{\omega}{k}$, v_{Ti} , $v_{Te} \ll \frac{1}{\sqrt{\epsilon\mu}}$. Net charges can be neglected if the characteristic frequencies are much lower than the electron plasma frequency and if the characteristic lengths are much longer than the Debye length, $\lambda \gg \lambda_D$. Neglecting net charges implies the quasi-neutrality of the plasma:

$$n_e = n_i = n$$

where it has been assumed that ions are singly charged, $Z_i = 1$.

The *Maxwell's equations* of electromagnetism in their quasi-stationary form are:

$$\nabla \times \mathbf{E} = -\frac{\partial \mathbf{B}}{\partial t} \quad (5.1)$$

$$\nabla \times \mathbf{H} = \mathbf{J} \quad (5.2)$$

$$\nabla \cdot \mathbf{B} = 0 \quad (5.3)$$

where \mathbf{E} is the electric field, \mathbf{B} the magnetic flux density, \mathbf{J} the current density and \mathbf{H} the magnetic field. The (5.1) equation is also known as Faraday's law whereas the (5.2) is the low-frequency Ampere's law, in which the displacement current $\frac{\partial}{\partial t}(\epsilon\mathbf{E})$ is neglected. The (5.3) equation represents the magnetic divergence constraint.

The two following constitutive laws must be coupled with the previous equations:

$$\mathbf{B} = \mu\mathbf{H} \quad (5.4)$$

$$\mathbf{E} + \mathbf{v} \times \mathbf{B} + \mathbf{E}_{ext} = \underline{\underline{\eta\mathbf{J}}} \quad (5.5)$$

Eq. (5.4) is the magnetic constitutive relation, linear in vacuum and in linear media such as air and plasma where $\mu = \mu_0$, nonlinear in ferromagnetic media where μ is a function of \mathbf{B} .

Eq. (5.5) is the electric constitutive relation, mainly the generalized Ohm's law where the speed \mathbf{v} can be assumed zero in the conductors but non-zero within the plasma, and \mathbf{E}_{ext} is the external electric field. As a second assumption the electron mass is neglected. As with the first assumption this requires that the frequencies of interest are small compared to the response of the electrons. The single fluid MHD description of a plasma is now obtained by introducing fluid variables, such as the mass density ρ , fluid velocity \mathbf{v} , and current density \mathbf{J} , and combining the equations for electrons and ions, assuming $m_e \ll m_i$,

$$\rho = m_i n_i + m_e n_e \approx m_i n_i$$

$$\mathbf{v} = \frac{1}{\rho} (m_i n_i \mathbf{v}_i + m_e n_e \mathbf{v}_e) \approx \mathbf{v}_i$$

$$\mathbf{J} = en(\mathbf{v}_i - \mathbf{v}_e) \approx en(\mathbf{v} - \mathbf{v}_e)$$

The total pressure p , and temperature T , are obtained by summing over the species.

To completely define the model, the following three equations of thermo-fluid dynamics within the plasma have to be added to previous equations:

$$\frac{\partial \rho}{\partial t} + \nabla \cdot (\rho \mathbf{v}) = 0 \quad (5.6)$$

$$\rho \left(\frac{\partial \mathbf{v}}{\partial t} + \mathbf{v} \cdot \nabla \mathbf{v} \right) = -\nabla p + \mathbf{J} \times \mathbf{B} \quad (5.7)$$

$$\frac{\partial}{\partial t} (\rho^{-\gamma} p) + \mathbf{v} \cdot \nabla (\rho^{-\gamma} p) = 0 \quad (5.8)$$

Where γ is the specific heat ratio.

Eq. (5.6) is the mass continuity equation stating that the mass variation within plasma volume is due only to mass flow through the surfaces of control volume; therefore, phenomena as ionization and recombination do not play any role. Developing the divergence of the product, the terms $\mathbf{v} \cdot \nabla p$ and $\rho \nabla \cdot \mathbf{v}$ represent respectively the effects of expansion and convection.

Eq. (5.7) expresses the momentum conservation which states that the variation of the plasma momentum density is due to the overall force density, i.e. the sum of the electromagnetic force density ($\mathbf{J} \times \mathbf{B}$) and the one due to the pressure ($-\nabla p$), acting on it. This equation represents the acceleration of the fluid as response to the local forces acting on it. Eq. (5.8) is an adiabatic law, with no heat exchanges, assuming that the processes take place rapidly, with entropy conservation. In Eq. (5.6) the mass defect (or rather the transformation of mass into energy) that takes place in nuclear reactions is neglected².

5.1.2 Ideal MHD

The ideal MHD model is obtained simply by assuming $\underline{\eta} = 0$, i.e. considering the *plasma* as a *perfect electrical conductor*. Thus, in the local frame of the moving fluid no electric field can be sustained, and consequently Eq. (5.5) turns into:

$$\mathbf{E} + \mathbf{v} \times \mathbf{B} = 0$$

In this case, the MHD model requires that magnetic field lines are frozen into the plasma and have to move along with it: this result is also known as *Alfvén's Theorem*.

Unfortunately, an analysis of the various assumptions made in the derivation of the ideal MHD equations shows that not all assumptions are valid for plasmas of fusion interest. In particular, the assumed high collisionality is not satisfied. However, as the incorrectly treated parts, namely the transport of parallel momentum and energy, are of little importance in equilibrium and stability calculations, the ideal MHD model has proven to provide an accurate description of macroscopic plasma behaviour.

² Referring to the Einstein's theory of relativity, $\Delta E = \Delta M \cdot c^2$ and recalling that the energy produced by D-T fusion is $\Delta E = 17.6 \text{ MeV}$, the defect of the final mass with respect to the initial one will be $\Delta M \cong \frac{3}{1000}$, which makes negligible the mass defect.

5.1.3 The equilibrium problem

The time independent form of the ideal MHD equations ($\frac{\partial}{\partial t} = 0$) can be used to calculate the so-called *MHD Equilibrium*. According to Equation (5.7) a static equilibrium, where the velocities are also set to zero ($v = 0$), requires:

$$\begin{cases} \nabla p = \mathbf{J} \times \mathbf{B} \\ \nabla \cdot \mathbf{B} = 0 \\ \nabla \times \mathbf{H} = \mathbf{J} \end{cases} \quad (5.9)$$

A simple scalar multiplication of the first equation by \mathbf{J} and \mathbf{B} respectively, being ∇p by definition of cross product perpendicular to both \mathbf{J} and \mathbf{B} vectors, yields (**Figure 5.1**):

$$\mathbf{B} \cdot \nabla p = 0 : \text{the magnetic field lines lie}$$

on the nested isobaric surfaces;

$$\mathbf{J} \cdot \nabla p = 0 : \text{current density lines lie on isobaric / magnetic surfaces.}$$

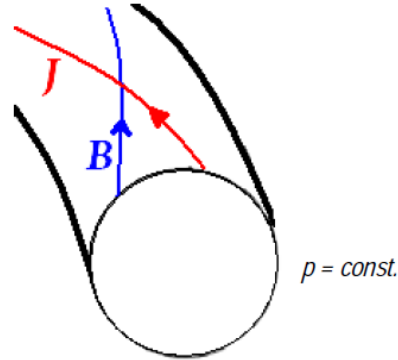


Figure 5.1: magnetic field and current density lines on an isobaric surface.

MHD equilibrium is reached whenever magnetic pressure balances the plasma kinetic pressure.

The MHD model is often used for complicated geometry systems, for which more sophisticated models cannot be applied. Despite its

simplifying assumptions, the MHD model allows very useful predictions.

5.1.4 Grad-Shafranov equation

A cylindrical reference system (**Figure 5.2**), identified by the (r, φ, z) triad, is well suited for the description of a toroidal axisymmetric equilibrium; r and z coordinates are also known as poloidal coordinates, whereas φ is called toroidal coordinate. In this system, the axisymmetry hypothesis predicts that all scalar variables of interest depend only on the poloidal coordinates:

$$\frac{\partial}{\partial \varphi} = 0$$

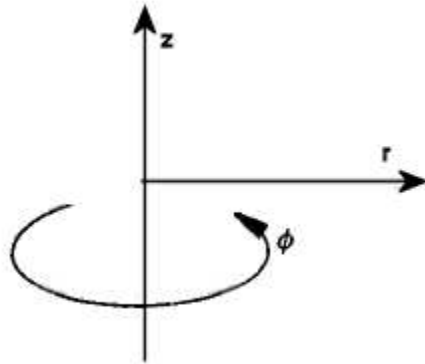


Figure 5.2: Cylindrical coordinate system.

In cylindrical coordinates, \mathbf{B} and \mathbf{J} can be expressed in terms of two scalar functions, namely, the *poloidal magnetic flux per radians* $\Psi(r, z)$ and the *poloidal current function* f respectively defined as:

$$\Psi(r, z) = \frac{\bar{\psi}}{2\pi} \quad (5.10)$$

$$f(r, z) = rB_{\phi}(r, z) = \mu \frac{I_{pol}}{2\pi} \quad (5.11)$$

Being $\bar{\psi}(r, z) = \int_0^r B_z(r', z') 2\pi r' dr'$ the poloidal magnetic flux, B_ϕ the toroidal field and I_{pol} the poloidal current. Therefore magnetic flux and current densities can be expressed as:

$$\mathbf{B} = \mathbf{B}_{pol} + \mathbf{B}_{tor} = \frac{1}{r} \nabla \Psi \times \mathbf{i}_\phi + \frac{f}{r} \mathbf{i}_\phi \quad (5.12)$$

$$\mathbf{J} = \frac{1}{r} \nabla \left(\frac{f}{\mu} \right) \times \mathbf{i}_\phi - \frac{1}{\mu_0 r} \Delta^* \Psi \cdot \mathbf{i}_\phi \quad (5.13)$$

where \mathbf{i}_ϕ is the unit vector in the toroidal direction, μ_0 is the magnetic permeability of the vacuum and the toroidal current component related to via the second order differential operator Δ^*

$$\Delta^* \Psi = r \frac{\partial}{\partial r} \left(\frac{1}{\mu_r r} \frac{\partial \Psi}{\partial r} \right) + \frac{\partial}{\partial z} \left(\frac{1}{\mu_r} \frac{\partial \Psi}{\partial z} \right) \quad (5.14)$$

μ_r being the relative magnetic permeability.

At the time scale of interest for current, position, and shape control, *because of the low plasma mass density ρ , inertial effects can be neglected.* Hence at equilibrium, the plasma momentum balance (5.7) can be rewritten as a second order nonlinear elliptic differential equation also known as the *Grad-Shafranov equation*:

$$\Delta^* \Psi = -f(\Psi) \frac{df(\Psi)}{d\Psi} - \mu_0 r^2 \frac{dp(\Psi)}{d\Psi} \quad (5.15)$$

The Grad-Shafranov equation describes the equilibrium for an isotropic³ plasma given a particular choice of p and f , which also set boundary conditions at the coordinate frame origin $r = 0$ and at infinity.

This formulation can be extended to various domains, where magnetic flux is present. To begin with, it can be observed that, according to Poisson's equation, the term $\Delta^* \Psi$ is equal to zero in the vacuum region. Moreover, $\Delta^* \Psi$ is proportional to the toroidal current density J_{ext} in the external conductors and coils. To summarize, the following PDE (Partial Differential Equation) problem has been defined:

³ Isotropic media show the same physical properties in all directions.

$$\Delta^* \Psi = \begin{cases} -f \frac{df}{d\Psi} - \mu_0 r^2 \frac{dp}{d\Psi} & \text{in plasma region} \\ -\mu_0 r J_{ext} & \text{in external conductors} \\ 0 & \text{elsewhere} \end{cases} \quad (5.16)$$

with boundary conditions:

$$\begin{cases} \Psi(0, z, t) = 0 \\ \lim_{r^2+z^2 \rightarrow \infty} \Psi(r, z, t) = 0 \end{cases} \quad (5.17)$$

The above equations are used to calculate the poloidal flux function at time t . However, the problem is ill posed, since $p(\Psi)$ and $f(\Psi)$ must be given as functions of Ψ , whose spatial dependence is not known until equation (5.16) is solved and consequently, iterative schemes have to be used. In Section 5.2.1 an overview of the methods used for the plasma boundary reconstruction is proposed.

Figure 5.3 shows the flux surfaces and profiles of J_ϕ , p , and B_ϕ obtained by numerical solution of the equation for a typical case.

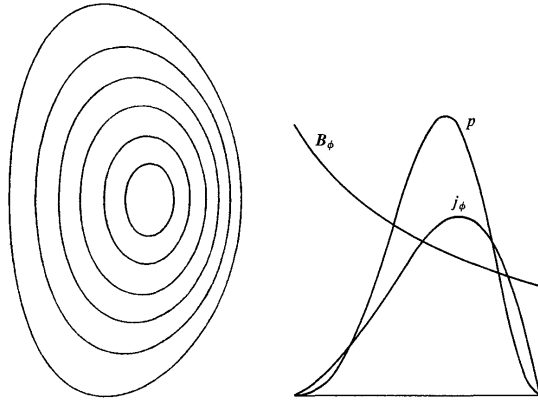


Figure 5.3: Equilibrium (nested) flux surfaces and plots of toroidal current density, plasma pressure, and toroidal magnetic field across the mid-plane.

The inner magnetic surface degenerates into a line defined “magnetic axis”.

5.2 The free boundary dynamic plasma equilibrium problem

A definition of the plasma boundary descending from the physics of the problem is associated with the magnetic configuration of the plasma (Chapter 1): the boundary is the outermost closed flux surface entirely contained inside the vacuum vessel (**Figure 5.4**). Particles interior to the plasma boundary follow magnetic field lines that remain in the plasma interior, while field lines external to the boundary intersect with structures. Topologically, the boundary is either the outermost flux contour not intersecting any solid object or it is a separatrix, that is, a surface containing an X point (**Figure 5.4**), which is a point at which the poloidal magnetic field is zero.

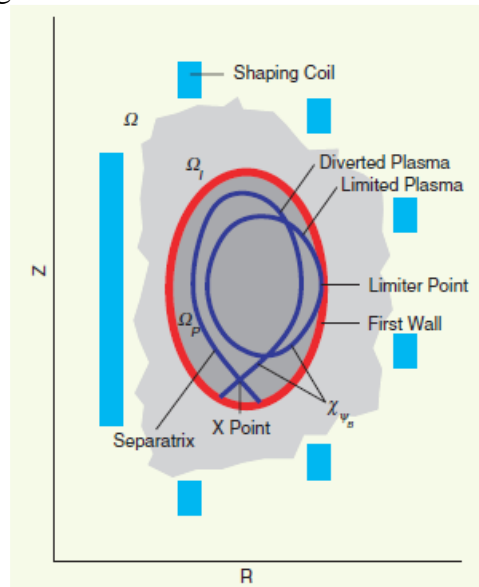


Figure 5.4: Poloidal cross section of a tokamak machine. [5.1]

For an axisymmetric plasma the analysis can be limited to a poloidal cross section of the machine. Two domains of interest can be identified on the poloidal plane Ω , as shown in **Figure 5.4**:

- Ω_l is the region enclosed by the shaping coil locations;
- the subset Ω_p of Ω_l is the plasma region, defined as the vacuum region interior to the containment vessel, where plasma may exist.

The *boundary reconstruction problem* is to locate the plasma inside the vacuum vessel and determine the plasma boundary position with respect to the first-wall components. Clearly, *the equilibrium problem and the boundary reconstruction problem are intimately connected*. It is important to stress that the plasma is seen and investigated only through the eyes of a privileged magnetic descriptor, namely the flux function, which contains all of the information needed for reconstructing the boundary position.

Once the equilibrium problem and the boundary definition have been formulated, the focus of attention is on understanding how the plasma and boundary shape evolve in time, as well as the possible magnetic configurations. A complete answer to these questions lies in the solution of a free boundary problem, since the differential equation governing the equilibrium (5.16) is defined in a domain whose boundary is not given a priori and is part of the unknown. The free boundary problem is often solved using finite difference or finite element techniques, whose implementation sometimes involves adaptive meshing procedures to follow the plasma deformation.

In Section 5.2.1 an overview of plasma equilibrium simulation codes developed during the years is given whereas Section 5.2.2 describes in detail the CREATE-NL+ tool used for static and dynamic analysis of the DEMO plasma configurations.

5.2.1 An overview of plasma equilibrium simulation codes

During the last decades, many electromagnetic equilibrium codes solving the plasma dynamic free boundary equilibrium (PDFBE) problem have been developed by different research teams. The resulting non-linear equilibrium codes allow the plasma shape reconstruction and the simulation of the plasma dynamics during a plasma discharge.

It is convenient to distinguish the PDFBE solvers among:

- equilibrium evolution codes (PROTEUS [5.2] and MAXFEA [5.3]);
- equilibrium reconstruction codes (EFIT [5.4]);
- boundary reconstruction codes (XLOC [5.5], filament method [5.6]).

The *equilibrium evolution codes* “evolve” the equilibrium, based on the dynamics of the external coil currents and either a bulk or distributed plasma current, while *equilibrium reconstruction codes* solve the equilibrium problem, taking into consideration internal measurements and the actual plasma current distribution. Both types of codes provide a complete magnetic description of the plasma, which includes both the plasma current density distribution and the flux distribution. A primary difference between the two classes of codes concerns the input data, since equilibrium reconstruction codes use experimental measurements and the resulting accuracy is limited because of ill-posedness of the problem and measurement noise; these tools are used in the experimental devices and are fundamental for the real-time applications, as the plasma feedback control. On the other hand, the data for the equilibrium evolution codes are provided by the code itself, in the form of simulated currents in all conductors, including plasma, and is therefore perfectly known, at least in principle. Finally, *boundary reconstruction codes* are limited to locating the boundary and do not aim at a detailed analysis of the internal plasma features.

The EFIT (Equilibrium FITting) code [5.7] is an equilibrium reconstruction algorithm that fits the equilibrium model (5.16) to the external magnetic measurements and to internal diagnostic data. The solution, which satisfies the Grad-Shafranov model, accounts for a distributed current source in the plasma region and is given by the pair (Ψ, J_φ) , where the distribution Ψ of flux on the poloidal plane along with the toroidal plasma current J_φ provide the least-squares fit to the data consistent with (5.15).

The XLOC code [5.5] represents the magnetic flux ψ on the poloidal plane with several polynomial functions of high degree, each locally defined over connected domains surrounding the plasma. The magnetic flux function is then extrapolated into the vacuum region (external to the plasma boundary) by fitting the available sensor measurements to the vacuum equation $\Delta^*\Psi = 0$, thus overcoming the plasma modelling. The information is then post-processed by a second module that reconstructs the plasma shape in terms of boundary to first-wall distances called “*gaps*”.

The filament method develops semi-analytical procedures to approximate the plasma flux distribution with a suitable number of current filaments placed inside the vacuum vessel.

5.2.2 CREATE-NL+ code

CREATE-NL+ code [5.8], implemented in MATLAB[®] environment, is a FEM code simulating the time evolution of 2D axisymmetric plasmas in toroidal nuclear fusion devices in the presence of current and/or voltage driven active circuits, currents induced in the passive conductors, and iron components. Although never systematically presented to the scientific community, the first version of CREATE-NL code was developed in 2002 with the objective of simulating JET plasmas in order to design and test innovative multivariable controllers like the XSC [5.9]. It was used for several activities including vertical stabilization studies on JET and ITER, shape controllability analyses on ITER, EAST, MAST, ASDEX-U, TCV, FTU, preliminary studies on FAST and DEMO. The code requires as inputs a set of machine configuration data (geometry, active coils and passive structures configuration, first wall definition, etc.); a set of input signals. PF coils voltages can be then generated by a feedback control law, whereas plasma related quantities can be generated by a detailed transport simulation code including heating and current drive systems (**Figure 5.5**). The CREATE-NL numerical solver was formulated to deal with a different number of equations and variables since the core solver is based on a pseudo-inverse procedure. In fact CREATE-NL was used also to solve shape and profile identification problems.

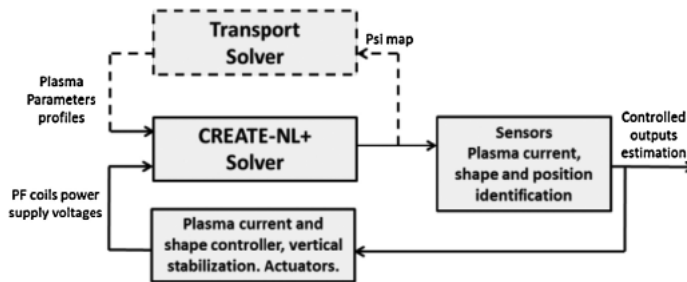


Figure 5.5: The CREATE-NL+ solver in interaction with a feedback control block, a transport equation solver and a plasma shape, position and current identification block. [5.8]

From a numerical point of view, the increased robustness of CREATE-NL+ is guaranteed by a robust numerical procedure for the plasma boundary search, and by a reliable numerical solution of the nonlinear algebraic equations arising from the FEM formulation.

Starting from the PDE problem already defined:

$$\Delta^* \Psi = \begin{cases} -f \frac{df}{d\Psi} - \mu_0 r^2 \frac{dp}{d\Psi} & \text{in plasma region} \\ -\mu_0 r J_{ext} & \text{in external conductors} \\ 0 & \text{elsewhere} \end{cases} \quad (5.16)$$

with initial and boundary conditions:

$$\begin{cases} \Psi(r, z, t) = \Psi_0(r, z) \\ \Psi(0, z, t) = 0 \\ \lim_{r^2+z^2 \rightarrow \infty} \Psi(r, z, t) = 0 \end{cases} \quad (5.17)$$

The above equations are used to calculate the poloidal flux function at time t provided that the plasma boundary can be determined, the toroidal current density in the PF coils is known, and the functions $p(\Psi)$ and $f(\Psi)$ are assigned within the plasma. Under simplifying assumptions, functions $p(\Psi)$ and $f(\Psi)$ can be expressed in terms of few plasma parameters, for example poloidal beta β_p and internal inductance l_i . As for J_{ext} , this can be expressed as a linear combination of the circuit currents. Therefore, the magnetic flux and the plasma configuration can be determined when prescribing the vector of currents \mathbf{I} (including poloidal field coils and plasma currents) along with functions $p(\Psi)$ and $f(\Psi)$. The time evolution of these currents is given by a circuit equation.

$$\dot{\Psi} + \mathbf{R}\mathbf{I} = \mathbf{V} \quad (5.18)$$

where $\dot{\Psi}$ is the vector of magnetic fluxes linked with the circuits, \mathbf{R} is the resistance matrix, and \mathbf{V} is the vector of applied voltages. The flux vector is defined as the integral of the flux function over the conductor regions (see (7) for the relationship among continuous variables).

The relationship between the toroidal current density in the control circuits and the poloidal flux can be obtained from Faraday's and Ohm's laws. In principle, the active powered coils and the passive conductors can be treated in the same way. The only difference is in the

applied voltage, which is zero in the passive conductors. It can be shown that

$$J_{ext} = -\frac{\sigma}{r} \frac{\partial}{\partial t} \Psi + \frac{\sigma}{2\pi r} u \quad (5.19)$$

where u is the voltage applied to the coil. Eq. (5.19) must then be integrated over the conductor regions.

In order to recast the PDE equilibrium problem to a finite dimensional problem a first order FEM is adopted. Plasma current density can be assigned in terms of $p(\Psi)$ and $f(\Psi)$ functions or described by means of a finite number of parameters using the following relationships:

$$J_{pl}(r, \Psi) = r \sum_{k=1}^{M_a} a_k \chi_{ak}(\bar{\Psi}, \alpha) + \frac{1}{r} \sum_{k=1}^{M_b} b_k \chi_{bk}(\bar{\Psi}, \alpha) \quad (5.20)$$

Where χ are basis functions of the normalized flux, defined as

$$\bar{\psi} = \frac{\psi - \psi_{axis}}{\psi_{boundary} - \psi_{axis}}$$

and of a parameter vector α . In this case additional equations are needed to close the problem, e.g. β_p , l_i and I_p fixed to a prescribed value.

FEM approach finally requires the solution of a nonlinear set of equations in the form:

$$\mathbf{F}(\boldsymbol{\Psi}, \boldsymbol{\pi}) = \mathbf{F}(\mathbf{x}_1, \mathbf{x}_2) = 0 \quad (5.21)$$

in the n_1 unknowns \mathbf{x}_1 , which is the vector of fluxes in the spatial discretization nodes, and n_2 unknowns $\boldsymbol{\pi} = (\mathbf{I}^T \boldsymbol{\alpha}^T)^T$, which is a vector of variables including coil currents and profile parameters. It is worth to notice that currents become unknowns if circuits are voltage driven. Problem (5.21) is solved with an iterative Newton based method where boundary conditions in (5.17) are treated via a suitable coupling with boundary integral equations [5.10]. The calculation and inversion of the \mathbf{F} Jacobian matrix is the core of the solver. The candidate solution update in the iterative algorithm is:

$$\mathbf{x}^{k+1} = \mathbf{x}^k - \left(\frac{\partial \mathbf{F}(\mathbf{x}^k)}{\partial \mathbf{x}} \right)^{-1} \mathbf{F}(\mathbf{x}^k)$$

Where $\mathbf{x}(\Psi^T \boldsymbol{\pi}^T)^T$, and k denotes the iteration step.

The calculation and inversion of the Jacobian matrix plays an important role both for the computational time and the numerical stability. It was in fact observed that, in the presence of plasma related profiles provided in a numerical form, discontinuities and jumps due to FEM approximation, the calculation of the Jacobian matrix adopted in CREATE-NL determined a fragility of the solver. An ad hoc solution was found for a fast numerical Jacobian calculation which is one of the most important improvements implemented in CREATE-NL+ (for more details see [5.8]).

5.3 DEMO alternative magnetic configurations design

The design of DEMO standard and alternative magnetic configurations follows an almost standard procedure.

The requirements of reference equilibria are deduced by the “PROCESS” runs performed by the PPPT EUROfusion Group. PROCESS is a Systems Code for Fusion Power Plants [5.11]: it assesses the engineering and economic viability of a hypothetical fusion power station using simple models of all parts of a reactor system, from the basic plasma physics to the generation of electricity. PROCESS is used to identify DEMO main machine and plasma parameters. The PPPT EUROfusion Group in Garching (Germany) consists of several physicists and engineers who work jointly on different DEMO tasks. The interaction with the PPPT group is fundamental during the design phase since several engineering issues, e.g. the remote maintenance, have to be taken into account. Finally, DEMO reference geometries are produced by CCFE providing realistic design of the structures, e.g. vessel, and Toroidal Field (TF) coils (**Figure 5.6**).

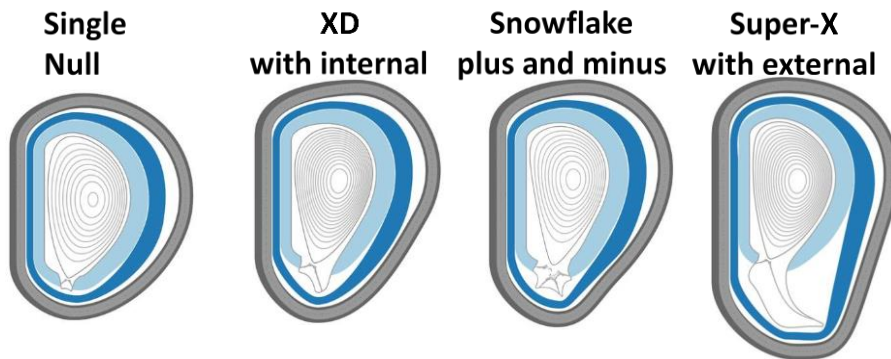


Figure 5.6: from the left, DEMO a) Single-Null, b) X Divertor, c) Snowflake, d) Super-X Divertor, geometries. [5.12]

Once the geometry and the main machine and plasma parameters have been produced and identified, the plasma configuration design mainly consists in the definition and optimization of a Poloidal Field (PF) coil system able to produce the desired plasma configuration satisfying the design constraints. Section 5.3.1 lists the design constraints whereas Section 5.3.2 illustrates the PF coil system optimization procedure. Finally, Section 5.3.3 shows few examples of optimized standard and alternative magnetic configurations.

5.3.1 PF coil system design constraints

Once the optimized geometry has been produced for the different plasma configurations, a feasible set of PF coils has to fulfil the following list of constraints concerning PF coil current, magnetic field and forces on the coils.

- I. The poloidal coils cross-sections shall be determined assuming a current density limit of 12.5 MA/m^2 .
- II. The maximum field at the location of the PF and CS coils shall not exceed 12.5 T .
- III. The maximum vertical force on the central solenoid stack shall not exceed 300 MN .

- IV. The maximum separation force in the central solenoid stack shall not exceed 350 MN.
- V. The maximum vertical force on a single PF coil shall be 450 MN.
- VI. In the case of two or more PF coils positioned close to each other: over a poloidal length of 3 m the maximum total vertical force transferred to the TF coils shall be < 450 MN.

Therefore, among all the possible PF coil system configurations only the ones satisfying the constraints listed above can be taken into account.

5.3.2 PF coil system optimization procedure

The first step in the optimization procedure is the production of a 2D mesh in MATLAB[®] environment, according to the geometry defined for example in **Figure 5.6**.

A non-optimized set of Central Solenoid (CS) and Poloidal Field (PF) coils is then defined in order to evaluate the pre-magnetization phase⁴. **Figure 5.7** shows an example of pre-magnetization phase for a DEMO Single-Null configuration after the definition of a CS stack composed by 5 elements and a 6 PF coils system. The position and width of the CS stack is mainly related to the maximum current density J_{max} of the coils and vertical magnetic field B_{max} on the z-axis of the torus; both J_{max} and B_{max} have to satisfy the constraints listed in Section 5.3.1. The pre-magnetization flux in the centre of the vacuum vessel can be therefore evaluated.

⁴ Even if the PF coils position and dimension is still not optimized, they will have a marginal effect on the pre-magnetization flux.

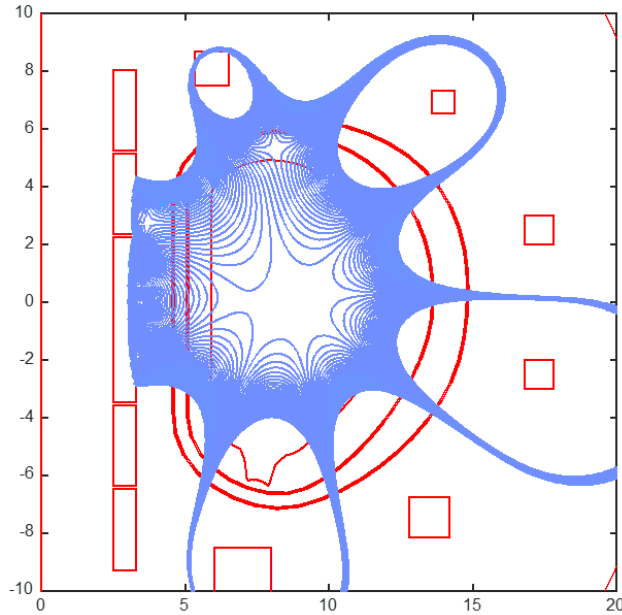


Figure 5.7: Example of pre-magnetization phase for a DEMO Single-Null configuration.

Starting from the pre-magnetization flux, the boundary flux at Start of Flat-Top (SOF) can be computed via Ejima scaling [5.13]. In order to define an optimized set of PF coils able to increase the flux swing at flat top satisfying all the currents and vertical forces constraints, a redundant set of PF coils is produced. **Figure 5.8** shows a redundant set of 30 PF coils produced for the SN plasma configuration in **Figure 5.7**.

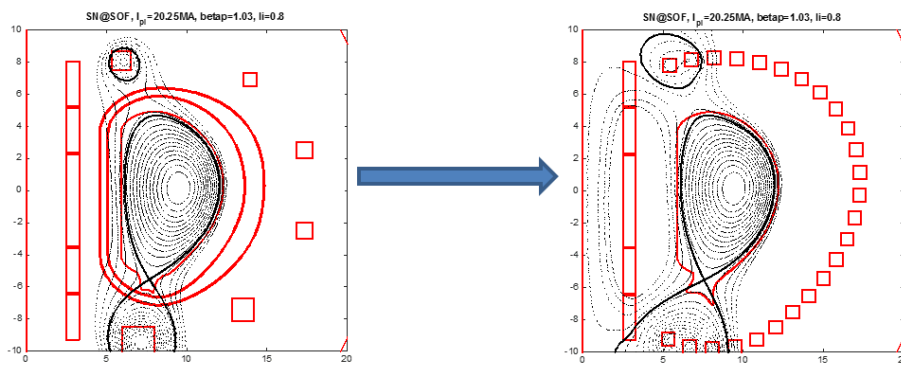


Figure 5.8: Redundant PF coil system for the SN flat-top configuration. [5.12]

The PF coil optimization procedure can be briefly formalized as follows:

- A redundant set of PF coils compatible with the available space - limited by the outer TF shell - is defined (**Figure 5.8**). All the coils have the same dimension. In the optimization problem, the current density constraint is relaxed since in post-processing the dimension of the selected coils can be modified in order to verify the constraint of 12.5 MA/m^2 .
- Chosen the number N constituting the PF coil set (e.g. 6 PF coils), all the possible combinations of N PF coils have to be investigated; a criterion to identify the possible PF coils combinations could be the minimum distance between two adjacent coils mass centre.
- Once few sets of PF coils have been identified to satisfy the constraints, an exhaustive analysis of the candidate PF coil systems is carried out in order to find SOF and EOF configurations able to maximize the flat-top flux swing while maintaining the desired plasma shape within a certain tolerance (always verifying all field and vertical force constraints summarized in Section 2.2.)

Cases of candidate PF coil systems composed by a different number of coils can be implemented. If no main differences in terms of flux swing can be noted in the different solutions, the system with a higher number of coils is preferable in order to increase the controllability degrees of freedom on the configuration and to reduce the maximum voltage request on the PF coils.

The implementation of the optimization procedure have to take into account the presence of the ports. Typically, in a DEMO standard configuration, there are 3 ports: upper, equatorial and lower ports for maintenance and diagnostics. The ports position and dimensions are given by the PPPT Remote Maintenance Group.

An example of identified candidate PF coil system through the optimization procedure proposed is shown in **Figure 5.9** (in blue the selected PF coils whereas the ports are highlighted in light blue).

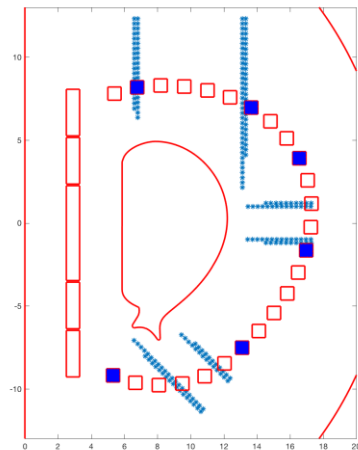


Figure 5.9: Selected coils satisfying the ports constraint. [5.12]

The set of PF coil currents produced by the optimization problem at SOF and EOF is used to finalise the dimension of the coils taking into account the current density constraint (relaxed in the first optimization phase). Moreover, a slight modification of the PF coil positions could be necessary to ensure a minimum distance from the TF coil outer shell and to avoid the intersection with the ports. **Figure 5.10** shows the equilibria at SOF and EOF evaluated with the CREATE-NL+ equilibrium code [5.8] after a further optimization of the PF coil currents for the same case proposed in **Figure 5.7**.

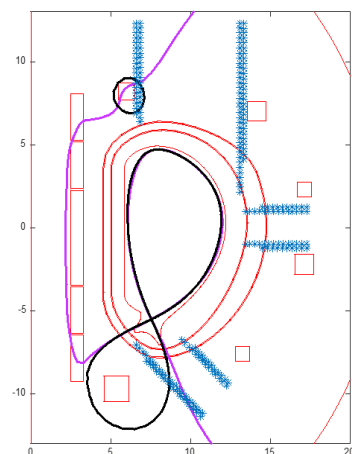


Figure 5.10: SOF and EOF DEMO Single Null optimized configurations. [5.12]

The PF coil system optimization procedure just illustrated, for the sake of simplicity in a DEMO Single-Null configuration, has been developed and used also on alternative magnetic configurations not only in DEMO, but also in EAST, DTT and other fusion devices. Section 5.3.3 reports few examples.

5.3.3 Examples

Figure 5.11-Figure 5.14 show examples of optimized alternative magnetic configurations produced for the DEMO reactor through the procedure described in Section 5.3. In particular:

- **Figure 5.11** shows the Double Null configuration;
- **Figure 5.12** shows the Snowflake configuration;
- **Figure 5.13** shows the X Divertor configuration;
- **Figure 5.14** shows the Super-X Divertor configuration.

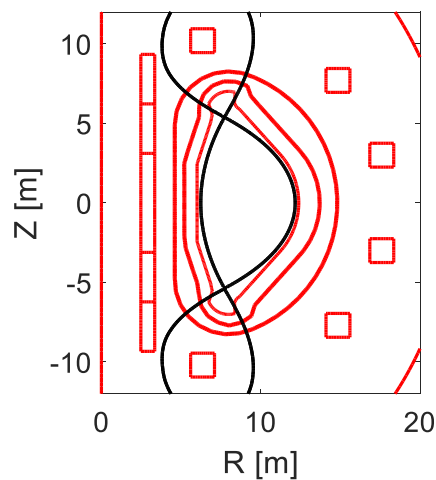


Figure 5.11: DEMO DN optimized configuration

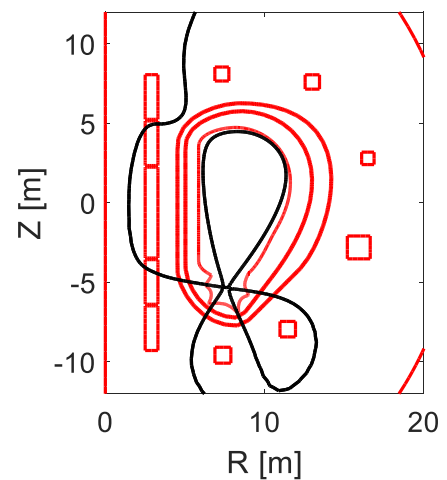


Figure 5.12: DEMO SF optimized configuration

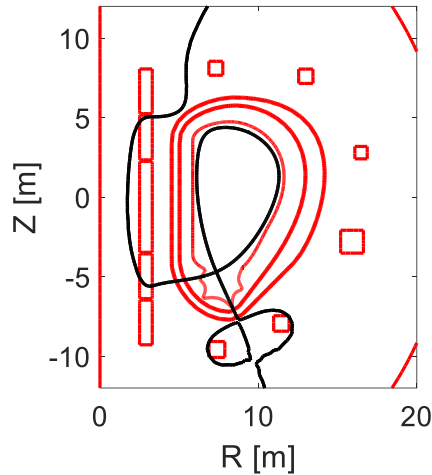


Figure 5.13: DEMO XD optimized configuration

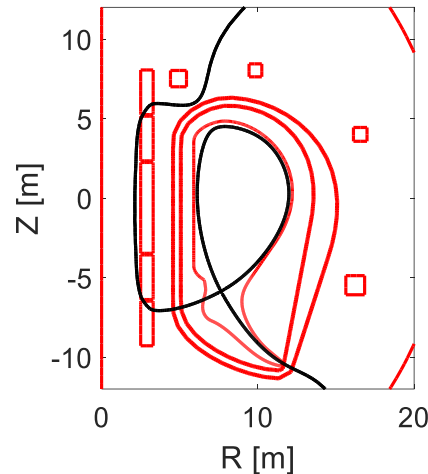


Figure 5.14: DEMO SXD optimized configuration

5.4 DEMO alternative configurations Vertical Stability (VS) analysis

Tokamak plasmas with elongated cross-sections show an inherent axisymmetric vertical instability [5.14]. This means that without corrective actions, any perturbation displacing the plasma's axisymmetric vertical position from an equilibrium position would grow exponentially, leading to a so-called vertical displacement event (VDE). Without any conductive wall, this instability would take place on the very fast Alfvén time scale (typically microseconds); conversely, plasma perturbations may induce eddy currents in the surrounding conducting structures, which tend to counteract the instability itself. This stabilizing effect lasts until the eddy currents decay due to non-vanishing resistivity, thus intuitively explaining why such instabilities can be slowed down to electromagnetic timescales (typically milliseconds) [5.14]. Thanks to this effect, a suitable magnetic active feedback controller acting on poloidal field (PF) coils may be designed, that can stabilize the vertical position. The vertical stabilization system is hence a key feature of any elongated tokamak device, either existing

[5.15] or under design [5.16]. The design of such a feedback controller and its performances depend on the growth rate of the vertical instability, among other parameters. Hence, it is crucial to correctly estimate such quantities, which critically depend on a correct description of the conducting structures [5.17].

In this Section, a Vertical Stability analysis is performed on the two Single-Null and Double-Null DEMO baseline configurations in order to assess the differences in the controllability of standard and alternative magnetic configurations. Once the reference equilibria will be illustrated, it is also shown how is it possible to obtain a set of perturbed equilibria constituting the starting point for the DEMO first wall design.

5.4.1 DEMO Single-Null (SN) and Double-Null (DN) reference equilibria definition

The requirements of DEMO reference equilibria are imposed by the “PROCESS” run and PPPT EUROfusion Group, as already illustrated in Section 5.3. The main parameters for plasma and PF coil system descending from the described interaction are the following for SN and DN configurations.

I. The considered plasma current profile parameters are:

SN	DN
Plasma current $I_{pl} = 19.6$ MA	Plasma current $I_{pl} = 18.75$ MA
poloidal beta $\beta_p = 1.107$	poloidal beta $\beta_p = 1.303$
internal inductance $l_i = 0.8$	internal inductance $l_i = 0.8$

II. Targets imposed for the flat-top plasma shape concern plasma elongation, triangularity and volume, namely

SN	DN
$k_{95} \cong 1.59$	$k_{95} \cong 1.70$
$\delta_{95} \cong 0.33$	$\delta_{95} \cong 0.40$
$V_{pl} \cong 2502$ m ³	$V_{pl} \cong 2108$ m ³

- III. The distance between the strike point legs of the SOF and EOF configurations shall not exceed 50 mm.
- IV. The coil system must be capable of having a pre-magnetization state with as large as possible poloidal magnetic flux.

In addition, also the constraints listed in Section 5.3.1 have been taken into account.

Single-Null (SN) DEMO geometry and PF coil system [5.18] used in this study are shown in **Figure 5.15** (SN DEMO baseline 2016). **Table 5-I** reports the active coils geometry, which are supposed to have zero resistance (superconductors).

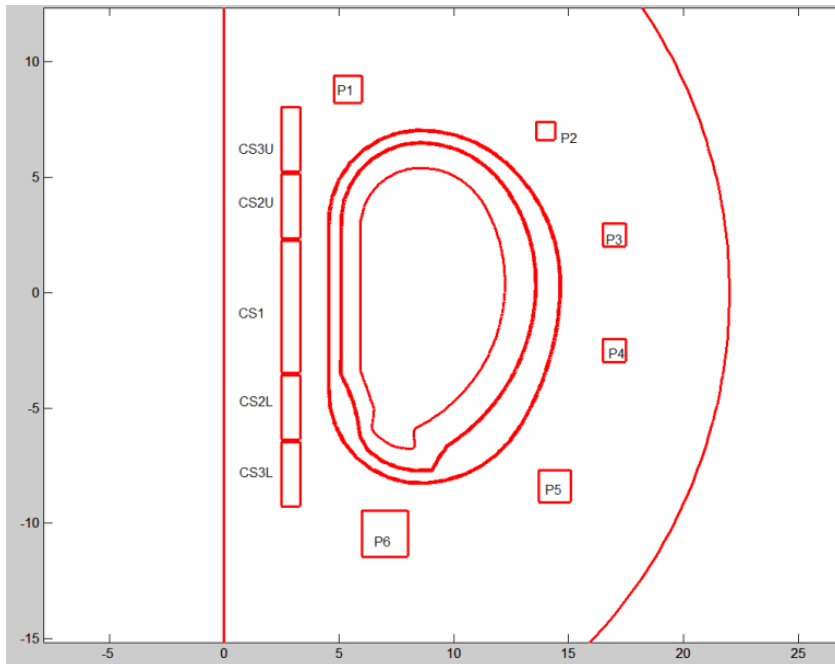


Figure 5.15: DEMO AR = 3.1 SN configuration.

Table 5-I: Coils description for SN configuration.

	R [m]	Z [m]	DR [m]	DZ [m]	Area [m ²]	Turns
CS3U	2.9000	6.6574	0.8000	2.8072	2.2458	630
CS2U	2.9000	3.7503	0.8000	2.8072	2.2458	630
CS1	2.9000	-0.6105	0.8000	5.7143	4.5714	1260
CS2L	2.9000	-4.9713	0.8000	2.8072	2.2458	630
CS3L	2.9000	-7.8784	0.8000	2.8072	2.2458	630
P1	5.4000	8.8200	1.2000	1.2000	1.4400	400
P2	14.0000	7.0000	0.8000	0.8000	0.6400	200
P3	17.0000	2.5000	1.0000	1.0000	1.0000	280
P4	17.0000	-2.5000	1.0000	1.0000	1.0000	280
P5	14.4000	-8.4000	1.4000	1.4000	1.9600	545
P6	7.0000	-10.4500	2.0000	2.0000	4.0000	1100

Double-Null (DN) DEMO geometry and the corresponding PF coil system are illustrated in **Figure 5.16**.

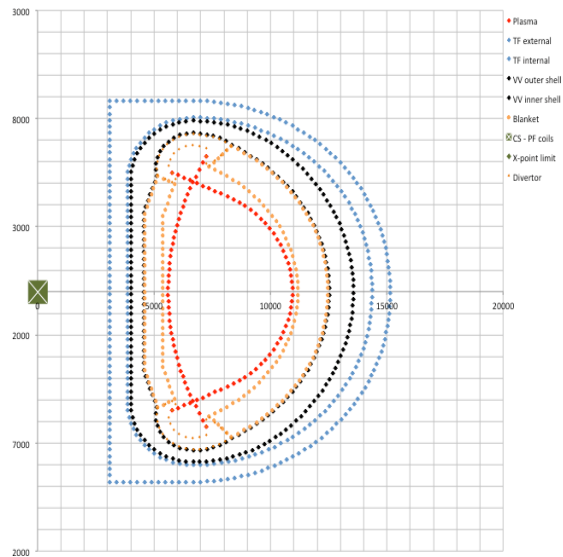


Figure 5.16: 2016 two-dimensional DEMO#01 geometry for double null configurations. The blue dots indicate the inner and outer TF walls, the black dots indicate the vessel inner and outer shell and the upper, equatorial and lower ports, the orange dots indicate the blanket, the red dots are a sketch of the reference plasma boundary

The coil system geometry assumed for this study is up-down symmetric, as shown in **Figure 5.17** and described in **Table 5-II**.

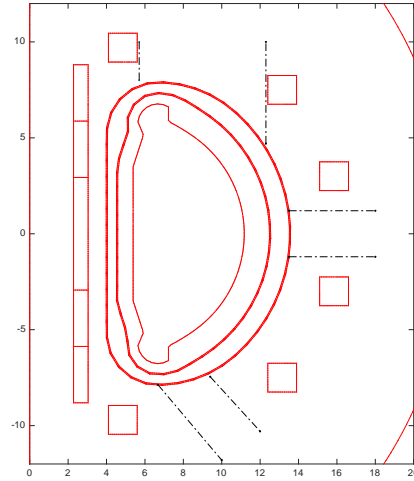


Figure 5.17: Demo#01 new coil systems configuration.

Table 5-II: Coils system geometry adopted for this study

	R [m]	Z [m]	DR [m]	DZ [m]	AR [m²]
CS3U	2.66	7.34	0.76	2.94	2.23
CS2U	2.66	4.41	0.76	2.94	2.23
CS1	2.66	0.00	0.76	5.87	4.46
CS2L	2.66	-4.41	0.76	2.94	2.23
CS3L	2.66	-7.34	0.76	2.94	2.23
P1	4.85	9.70	1.50	1.50	2.25
P2	13.15	7.50	1.50	1.50	2.25
P3	15.85	3.00	1.50	1.50	2.25
P4	15.85	-3.00	1.50	1.50	2.25
P5	13.15	-7.50	1.50	1.50	2.25
P6	4.85	-9.70	1.50	1.50	2.25

The number (eleven) and position of the coils have been scaled starting from the PF coils system proposed by PPPT group for a double null configuration and taking into account constraints related to the ports location, which are important elements for remote maintenance but at the same time have to be accurately taken into account during the

stability analyses. No optimization of the coil positions and dimensions has been performed.

In both the SN and DN DEMO geometries, the vessel is composed by two conductive shells with a thickness of 60 mm and a resistivity of $0.76 \mu\Omega m$.

Figure 5.18, **Figure 5.19** and **Table 5-III** describe the two equilibria assumed as reference equilibria for this study.

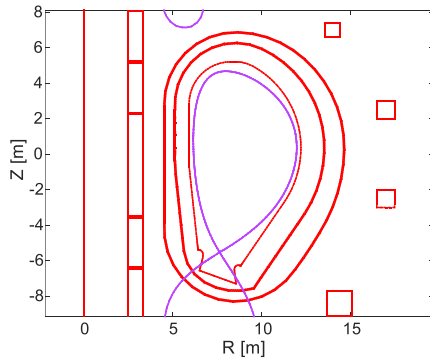


Figure 5.18: SN equilibrium
19.6 MA (Equilibrium # 1)

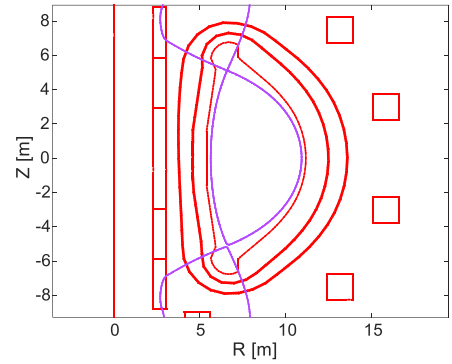


Figure 5.19: DN equilibrium
18.75 MA (Equilibrium # 2)

Table 5-III: Main equilibrium parameters for the reference SN and DN configurations

ID	Equilibrium	I_{pl}	l_i	β_{pol}	R_{pl} [m]	Z_{pl} [m]	R_{major}	a_{minor}	k	δ	Volume [m ³]
1	SN ref ($k_{95\%} = 1.59$)	19,6	0,80	1,107	9,30	0,10	9,10	2,92	1,76	0,43	2409,89
2	DN ref ($k_{95\%} = 1.70$)	18,75	0,80	1,303	8,53	0,00	8,27	2,65	1,92	0,62	1924,23

5.4.2 Single-Null perturbed plasma equilibria (development of the first wall contour)

In order to define a set of worst-case displaced equilibria for the development of an optimized first wall contour, a wide set of perturbed equilibria has been produced starting from the SN baseline configuration at the SOF. The disturbances are modelled, with respect to the reference configuration, as variations of the two main plasma parameters:

- Delta poloidal beta ($\Delta\beta_{pol}$);

- Delta internal inductance (Δl_i).

This kind of analysis gives just a first idea of the plasma movement as response to a given perturbation. The displacement of the plasma in this case is pessimistic since a perturbed equilibrium does not consider dynamical phenomena, e.g. the development of eddy currents in the passive structures which somehow counteracts the plasma movement. Different sets of equilibria have been produced keeping fixed plasma current and the currents in the external coils:

- a first set of equilibria has been produced keeping fixed one of the two plasma parameters and applying a variation to the other one (**Figure 5.20** and **Figure 5.21**);
- a second set of equilibria has been produced changing both β_{pol} and l_i .

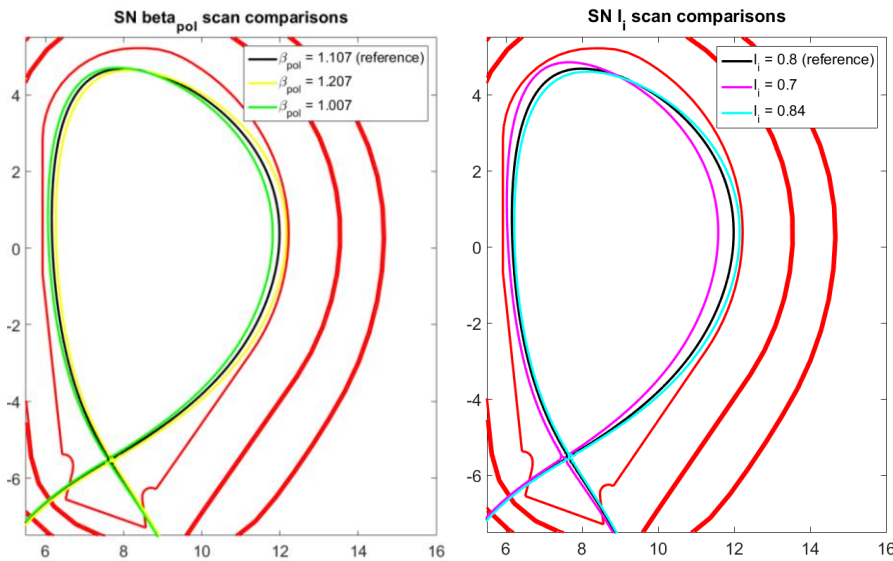


Figure 5.20: SN plasma equilibria obtained keeping fixed l_i and varying β_{pol}

Figure 5.21: SN plasma equilibria obtained keeping fixed β_{pol} and varying l_i

The main results, in terms of plasma displacement, are summarized in the following contour plots (**Figure 5.22** and **Figure 5.23**); they show the displacements corresponding to variations in the plasma parameters (β_{pol} and l_i), with respect to the reference configuration ($\Delta\beta_{pol} = 0$ and

$\Delta l_i = 0$, marked with a black circle in the parameter space, represents the reference case configuration). The light blue region represents the region of $\Delta\beta_{pol}$ and Δl_i in which the plasma hits the wall becoming “limiter”.

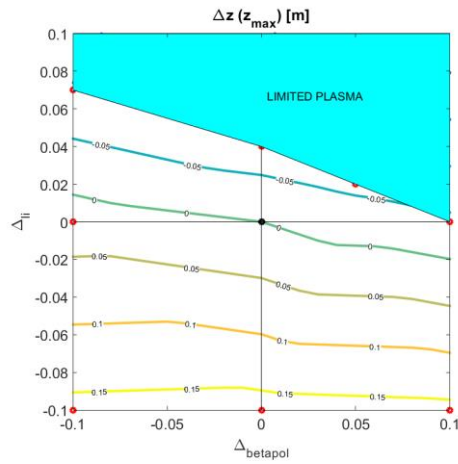


Figure 5.22: level curves for the parameter $\Delta z(z_{max})$ (z coordinate of the most external boundary point along z : $\Delta z(z_{max}) = z_{zmax}(new\ config) - z_{zmax}(reference\ config)$) in the parameter space ($\Delta\beta_{pol}$, Δl_i).

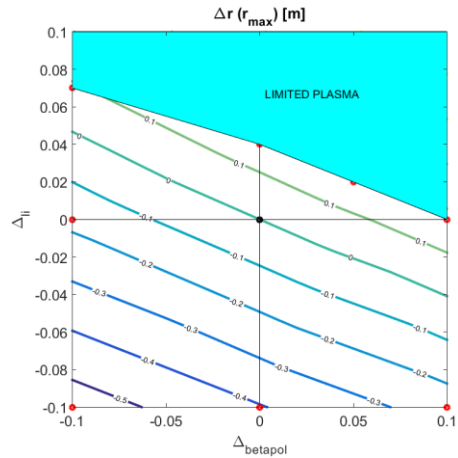


Figure 5.23: level curves for the parameter $\Delta r(r_{max})$ (r coordinate of the most external boundary point along r : $\Delta r(r_{max}) = r_{rmax}(new\ config) - r_{rmax}(reference\ config)$) in the parameter space ($\Delta\beta_{pol}$, Δl_i).

5.4.3 DEMO baseline SN and DN Vertical Stability Analysis

The pessimistic results achieved in the analysis presented in Section 5.4.2 are useful for the design of the DEMO first wall contour for different magnetic configurations. For a more realistic description of the behaviour of the plasma as response to a perturbation, dynamic phenomena have to be taken into account, e.g. eddy currents developing in the passive structures. Typically, the VS stability performances of the different plasma configurations can be assessed simulating the plasma time evolution (Section 5.2.2).

In order to assess the VS controllability of the two DEMO reference equilibria (**Table 5-III**), taking into account also the presence of the maintenance ports, the following four different cases have been considered:

Table 5-IV: Plasma configurations considered in the analysis.

ID	Short description
1	Single Null baseline configuration without ports
2	Single Null baseline configuration with ports
3	Double Null baseline configuration without ports
4	Double Null baseline configuration with ports

The presence of the ports is not negligible in the analysis of SN configuration since it reduces the effective surface of passive structures in which eddy currents can develop counteracting the plasma displacement. For the DN baseline configuration, both the cases with and without ports have been considered despite only the presence of the ports allows the plasma to move in a perturbation case, nullifying the effect of the up-down symmetry normally given by the passive structure.

Starting from reference equilibria and respective linearized models, following VS relevant parameters have been computed (see **Table 5-V**). In particular, according to the “best achievable performance” definition, the following parameters have been evaluated:

- Growth rate (γ [s^{-1}] in **Table 5-V**);
- Stability margin at psi constant (“*ms*” in **Table 5-V**);

- Voltage to stop a vertical displacement of 5 cm on the unstable mode at $t = infinity$ ($V0s$ [kV] in **Table 5-V**);
- Max Power to stop the plasma applying $2 * V0s$ voltage ($Pow2V0s$ [MW] in **Table 5-V**) and corresponding maximum vertical displacement ($Z02V0s$ [cm] in **Table 5-V**);
- Max Power to stop the plasma applying $10 * V0s$ voltage ($Pow10V0s$ [MW] in **Table 5-V**) and corresponding maximum vertical displacement ($Z0max10V0s$ [cm] in **Table 5-V**).

All the reported powers are computed without taking into account the currents in coils for Scenario which may cause a further increase of power.

Table 5-V: VS parameters for the Equilibria in the **Table 5-IV**

Equil	γ [s^{-1}]	m_s	$V0s$ [kV]	$Pow2V0s$ [MW]	$Pow10V0s$ [MW]	$Z0max2V0s$ [cm]	$Z0max10V0s$ [cm]
1	2.05	0.81	-0.005	3.05	18.45	7,64	5,64
2	3.72	0.63	-0.008	3.88	7.09	6.74	5.03
3	8.32	0.41	-0.034	54.3	438.25	9.38	6.33
4	23.43	0.23	-0.058	22.51	5.43	5.40	5.00

It is worth to notice that, for the DN configuration, due to the symmetry of coils and equilibrium currents, the imbalance current due to the scenario currents is almost null. This is a positive effect for active power requested for VS.

Starting from the SN and DN baseline (reference) configurations (**Table 5-III**), open loop non-linear dynamical simulations have been produced for different physical and non-physical perturbations, in order to evaluate the vertical stability control system performances. The scheme is shown in **Figure 5.24**. The input voltage of the VS control system “ $V_{imbalance}$ ” is obtained according to the “best achievable performance” definition, as the double of the voltage $V0$ needed to stop a vertical displacement of 5 cm on the unstable mode at infinity.

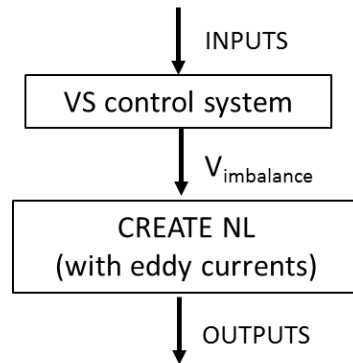


Figure 5.24: open-loop non-linear dynamical simulation scheme.

DEMO active stabilization circuit has the same structure as the ITER VS1 circuit: poloidal field coils P2⁵ and P3 are in parallel whereas P4 and P5 are in anti-parallel (**Figure 5.25** and [5.16]).

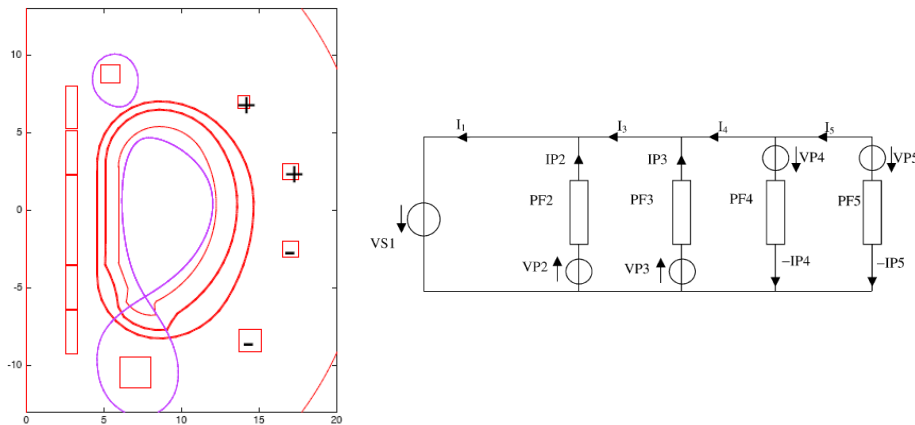


Figure 5.25: Scheme of the circuit for vertical stabilization scheme (VS1).

An assessment of the effect of critical disturbances, modelled as a variation of poloidal beta ($\Delta\beta_{pol}$) and internal inductance (Δl_i), on the vertical and radial plasma displacement is considered. In the simulations, the following assumptions have been considered:

⁵ The Poloidal Field coils are clockwise oriented.

- the eddy currents originating in the passive structures are always taken into account;
- a constant voltage on the imbalance circuit (given by the best achievable performance) is applied;
- the presence of the ports roughly has been modelled removing 1/3 of the conductive elements in correspondence of each port;
- the plasma current has been kept constant during the simulation.

Here the results of the simulations carried out considering only “physical” perturbations are reported. In particular, only the ELM (Edge Localised Mode) and the minor-disruption cases are reported (**Table 5-VI**). ELM has been modelled according to different models; the ELM model 2, in which $\Delta\beta_{pol} = -0.1$ and $\Delta I_i = +0.1$, is the one used also in ITER and probably the most reliable.

Table 5-VI: *physical perturbations list.*

$\Delta\beta_{pol}$	ΔI_i	
- 0.1	0	ELM (model 1)
- 0.1	+ 0.1	ELM (model 2)
- 0.1	- 0.1	minor-disruption

Figure 5.26 shows, for each perturbation, the plasma boundary at the maximum displaced position during the simulation. It is evident that a minor-disruption represents the worst case in terms of plasma boundary displacement.

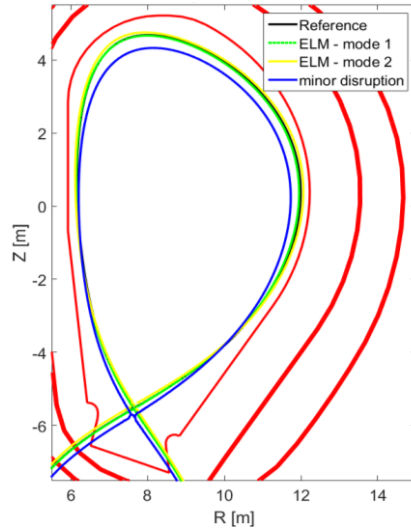


Figure 5.26: DEMO SN plasma boundaries at the maximum displaced position during the simulation for the perturbations listed in **Table 5-VI**.

Through dynamical simulations the evolution of several plasma geometrical and current parameters could be studied; e.g. **Figure 5.27** shows the time evolution of plasma current centroid radial and vertical coordinates.

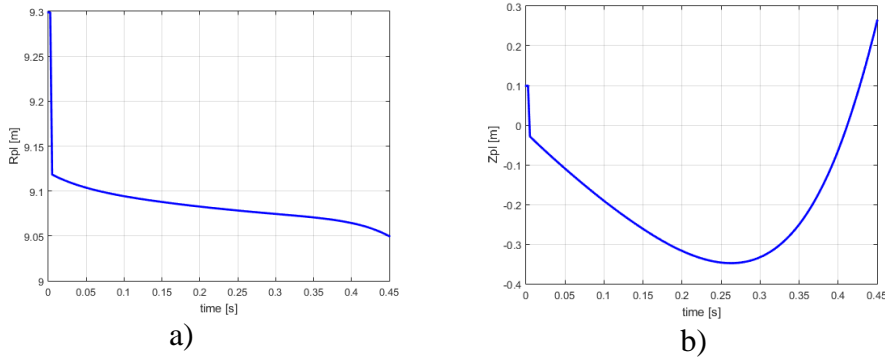


Figure 5.27: Time evolution of the plasma current centroid
a) radial position and b) vertical position (minor disruption case).

Table 5-VII and **Table 5-VIII** list, respectively, the main plasma boundary and current centroid parameters for the three perturbations considered. In particular, concerning **Table 5-VII**:

- r_{max} represents the point of the plasma boundary assuming the maximum radial coordinate (radially the most external boundary point) during the simulation;
- z_{max} represents the point of the plasma boundary assuming the maximum vertical coordinate (the upper boundary point) during the simulation;
- $\Delta r(r_{max})$ and $\Delta z(z_{max})$ represent, respectively, the radial and the vertical displacements of the two point just described during the simulation with respect to the reference case;
- *Eucl. dist.* represents, instead, the Euclidean distance between r_{max} (or z_{max}) and the reference case.

Table 5-VII: Main plasma boundary parameters in the different disturbance cases analysed.

	r_{max} [m]		z_{max} [m]		$\Delta r(r_{max})$	$\Delta z(z_{max})$	<i>Eucl. Dist.</i> (r_{max})	<i>Eucl. Dist.</i> (z_{max})
	r	z	r	z				
(Reference)	11.9885	0.3696	7.9816	4.6817	\	\	\	\
ELM – model 1 ($\Delta\beta_{pol} = -0.1$)	11.9478	0.3696	7.9860	4.6674	-0.0406	-0.0143	0.0406	0.0150
ELM – model 2 ($\Delta\beta_{pol} = -0.1$, $\Delta l_i = +0.1$)	12.0602	0.4136	7.9640	4.7542	0.0718	0.0726	0.0842	0.0747
Minor disruption ($\Delta\beta_{pol} = 0.1$, $\Delta l_i = -0.1$)	11.6847	0.1144	8.2720	4.0045	-0.3038	-0.6771	0.3968	0.7368

Table 5-VII lists main plasma current centroid parameters.

Table 5-VIII: Main plasma current centroid parameters in the different disturbance cases analysed.

	centroid [m]		Δr (centroid)	Δz (centroid)	Eucl. dist.
	r	z			
(Reference)	9.3003	0.1013	\	\	\
ELM – model 1 ($\Delta\beta_{pol} = -0.1$)	9.2376	0.0893	-0.0628	-0.0120	0.0639
ELM – model 2 ($\Delta\beta_{pol} = -0.1$, $\Delta l_i = +0.1$)	9.3520	0.1701	0.0516	0.0688	0.0860
Minor disruption ($\Delta\beta_{pol} = 0.1$, $\Delta l_i = -0.1$)	9.0773	-0.3480	-0.2230	-0.4493	0.5016

As it was already evident in **Figure 5.26**, the minor-disruption event represents the worst-case in terms of plasma boundary displacement. In this case, with respect to the reference equilibrium, the maximum boundary radial value (r_{max}) undergoes to a displacement of 30 cm, the maximum vertical value (z_{max}) moves around 67 cm whereas the Euclidean displacement of plasma current centroid is around 50 cm. Applying the same perturbations to the DN case, once more the worst-case is represented by the minor-disruption, as it is possible to observe in **Table 5-IX**.

Table 5-IX: Main plasma current centroid parameters in the different disturbance cases analysed.

	Centroid [m]		Δr (centroid)	Δz (centroid)	Eucl. Dist.
	r	z			
(Reference)	8.5367	0.0013	\	\	\
ELM – model 1 ($\Delta\beta_{pol} = -0.1$)	8.4795	-0.0207	-0.0572	-0.0221	0.0613
ELM – model 2 ($\Delta\beta_{pol} = -0.1$, $\Delta l_i = +0.1$)	8.5964	-0.0155	0.0597	-0.0169	0.0620
Minor disruption ($\Delta\beta_{pol} = 0.1$, $\Delta l_i = -0.1$)	8.3439	-0.0432	-0.1928	-0.0446	0.1979

For the DN case, only the plasma current centroid parameters have been considered in the comparison since the boundary geometrical parameters taken into account in the SN case make no sense.

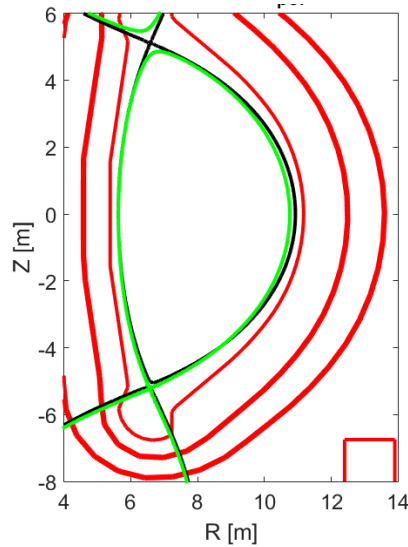


Figure 5.28: DN plasma separatrix in case of minor disruption perturbation.

Figure 5.28 shows the maximum displacement of the plasma contour during perturbation.

It can be immediately observed that, for a DN plasma, even in the worst-case of minor-disruption, the vertical displacement of the plasma centroid ($\Delta z_{centroid}$) is around ten times smaller than in case of SN ($\approx 4.5\text{ cm}$). This comparison is not properly “fair” since SN and DN having different plasma and geometrical parameters are compared. Section 5.4.4 presents a SN-DN fair comparison.

5.4.4 A DEMO SN-DN “fair comparison”

In order to perform a “fair comparison” between the DEMO Single Null and Double Null configurations with the aim to highlight advantages and drawbacks in terms of Vertical Stability controllability, SN and DN configurations having the same nominal values of elongation and triangularity have been produced. In particular, for the triangularity at 95% the value $\delta_{95\%} = 0.33$ has been chosen whereas for the elongation

at 95% the two values $k_{95\%} = 1.59$ and $k_{95\%} = 1.71$ have been considered. **Figure 5.29** shows the different configurations.

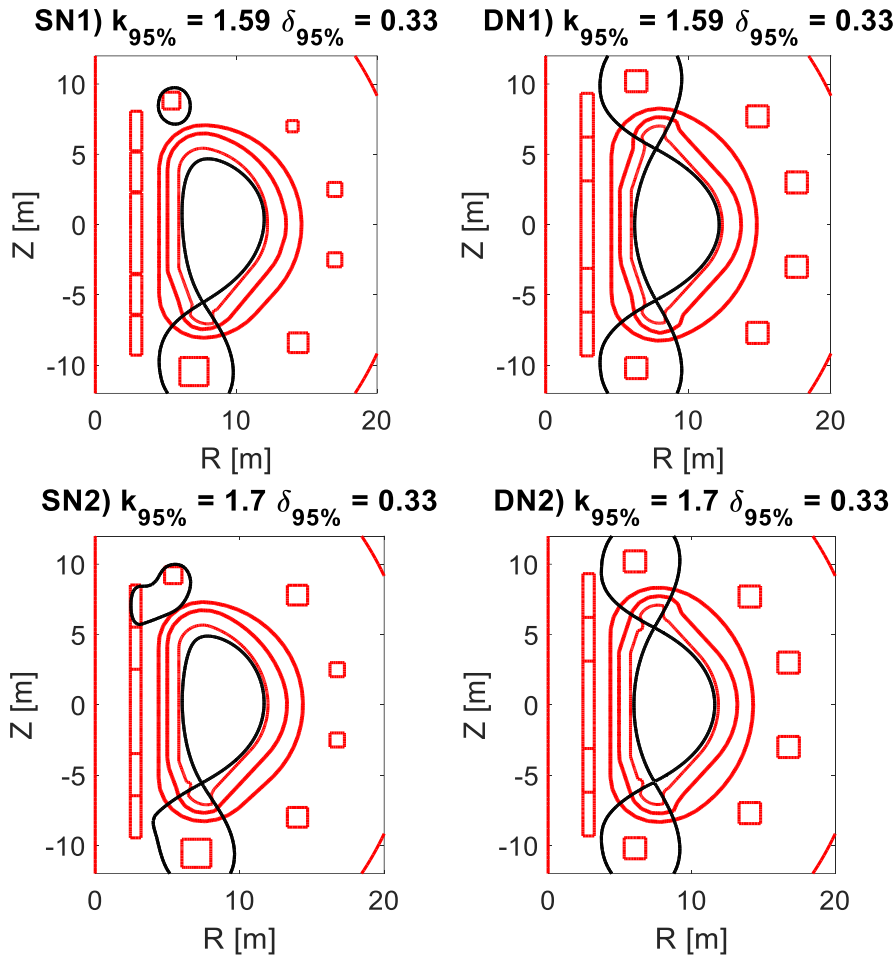


Figure 5.29: SN and DN configurations used for a “fair comparison”. [5.19]

For the Vertical Stability analysis, the same physical perturbations listed in **Table 5-VI** and the same assumptions described in Section 5.4.3 for the non-linear open loop simulations have been considered. The simulations are stopped when the plasma is recovered, i.e. the plasma comes back to the initial position.

Table 5-X shows that, regardless the nominal elongation of the configurations, *the growth rate (γ) of the SN is always less than the DN configurations*. This circumstance is mainly related to the presence of the upper divertor in the DN geometry that increases the relative distance between plasma and passive structures.

Table 5-X: Comparison SN-DN configurations in terms of passive stability parameters: growth rate (γ) and stability margin (m_s)

Configurations	γ [s^{-1}]	m_s
SN1 @ SOF k95%=1.61	2.55	0.81
DN1 @ SOF k95%=1.61	6.75	0.58
SN2 @ SOF k95%=1.7	5.59	0.56
DN2 @ SOF k95%=1.7	9.25	0.37

Table 5-XI remarks that, in case of VDE, while the power request of DN configurations on the vertical stabilization circuit (P_{VS}) is higher than the SN case, *the total power on the imbalance circuit (P_{TOT}) for DN configurations is considerable less than in the SN case*. This result is mainly due to the up-down symmetry of the DN configurations that makes zero the imbalance current of the scenario. Z_{max} represents the maximum vertical displacement of the plasma current centroid during the simulation.

Table 5-XI: Comparison SN-DN configurations in case of a 5cm VDE.

Configurations	Z_{max} [cm]	P_{VS} [MW]	P_{TOT} [MW]
SN1 @ SOF k95%=1.61	7.5	3	93
DN1 @ SOF k95%=1.61	7.5	24	24
SN2 @ SOF k95%=1.7	7.4	13	77
DN2 @ SOF k95%=1.7	8.5	61	61

Table 5-XII reports the best achievable performance in case of an ELM (always modelled as variation in β_p and l_i parameters $\Delta\beta_p = -0.1$ and $\Delta l_i = -\Delta\beta$); Z_0 is the initial displacement of the plasma current centroid due to the applied perturbation. Due to the coincidence in ideal DN configurations of the plasma centroid and the magnetic axis, in case of ELM, *the vertical displacement of the plasma is much lower than the SN*. This aspect, added to the up-down symmetry of the DN

configurations, make *the total power requests of the DN configurations orders of magnitude less than the SN case.*

Table 5-XII: Comparison SN-DN configurations in case of ELMs

Configurations	Z_0 [cm]	Z_{max} [cm]	P_{VS} [MW]	P_{TOT} [MW]
SN1 @ SOF k95%=1.61	5.0	24.7	16	221
DN1 @ SOF k95%=1.61	0.7	0.7	0.1	0.1
SN2 @ SOF k95%=1.7	2.3	16.0	6	54
DN2 @ SOF k95%=1.7	0.9	1.8	1.3	1.3

5.5 Conclusions

The knowledge of position and shape of the plasma column inside the vacuum chamber represents a critical issue playing a key role in large scale fusion devices efficient and safe operation. In the present Chapter, the magnetohydrodynamic model, describing the behaviour of a plasma, and the theoretical basis of the plasma boundary reconstruction are introduced. The final part is focused on the CREATE-NL+ code used for the plasma equilibria design and dynamic simulations of the plasma response to instabilities.

The main contributions illustrated in this Chapter are related to the optimization of the design of the poloidal field coils in standard and alternative plasma magnetic configurations and to the analysis of the active and passive vertical stability properties of the evolving magnetic configurations. The optimization criteria and method are described, from the output of the systems code to the implementation of ports, taking pre-magnetisation and plasma configurations into account. Examples are given of standard and alternative magnetic configurations for a demonstration fusion reactor (DEMO). The stability of equilibria against external perturbations is then investigated. Vertical stability analyses of single versus double null magnetic configurations for DEMO are then performed. The results mainly show that the vertical stability of double null equilibria would behave much more benign, with a much lower vertical displacement in case of external

perturbations, and therefore they would require much lower power to stabilise their vertical position.

References

- [5.1] A. Beghi and A. Cenedese, “Advances in Real-Time Plasma Boundary Reconstruction”, IEEE Control Systems (Vol. 25, Oct. 2005), DOI: 10.1109/MCS.2005.1512795
- [5.2] R. Albanese, J. Blum, and O. DeBarbieri, “Numerical studies of the next European torus via the PROTEUS code,” in Proc. 12th Conf. Numerical Simulation Plasmas, San Francisco, CA, 1987, IT4
- [5.3] M. Cavinato, A. Kavin, V.E. Lukash, and R.R. Khayrutdinov, “Non-linear simulations by numerical magneto hydro dynamics equilibrium codes in ITER-FEAT,” in Proc. IEEE Int. Conf. Control Applications (CCA), Anchorage, AK, 2000, pp. 406–411.
- [5.4]] L.L. Lao, H. St. John, R.D. Stambaugh, A.G. Kellman, and W. Pfeiffer, “Reconstruction of current profile parameters and plasma shapes in tokamaks,” Nucl. Fusion, vol. 25, no. 11, pp. 1611–1622, 1985.
- [5.5] F. Sartori, A. Cenedese, and F. Milani, “JET real-time object-oriented code for plasma boundary reconstruction,” Fusion Eng. Des., vol. 66–68, pp. 735–739, 2003.
- [5.6] D.W. Swain and G.H. Neilson, “An efficient technique for magnetic analysis of noncircular, high-beta tokamak equilibria,” Nucl. Fusion, vol. 22, no. 8, pp. 1015–1030, 1982.
- [5.7] L.L. Lao, H. St. John, R.D. Stambaugh, A.G. Kellman, and W. Pfeiffer, “Reconstruction of current profile parameters and plasma shapes in tokamaks,” Nucl. Fusion, vol. 25, no. 11, pp. 1611–1622, 1985.
- [5.8] R. Albanese, R. Ambrosino, M. Mattei, “CREATE-NL+: A robust control-oriented free boundarydynamic plasma equilibrium solver”, FED 96–97 (2015) 664–667
- [5.9] R. Albanese, et al., “Plasma response models for current, shape and position control in JET”, Fusion Eng. Des. 66–68 (2003) 715–718.
- [5.10] R. Albanese, J. Blum, O. Barbieri, On the solution of the magnetic flux equation in an infinite domain, in: EPS. 8th Europhysics Conference on Computing in Plasma Physics, 1986.

- [5.11] M. Kovari, R. Kemp, et al, “<<PROCESS>>: a Systems Code for Fusion Power Plants - Part 1: Physics”, CCFE-PR(14)12
- [5.12] R. Ambrosino, R. Albanese, A. Castaldo, V. P. Loschiavo, S. McIntosh, H. Reimerdes, “Final report: DTT1-AC3: Equilibrium generation”, June 2016, <https://idm.euro-fusion.org/>, EFDA_D_2MPYDL
- [5.13] S. Ejima, et al, “Scaling of energy confinement with minor radius, current and density in Doublet III Ohmically heated plasmas”, Nuclear Fusion, Volume 22, Number 12, Pages 1627
- [5.14] Lazarus E.A. et al, 1990, Nucl. Fusion 30 111
- [5.15] Crisanti F. et al 2003 Fusion Eng. Des. 66–68 803–7
- [5.16] Gribov Y. et al 2007, “Progress in the ITER Physics Basis: chapter 8. Plasma operation and control”, Nucl. Fusion 47 S385
- [5.17] S. L. Chen, F. Villone, et al., “Effect of three-dimensional conducting structures on vertical stability in EAST”, Nucl. Fusion 55 (2015) 013010 (11pp)
- [5.18] R. Albanese, R. Ambrosino, V. P. Loschiavo, “Single null and Double null DEMO reference configurations vertical stability analysis”, December 2016, <https://idm.euro-fusion.org/>, ANNEX 1 to EFDA_D_2MP7Z8.
- [5.19] R. Albanese, R. Ambrosino, V. P. Loschiavo, M. Mattei, “Final report on DEMO Vertical Stability investigations described in the task specification”, December 2016, <https://idm.euro-fusion.org/>, EFDA_D_2MP7Z8

Chapter 6

“Life is like riding a bicycle. To keep your balance, you must keep moving.”

Albert Einstein

DEMO divertor target tiles 2D and 3D thermo-mechanical analyses in the strike-point sweeping case

During tokamak operation, different types of high-energy ionized particles are produced and leave the plasma after the confinement time. The particles escaping from the plasma enter the scrape-off-layer (SOL) region and reach the Divertor region. The particles reaching the Divertor region cause a localized thermal load around the strike-points, i.e. the intersections of the separatrix with the divertor. To spread on a larger region this thermal load, it is convenient to resort to a periodical movement of the strike-points [6.1]. The different techniques providing this movement can be classified in “*strike point sweeping*”, if it generates a movement of the only region of plasma boundary close to the X-point keeping the rest of the shape practically unchanged, and “*wobbling*”, in which the whole plasma is displaced periodically in a rigid way (as illustrated conceptually in the Section 4.3).

In this Chapter, after a brief introduction describing the possibilities to implement the strike-point sweeping technique in fusion experimental devices, a 2D model of the DEMO divertor target tiles and the results of a thermal analysis carried out are presented, showing the advantages of the strike-point sweeping technique. In the second part of the Chapter, the results of a 3D model are presented taking into account also the fatigue lifetime of the divertor component. Finally, a preliminary analysis on the wobbling technique applied to a DEMO Double Null plasma magnetic configuration is illustrated.

6.1 The strike-point sweeping technique

The “strike point sweeping” technique consists in a periodical movement of the strike points. This technique has been already successfully applied to different tokamaks. In JET, for example, different model-based algorithms for the strike-point sweeping have been presented and implemented within the JET XSC (eXtreme Shape Controller) architecture allowing to perform experimentally the strike-point sweeping without affecting the plasma-boundary shape control ([6.1] and [6.2]).

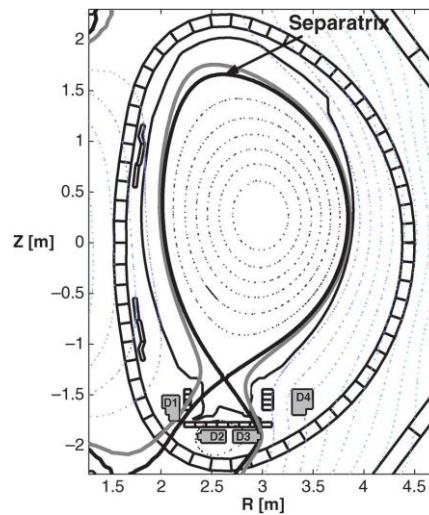


Figure 6.1: Poloidal cross section of the JET tokamak. The four divertor coils (D1–D4) are shown.

In order to give an idea on how the strike-point sweeping technique can be realized in an experimental device, at the Joint European Torus (JET) tokamak the standard sweeping strategy adopted is implemented within the Shape Controller (SC) architecture. In this case, the strike-point sweeping is performed with a 4-Hz triangular reference for either the currents in the divertor coils D2 and D3 shown in **Figure 6.1** ([6.1]).

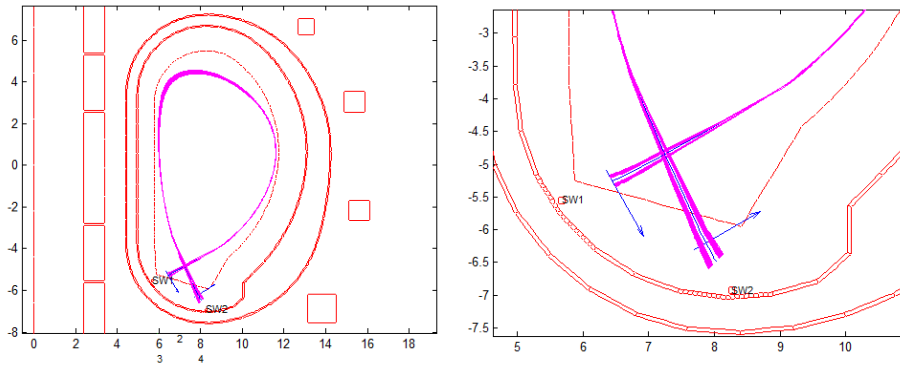


Figure 6.2: Plasma boundary modification in the presence of a sinusoidal current in antiseries, with a frequency from 0 to 5 Hz and an amplitude of 240 kA (170 kA rms). [6.3]

The strike-point sweeping is usually produced by sinusoidal currents flowing in dedicated sweeping coils. **Figure 6.2** shows the plasma boundary modification for a DEMO standard SN configuration in the presence of a sinusoidal current flowing in dedicated in-vessel sweeping coils. The eddy currents and hysteresis phenomena resulting from the varying magnetic field yields AC losses, and lead to the heating of the superconductive coils, decreasing their cooling capabilities. Therefore, an important task in the development of the strike-point sweeping technique is the assessment of the power required for the sweeping and the AC losses in the superconductors. In Section 6.1.1, a preliminary assessment for the DEMO fusion reactor is presented.

6.1.1 A preliminary assessment of the sweeping power requirements and AC losses in DEMO

In DEMO, some preliminary analysis has been carried out on the possibility to realize the strike-point sweeping through dedicated in-vessel coils [6.3].

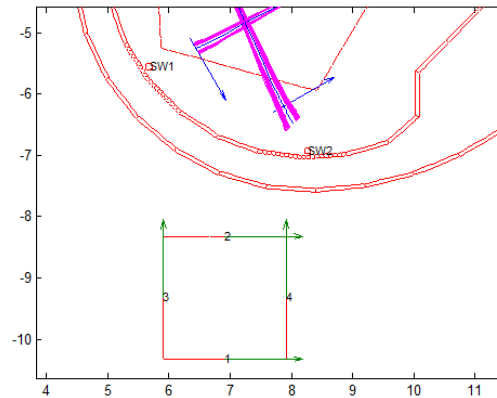


Figure 6.3: Sweeping coils in anti-series and four field measurements on the jacket of the closest PF coil. [6.3]

The analysis was performed on the installed power required for the strike point sweeping, by using the CREATE L [6.4] model of a DEMO standard Single Null equilibrium [6.3]. Two sweeping copper coils were preliminarily considered (**Figure 6.3**). These are located 80 cm behind the divertor, to allow the possibility to provide a sufficient neutron shielding, not yet analysed, and enable maintenance. The sweeping coils considered present similar size and carry a similar current as the ITER in-vessel VS coils. This solution presents non-negligible integration issues, but some experience will be gained from the ITER VS in-vessel coils [6.5]. An alternative solution could be represented by the use of saddle coils in each toroidal sector, integrated in the divertor cassette, and replaceable with the time scale of the DEMO divertor. A sinusoidal current with an amplitude of 240 kA (170 kA rms) and a frequency from 0 to 5 Hz was considered. The figure of 240 kA is the nominal current for the internal VS coils in ITER. While the required power scales quadratically, most other relevant parameters, such as strike point motion, plasma motion, magnetic field, etc., have a linear dependence on the sweeping coil current. The power needed for sweeping in the above conditions with the current considered is:

- active power of 0.30 MW at 0.2 Hz, 3.3 MW at 1 Hz;
- reactive power of 3.5 MVar at 0.2 Hz, 16 MW at 1 Hz.

At the low frequency considered, it is possible to realise a sweep of up to 26 cm peak-to-peak on the outer strike-point and 19 cm on the inner strike-point.

An estimation of the AC losses in the superconductive coils closer to the divertor was also performed (**Figure 6.3** shows also the points where the magnetic field is calculated for the AC loss analysis of the closest superconducting PF coil). At low frequency the maximum dB/dt is about 15 mT/s rms at 0.2 Hz and 60 mT/s rms at 1 Hz. The maximum temperature increase is of 0.03 K, at 1 Hz. This did not include the hysteresis losses that might also play a role. If a conservative figure of a total of 0.1 K is considered, this is comparable with the AC losses due to the DEMO scenario, which are of the order of 0.3 K, then they are not negligible. A preliminary estimation, based on ITER superconductor technology does not exclude the possibility of using sweeping at the expense of an acceptable decrease of T margin in the closest superconductive coil [6.5].

After a preliminary assessment on the strike-point sweeping technique feasibility in the DEMO reactor, in terms of installed power required and AC losses in the superconductors, the subsequent step was the development of thermo-mechanical models showing advantages and drawbacks of the strike-point sweeping technique as candidate solution to the power exhaust issue.

6.2 Strike-point sweeping 2D thermal analysis

The present DEMO divertor design is based on the ITER one, even though it has to withstand higher demanding conditions on the heat exhaust. It is composed by tungsten mono-block divertor targets embedded on copper alloy CuCrZr cooling pipes, with a Cu interlayer (**Figure 6.4**).



Figure 6.4: Water-cooled tungsten mock-ups produced by CCFE and KIT. [6.6]

The coolant considered in ITER, and hence used in the analysis, is water.

A broad parametric scan has been carried out in order to assess the operational space of the strike-point sweeping technology. The 2D thermal analysis has been performed for a static case, in which the outer strike point is fixed, and for an outer strike point sweeping case, in order to quantify the main advantages of the strike-point sweeping in terms of maximum temperature decrease. In the latter case, the operational space of the strike-point sweeping technique is explored considering different values for the SPS parameters, i.e. amplitude and frequency. In particular, the two amplitude 3 and 6 cm, and the three frequencies 0.2, 0.5 and 1 Hz have been considered. Finally, also the upper thickness of the tungsten tile has been analysed, investigating the 5 and 10 mm cases in order to understand the differences.

6.2.1 Model assumptions

In order to develop a simple 2D model of the DEMO divertor, a simplified cross-section geometry has been considered (**Figure 6.5**). At a first stage, a cooling Cu-alloy pipe having an inner diameter of 14 mm and a 1.5 mm thickness has been considered, neglecting the presence of the soft copper layer (in a first approximation this assumption does not involve a big error because of the similar thermal conductive properties of the two materials).

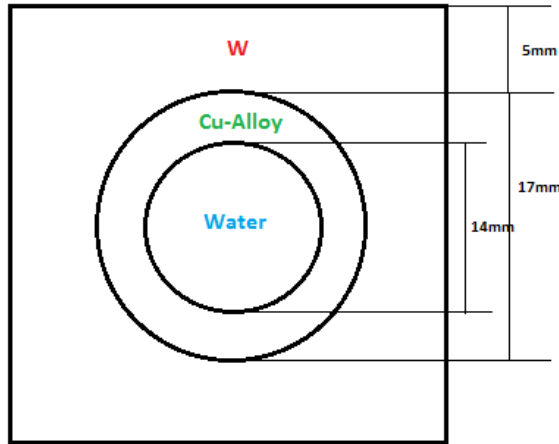


Figure 6.5: DEMO divertor tile geometry

Other simplifying assumption are the following:

- the radiation on the upper bound (this is probably the most inaccurate assumption) is neglected;
- the water and the tungsten phase transitions (i.e. the sub-cooled vapour for the water and the evaporation and the melting for the tungsten layer) are neglected;
- the mesh considers only the W and Cu layers modelling the convective heat transfer between Cu and water as boundary condition (the water is assumed at a fixed temperature of 200°C); i.e. the velocity profile into the pipe and the time variation (due to the changing temperature) of the main heat transfer parameters (Nu, Pr, etc.) are neglected.

A 30 MW conductive heat power impinging on the outer target tile surface and a background heat power density (mainly due to the neutrons) of $2.5\text{ MW}/\text{m}^2$ are considered, with a resulting heat flux profile shown in **Figure 6.6** and given by the empirical formula (6.1):

$$\dot{q}_{plasma} = \dot{q}_0 \cdot 0.5 \cdot e^{\frac{S^2}{4\lambda^2} - \frac{x}{f_x S}} \cdot \operatorname{erfc}\left(\frac{S}{2\lambda} - \frac{x}{f_x S}\right) + \dot{q}_{BG} \quad (6.1)$$

with:

- $\dot{q}_0 = 147.44 \text{ MW/m}^2$ (pre-factor);
- $S = 0.0045 \text{ m}$ (Gaussian width);
- $\lambda = 0.0008 \text{ m}$ (λ_q or power decay length);
- $f_x = 6$ (total flux expansion);
- $q_{BG} = 2.5 \text{ MW/m}^2$ (background heat power density).

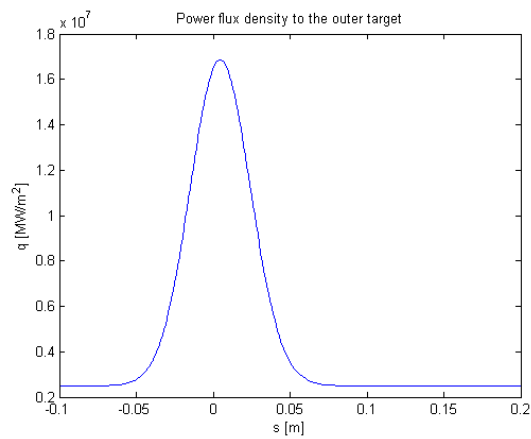


Figure 6.6: Divertor target heat flux profile.

In Eq. (6.1) “ x ” is the longitudinal coordinate, parallel to the pipe axis. The resulting plasma heat flux footprint is shown in **Figure 6.7**.

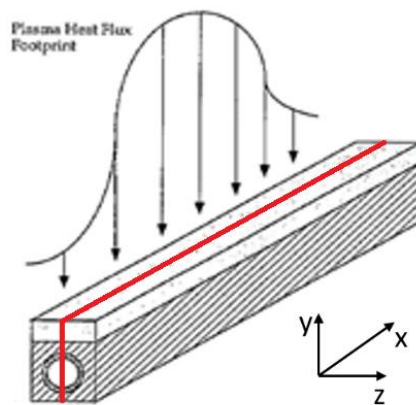


Figure 6.7: Plasma heat flux footprint

Because of the heat flux profile impinging on the divertor target tiles, the problem becomes a 3D thermal problem. In order to reduce it to a 2D problem, 50 cm of the structure along the x axis are considered, at the vertical mid-plane of the cross-section (red plane highlighted in **Figure 6.7**). The continuity between the tiles is considered whereas the pipe curvature is neglected assuming a shape correction factor f_{corr} .

6.2.2 Thermal analysis

The bi-dimensional multi-domain¹ conductive problem is described by the parabolic partial differential equation:

$$\nabla \cdot (k\nabla T) = \rho c \frac{\partial T}{\partial \theta} \quad (6.2)$$

Usually, the contribution of the neutrons to the heat load is modeled as a volumetric heat flux (\dot{q}_v) but in this analysis it is taken into account only through the background heat power density (\dot{q}_{BG}) in the heat flux density profile (6.1).

The boundary conditions are the following:

$$\begin{aligned} T_W(x, y, 0) = T_{Cu}(x, y, 0) = 116^\circ\text{C} & \quad 0 \leq x \leq L_x, 0 \leq y \leq L_y \\ -k_{Cu} \frac{\partial T(0, y, \theta)}{\partial x} = 0 & \quad 0 \leq y \leq L_{y,Cu}, \theta > 0 \\ -k_{Cu} \frac{\partial T(L_x, y, \theta)}{\partial x} = 0 & \quad 0 \leq y \leq L_{y,Cu}, \theta > 0 \\ -k_{Cu} \frac{\partial T(x, 0, \theta)}{\partial y} & = \bar{h}_{c,eff}(T_{Cu,lower} - T_w) \quad 0 \leq x \leq L_x, \theta > 0 \\ -k_{Cu} \frac{\partial T(x, L_{y,Cu}, \theta)}{\partial y} & = -k_W \frac{\partial T(x, L_{y,Cu}, \theta)}{\partial y} \quad 0 \leq x \leq L_x, \theta > 0 \end{aligned}$$

¹ There are two domains, the tungsten (W) and the copper (Cu).

$$\begin{aligned}
 -k_W \frac{\partial T(0, y, \theta)}{\partial x} &= 0 & L_{y,Cu} \leq y \leq L_{y,W}, \theta > 0 \\
 -k_W \frac{\partial T(L_x, y, \theta)}{\partial x} &= 0 & L_{y,Cu} \leq y \leq L_{y,W}, \theta > 0 \\
 -k \frac{\partial T(x, L_{y,W}, \theta)}{\partial y} &= \dot{q}_{plasma}(\theta) & 0 \leq x \leq L_x, \theta > 0
 \end{aligned}$$

All the heat transfer coefficients (conductivity, specific heat, etc.) are temperature dependent, except the heat transfer convective coefficient $\bar{h}_{c,eff}$, which has been assumed constant and equal to:

$$\bar{h}_{c,eff} = \bar{h}_c \cdot f_{corr}$$

In particular:

- $\bar{h}_c = 45400 \text{ W/m}^2\text{K}$ is the \bar{h}_c for the single phase water;
- $f_{corr} = 3/5$ is the shape correction factor, evaluated as the ratio of the water pipe diameter to the W layer width.

The other heat transfer coefficients used in the analysis [6.8] are shown in the diagrams below.

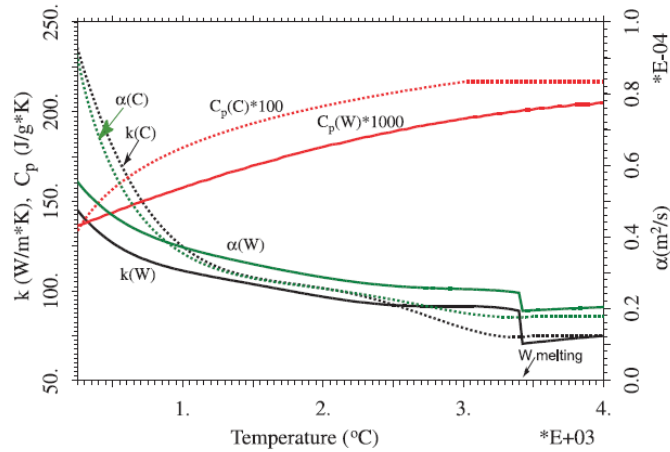


Figure 6.8: thermal properties (thermal conductivity, k , specific heat C_p , and thermal diffusivity, $k/\rho c_p$) of W and CFC as a function of the temperature used in the model. [6.8]

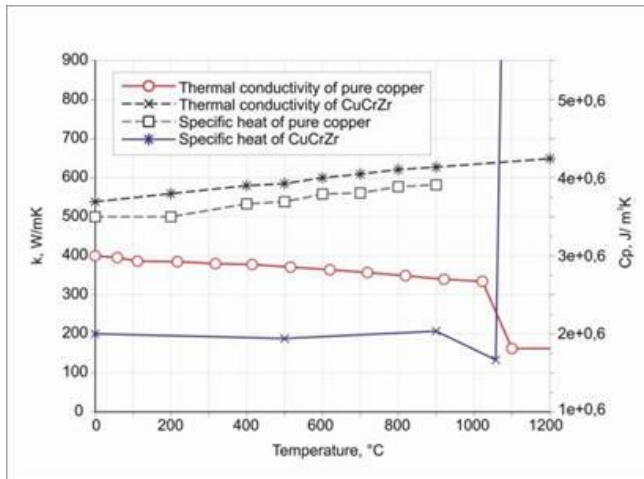


Figure 6.9: Thermal properties (thermal conductivity, k , specific heat C_p) of Cu-Alloy and Cu as a function of the temperature used in the model. [6.8]

The initial 3D problem has been reduced to a 2D multi-domain conductive problem resorting to simplifying hypotheses. However, the power flux density \dot{q}_{plasma} profile (appearing in the last boundary condition), specified in **Figure 6.6** and Eq. (6.1), is time dependent in the strike-point sweeping case, complicating the problem with a time-varying boundary condition.

This kind of problem, governed by the parabolic partial differential equation (6.2), can be solved by different numerical methods.

The numerical method chosen for this analysis is the so-called “*method of lines*”. The method of lines is a “semi-discretization” method that proceeds by first discretizing the spatial derivatives only and leaving the time variable continuous [6.9]. This leads to a system of ordinary differential equations to which a numerical method for initial value ordinary equations can be applied

This method has been implemented in MATLAB® environment.

As first step, a triangular mesh, modeling only the W (upper) and the Cu (lower) layers, has been produced (**Figure 6.10**).

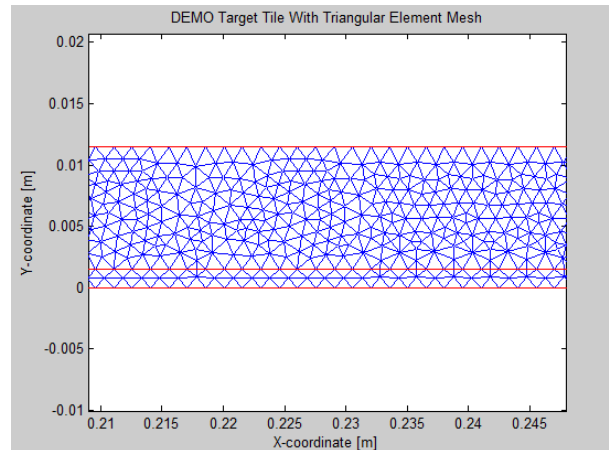


Figure 6.10: MATLAB triangular mesh (zoom) modeling the W (upper) and the Cu-alloy (lower) layers (case of $W_width = 10\text{ mm}$)

Once the space has been discretized, all the finite element matrices corresponding to the problem are created yielding the matrix notation:

$$M \frac{dT}{dt} + KT = F$$

where M , K and F are, respectively, the mass matrix, the stiffness matrix and the load vector. The numerical integration of the resulting ODE system is performed by the MATLAB® ODE Suite functions, which are efficient for this class of problems. In particular, the ODE15s has been chosen, since it is a variable-step, variable-order (VSVO) solver based on the numerical differentiation formulas (NDFs) of orders 1 to 5 employing an implicit method (suitable for stiff problems), and hence unconditionally stable. It is also a multi-step algorithm, using the results of several past steps.

The code implemented in the MATLAB® environment takes less than one minute to run. The analysis main results are shown below.

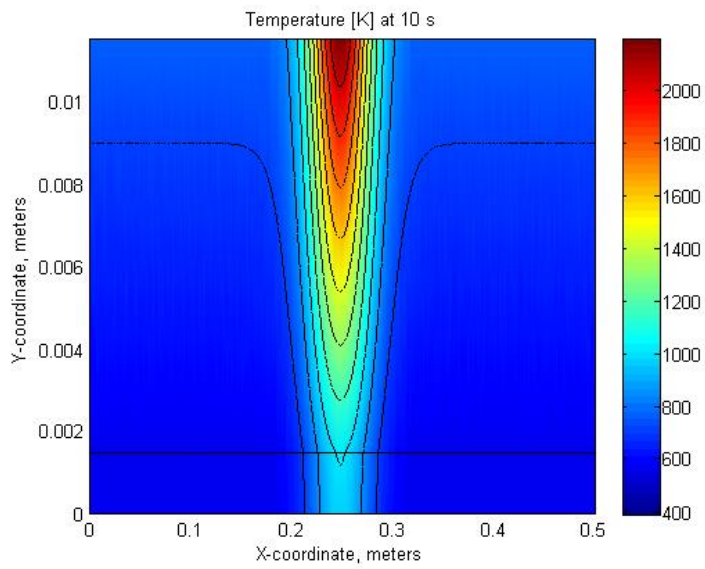


Figure 6.11: temperature contours obtained fixing the outer strike point in the case $W_thickness = 10mm$

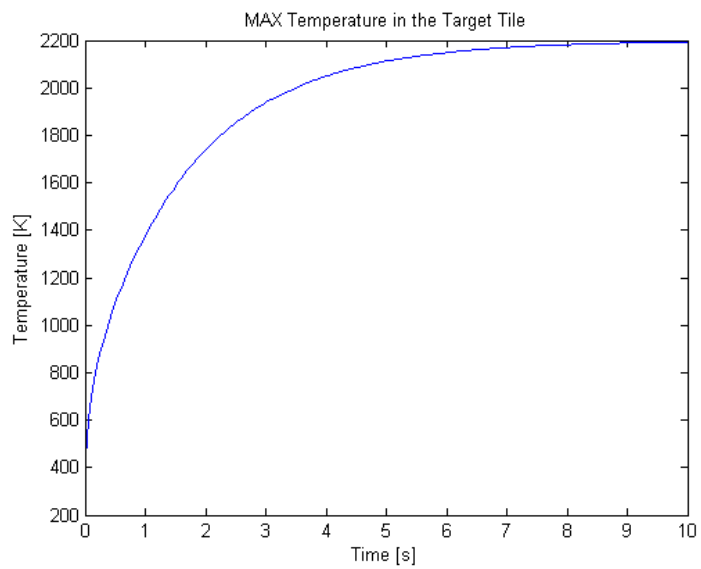


Figure 6.12: maximum temperature evolution obtained fixing the outer strike point in the case $W_thickness = 10mm$

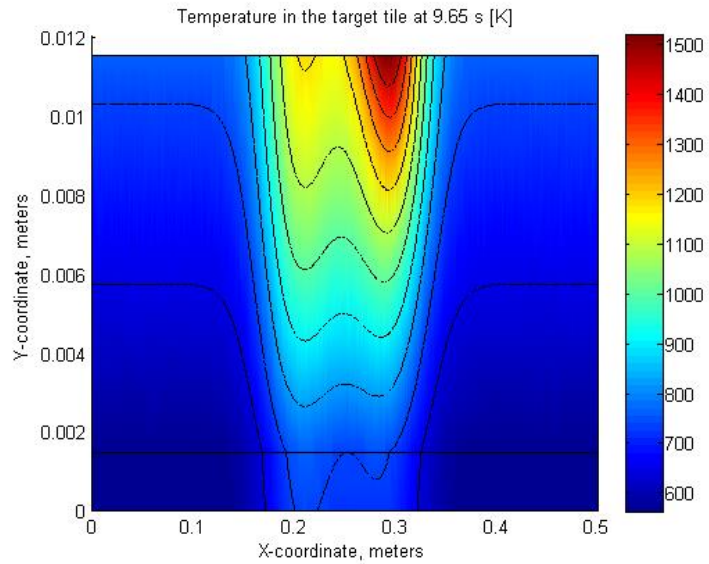


Figure 6.13: temperature contours - obtained in the case $W_{thickness} = 10\text{ mm}$ sweeping the outer strike point with Amplitude = 6cm and Frequency = 1Hz (the image refers to the instant in which the maximum temperature is reached)

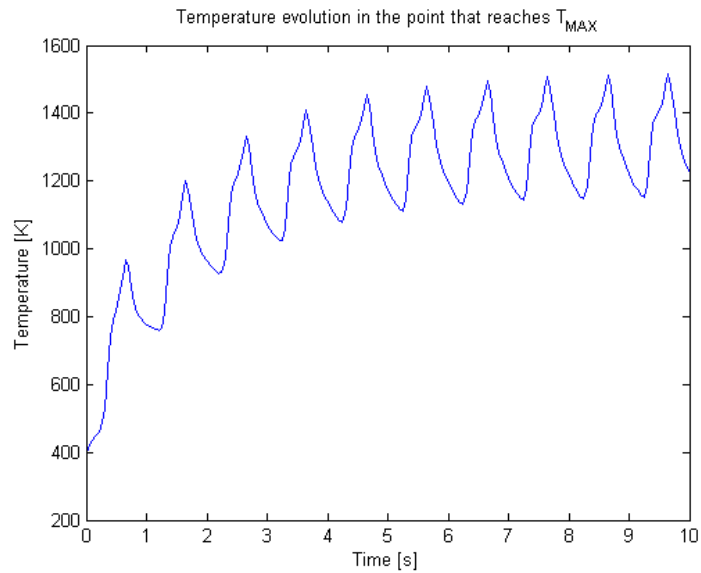


Figure 6.14: temperature evolution in the point that reaches the maximum temperature during the transient process - obtained in the case $W_{thickness} = 10\text{mm}$ sweeping the outer strike point with Amplitude = 6cm and Frequency = 1Hz

Figure 6.11 and **Figure 6.12** show, respectively, the temperature contours in the domain at steady state and the time evolution of the temperature in the point that reaches the maximum value in the domain at steady state, when the outer strike point is kept fixed.

Figure 6.13 and **Figure 6.14** show, respectively, the temperature contours in the domain at the time instant in which the maximum temperature is reached in the domain at steady state and the time evolution of the temperature in the point that reaches the maximum temperature value, when the outer strike point is swept.

Figure 6.15 refers to the case already represented in **Figure 6.14** showing the evolution of the heat flux profile, taken in representative instants during the process. The magenta profile is the heat flux profile in the instant in which the maximum temperature in the tile is reached whereas the black point shows that point position in the mesh.

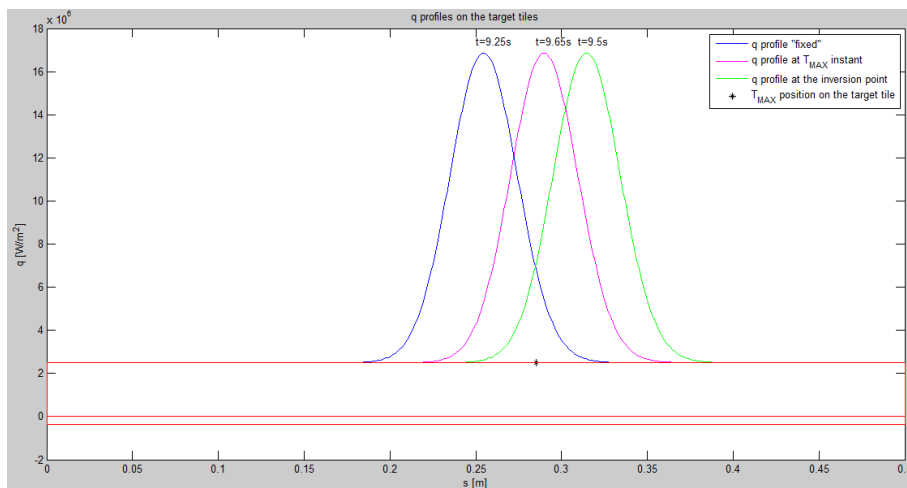


Figure 6.15: heat flux profiles taken in representative instants during the strike point sweeping process (related to Figure 6.14).

The maximum temperatures reached in the outer target tiles in the main cases discussed above are reported in **Table 6-I**.

Table 6-I: maximum temperatures reached in the domain, keeping fixed and sweeping the outer strike-point with different values of frequency and amplitude, for two different thickness of the tungsten (W) layer.

		W thickness	5 mm		10 mm	
		Amplitude	3 cm	6 cm	3 cm	6 cm
FIXED		\	1410		1920	
SWEEPING	Frequency[Hz]	0.2	1344	1268	1712	1511
		0.5	1225	1075	1592	1325
		1	1158	977	1542	1242

Figure 6.16 - Figure 6.20 illustrate graphically the same results reported in **Table 6-I**.

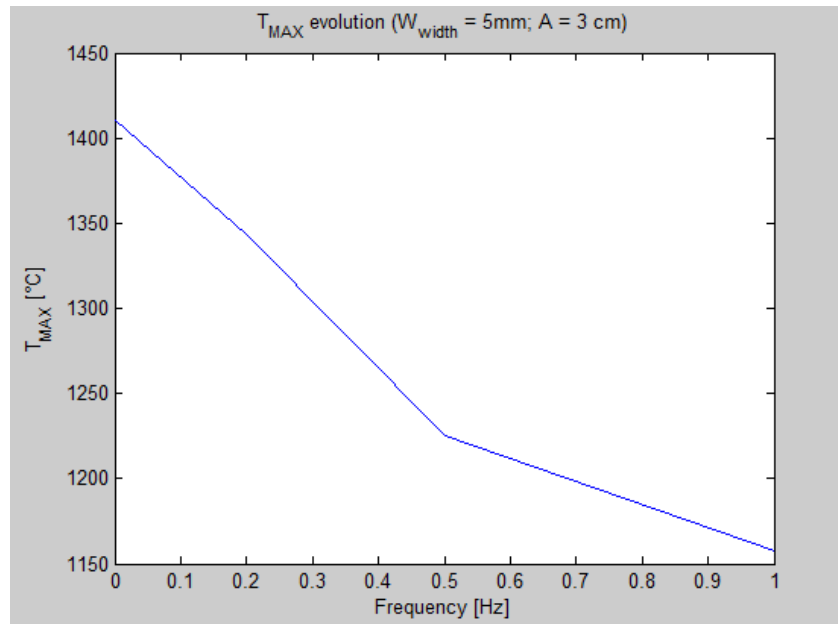


Figure 6.16: maximum temperature in the tiles as a function of the frequency ($W_{thickness} = 5mm$; Amplitude = 3cm)

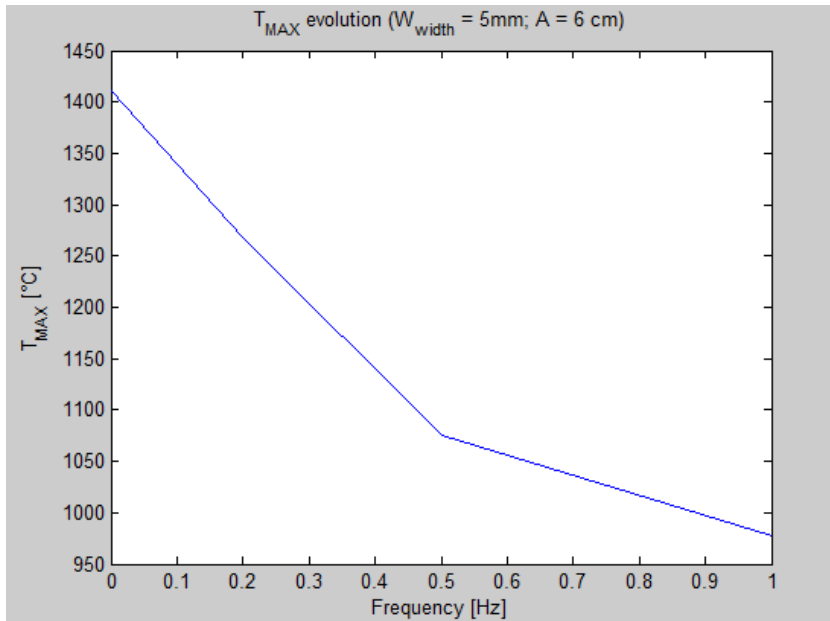


Figure 6.17: maximum temperature in the tiles as a function of the frequency ($W_{thickness} = 5\text{mm}$; Amplitude = 6cm)

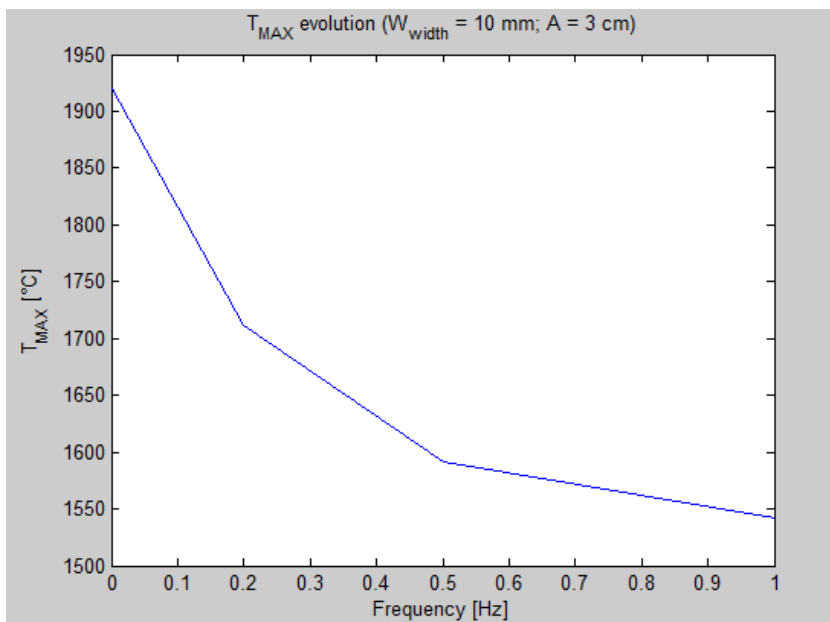


Figure 6.18: maximum temperature in the tiles as a function of the frequency ($W_{thickness} = 10\text{mm}$; Amplitude = 3cm)

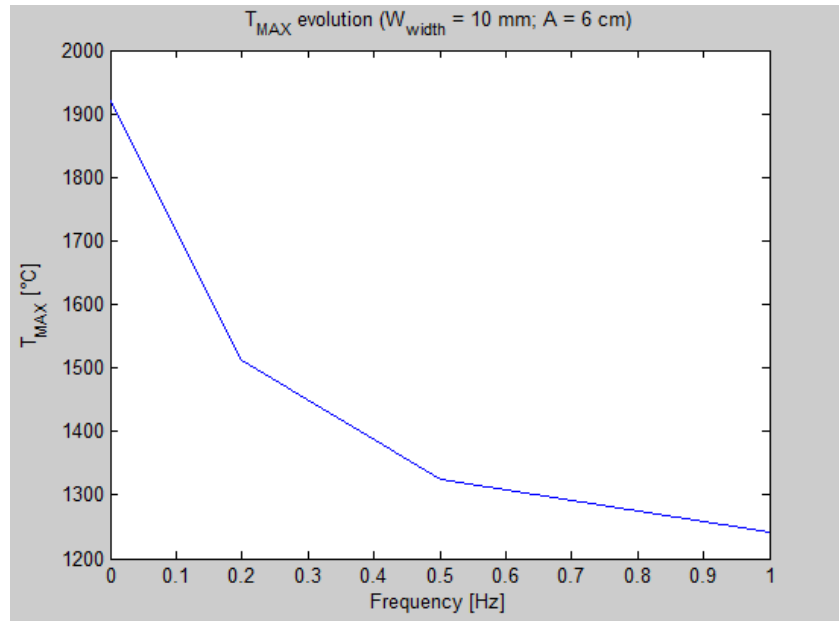


Figure 6.19: maximum temperature in the tiles as a function of the frequency ($W_{thickness} = 10\text{mm}$; Amplitude = 6cm)

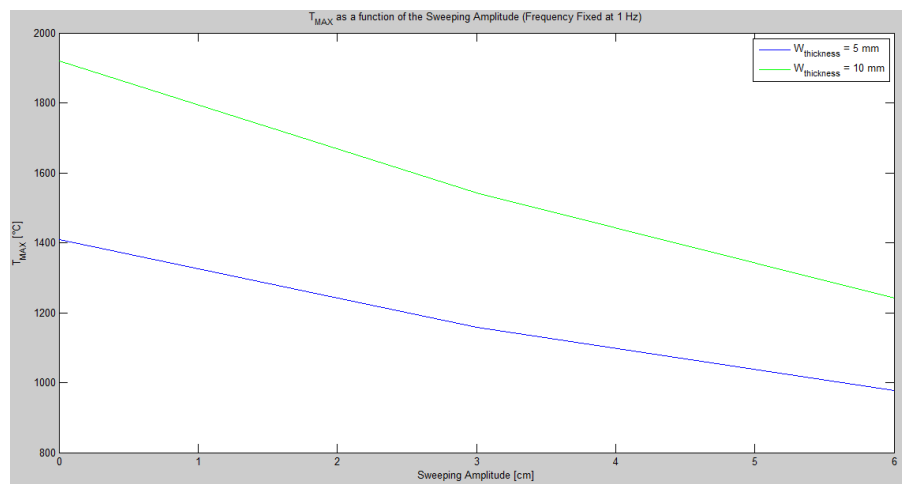


Figure 6.20: maximum temperature decrease as a function of the sweeping amplitude, fixed the sweeping frequency at 1 Hz

As it was expected, it is clearly possible to observe from **Table 6-I** and **Figure 6.16** - **Figure 6.20** that a decreasing of the maximum temperature in the tile is achievable:

- increasing the sweeping frequency;
- increasing the sweeping amplitude;
- reducing the tungsten thickness.

From the results of the analysis, e.g. referring to the variation of the tungsten layer thickness, it is possible to quantify the maximum temperature decrease, with respect to the fixed strike-point case, approximately as $70\text{ }^{\circ}\text{C}/\text{cm Hz}$ in the case of $W_{thickness} = 5\text{ mm}$ and $110\text{ }^{\circ}\text{C}/\text{cm Hz}$ in the case of $W_{thickness} = 10\text{ mm}$.

However, as in the greatest part of the engineering problems, also this result has to be considered as just one of all the complicated and interconnected aspects of the whole problem. In fact, so far only the thermal problem has been tackled neglecting the mechanical aspects. In the next section, a more complicated 3D model will be presented, developing a thermo-mechanical analysis suitable to show the influence of a time-varying thermal field (due to the strike point-sweeping) on the mechanical behavior of the DEMO divertor.

6.3 Strike-point sweeping 3D thermo-mechanical analysis

6.3.1 Model assumptions

An “optimized” ITER-like Water Cooled Divertor Target for the DEMO-relevant operational conditions [6.10] has been considered. The target consists of a number of rectangular monoblocks of tungsten (W) armour, connected by a cooling tube, having a thickness of 4 mm with a gap of 0.25 mm between two neighbouring monoblocks (**Figure 6.4**). A soft-copper (Cu) interlayer between the armour and the copper alloy (CuCrZr-IG) pipe was also considered to reduce the thermal stresses caused by the mismatch of thermal expansion coefficients between W and CuCrZr alloy. The dimensions considered are the following:

- a) Tube inner diameter \rightarrow 12 mm

- b) Tube thickness \rightarrow 1 mm
- c) Interlayer thickness \rightarrow 1 mm
- d) Armour side thickness \rightarrow 2.5 mm

The thickness of the armour to the plasma-facing side has been assumed 5 mm, which was derived from the erosion rate and required lifetime whereas the minimum thickness to the bottom side has been fixed to 2.5 mm considering the technical limitation in fabrication [6.10].

Only one monoblock (whose choice will be discussed later) has been considered and in particular, assuming the symmetry² of both the tile geometry and the boundary conditions, only one quarter of the monoblock has been modelled (**Figure 6.21**) reducing the mesh size and hence the calculation time.

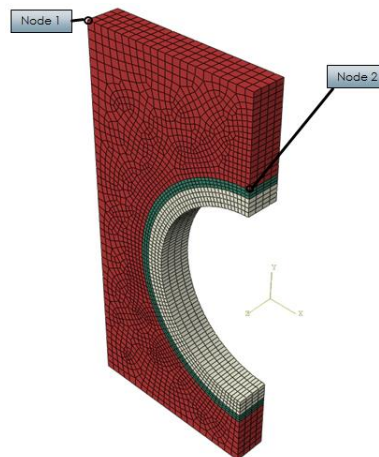


Figure 6.21: The FE mesh of the mono-block divertor model. Due to symmetry hypothesis, only one quarter of the structure has been considered.

The commercial FEM code ABAQUS[®] was employed for the numerical studies.

The thermo-mechanical simulations are based on data of several materials in the PFC model. Cross-rolled and stress-relieved tungsten was applied for the tungsten armour block. A precipitation-hardened

² The footprint of the heat flux power, and hence the upper boundary condition, is not symmetric along the thickness (z-axis) of the tile (**Figure 6.22**) but, due to the tile small thickness, the heat flux could be assumed spatially constant along the z-axis in a single tile.

copper alloy (CuCrZr) was considered for the heat sink tube and soft-annealed copper constituted the interlayer [6.11]. The Frederick-Armstrong constitutive model applied for both copper and copper alloy is based on the combination of non-linear isotropic and kinematic hardening laws [6.12]. Temperature-dependent material properties are listed in **Table 6-II** at selected temperatures, corresponding to the operation temperatures for the considered materials. It should be noted that the materials are assumed to be unirradiated due to lack of data of irradiated materials [6.13].

Table 6-II: Properties of the considered materials at selected temperatures [6.13]

	Tungsten ¹			CuCrZr ²		Copper ³	
	20 °C	400 °C	1200 °C	20 °C	400 °C	20 °C	400 °C
Young's modulus (GPa)	398	393	356	115	106	115	95
Yield stress (MPa)	1385	1100	346	273	238	3	3
Q^* (MPa)				-43	-68	76	36
b^*				6	10	8	25
C^* (MPa)				148575	117500	64257	31461
γ^*				930	1023	888	952
Heat conductivity (W/mK)	175	140	105	318	347	379	352
Coefficient of thermal expansion ($10^{-6}/K$)	4.5	4.6	5.3	16.7	17.8	17.8	18.1

¹ Rolled and stress-relieved state.

² Precipitation-hardened state, the reference alloy: Elmedur-X (code: CuCr1Zr, Cr: 0.8%, Zr: 0.08%).

³ Softened by annealing at 700 °C for 1 h.

* Material parameters entering the Frederick-Armstrong constitutive model [13].

Figure 6.22 shows the assumed footprint of the heat flux power impinging on the outer target according to the latest prediction for DEMO based on [6.14].

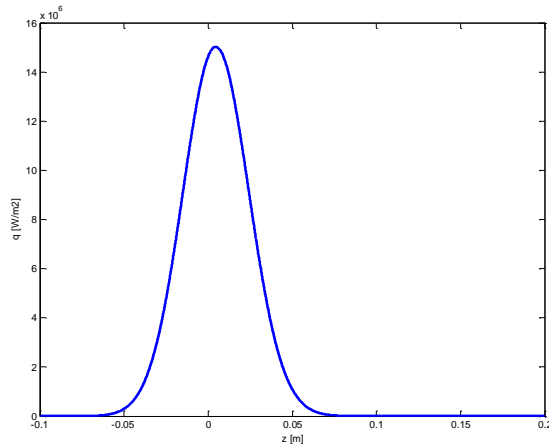


Figure 6.22: The assumed footprint of the heat flux power on the outer target (according to [6.14]).

To study the influence of periodic strike point oscillation, the footprint of the heat flux power is swept at the surface of the target along the axial direction of the cooling tube (z-axis), see **Figure 6.21**. The heat flux profile is assumed to be uniform along the x-axis and z-axis³, and therefore only one quarter of the structure has been considered in this analysis.

Moreover, the sweeping amplitude is defined as the distance between the rightmost and leftmost positions of a control point during sweeping. The position where the maximum temperature occurs during sweeping in the whole divertor target is dependent on the two sweeping parameters: amplitude and frequency. That position, in which the maximum temperature is reached in the target during the phenomenon, and therefore the position of the single divertor mono-block selected for the analysis, is evaluated, for each sweeping case, with the MATLAB® 2D approximated FE model illustrated in Section 6.2, slightly modified in order to take into account also the soft-copper interlayer **Figure 6.23**.

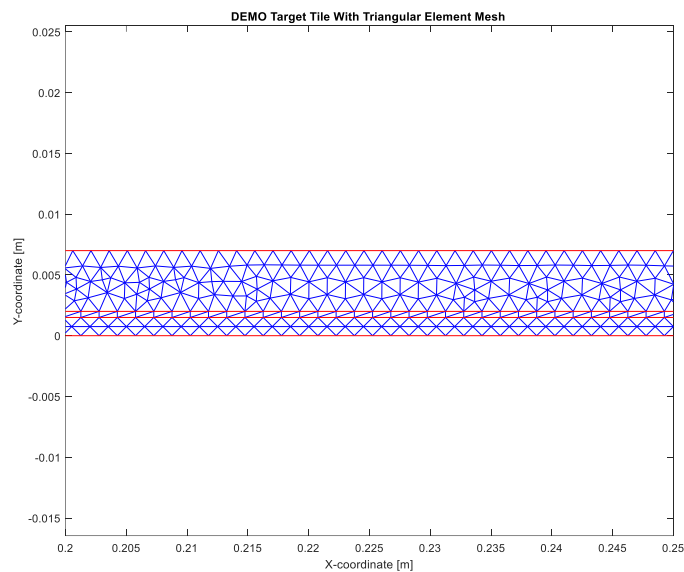


Figure 6.23: MATLAB triangular mesh (zoom) modeling the W (upper), the Cu-alloy (lower) and the soft-Cu (intermediate) layers

³ This approximation is probably the most inaccurate, but it was necessary considering the calculation time needed by the available machine.

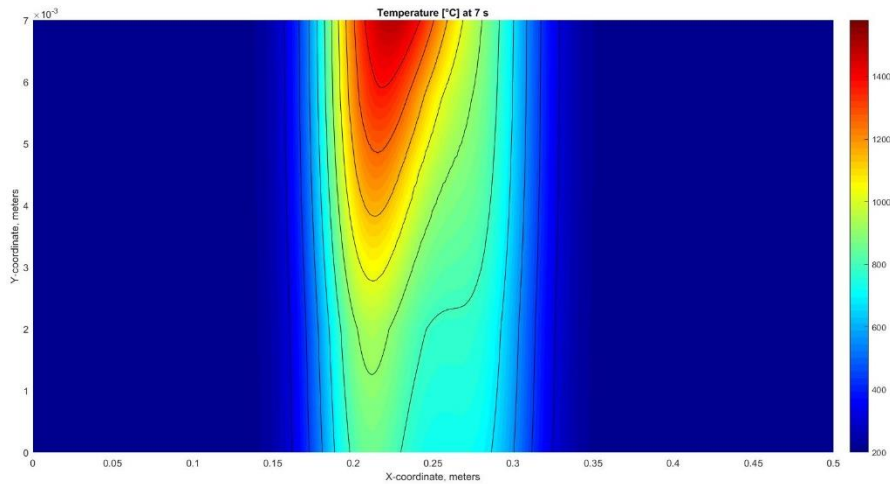


Figure 6.24: Example of the MATLAB 2D FE model thermal analysis.

Once the position where the maximum temperature is reached in the whole target during the phenomenon has been evaluated starting from the results of the 2D thermal analysis (**Figure 6.24**), the (a-dimensional) heat flux time evolution in the correspondent tile is evaluated with a MATLAB® routine (see **Figure 6.25**). Through this procedure, it is possible for each case (given by the combination of the different strike-point sweeping parameters) to determine and hence analyse the tile of the target which reaches the maximum temperature during the phenomenon.

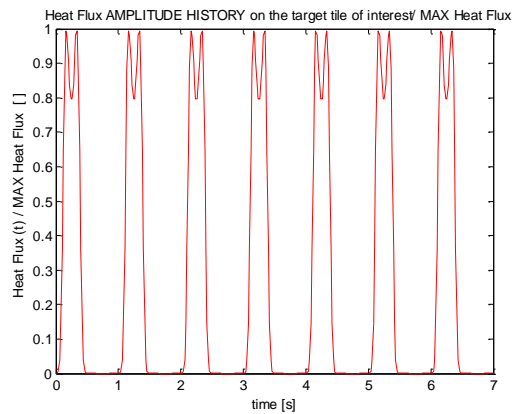


Figure 6.25: A-dimensional heat flux amplitude history evaluated in the position where the maximum temperature occurs during sweeping.

The peak heat flux densities of 15MW/m^2 and 30MW/m^2 are applied in this study. Before the high heat flux (HHF) load is applied, the PFC is assumed to have a uniform temperature of 200°C (coolant temperature) without any residual stress. For a parametric study, the sweeping amplitudes of 5 cm and 20 cm have been chosen. The sweeping frequency values of 0.5 Hz and 1 Hz were also considered.

The heat transfer coefficient between the inner wall of the heat sink tube and the coolant water is plotted in **Figure 6.26**, as a function of the wall temperature. The coolant water velocity and pressure in the pipe are respectively 12 m/s and 5MPa whereas the temperature is assumed 200°C .

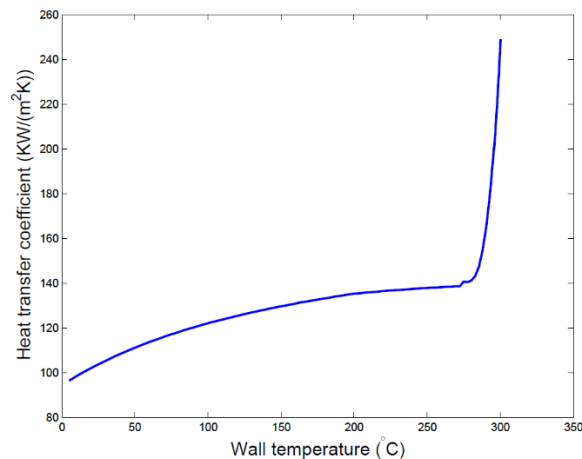


Figure 6.26: Heat transfer coefficient between the inner wall of the heat sink tube and the coolant water. The coolant water velocity is 12 m/s. Pressure of the coolant water is 5MPa. The temperature of the coolant water is 200°C [6.16].

At the end of the cooling pipe, a planar axial displacement constraint⁴ is given.

For the remaining surfaces at the front and at the right sides of the tile, a symmetry boundary condition has been considered. Furthermore, in order to avoid a rigid body displacement, the point on the symmetry plane at the tile bottom surface (**Figure 6.21**) has been considered as embedded.

⁴ A conservative assumption has been made correlating the planar axial displacement of the left tile surface to the displacement of the lowest (and therefore the coolest) point in the cooling pipe (in the upper part).

6.3.2 Thermo-mechanical analysis

In order to appreciate the advantages achievable in terms of maximum temperature reduction with the strike point sweeping technique, the results of the simulations in the strike point sweeping cases are compared to the results obtained in a stationary case (assumed as reference).

The nodes 1 and 2 at the left edge (see **Figure 6.21**) are selected to characterize, respectively, the maximum temperatures in the tungsten block and between tungsten and copper in the sweeping cases.

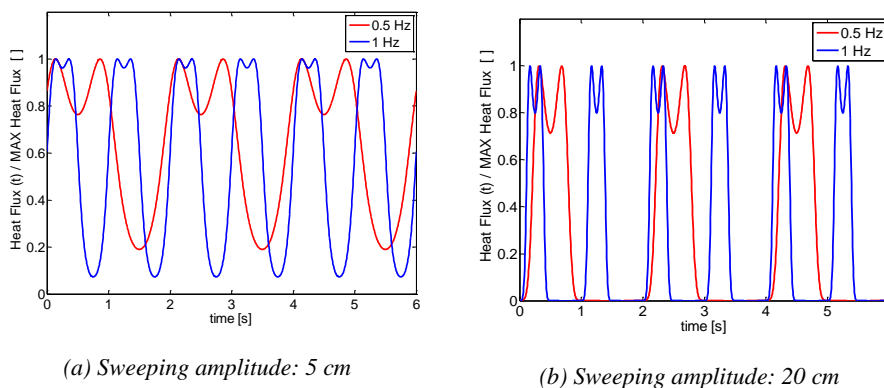


Figure 6.27: Heat flux density/MAX heat flux density at node 1 as a function of time for different sweeping amplitudes and frequencies.

In **Figure 6.27**, the a-dimensional heat flux density is shown as a function of time for different sweeping amplitudes and frequencies. A higher sweeping frequency leads more thermal cycles within the same time but less loading time for each thermal cycle. Increasing the sweeping amplitude results in spreading the energy in a larger area, i.e. the energy input is reduced for each mono-block [6.13].

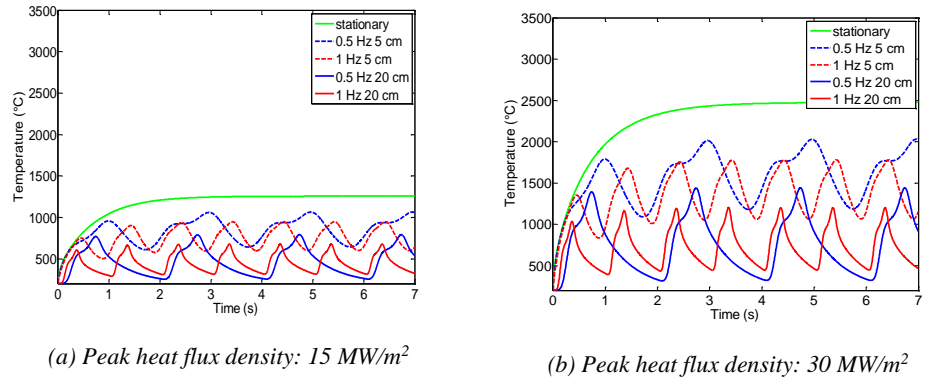


Figure 6.28: Temperature at node 1 as a function of time for different peak heat flux densities.

Figure 6.28 shows the temperature at node 1 for peak heat flux densities of 15MW/m^2 (a) and 30MW/m^2 (b). The temperature is much higher for a sweeping amplitude of 5 cm than 20 cm. Furthermore, when the sweeping frequency increases, the peak temperature decreases.

According to the results analyzed in Section 6.2, the peak temperature at the top surface of the mono-block can be reduced by increasing either the sweeping amplitude or the sweeping frequency. However, the sweeping amplitude increase will be limited by the geometry of divertor target. A higher sweeping frequency will require more thermal cycles during the operation, but at the same time, it reduces the temperature variation as well as the loading time in each thermal cycle [6.13] enlarging the allowed number of load cycles (fatigue lifetime). The study of impact of increasing sweeping frequency on Low Cycle Fatigue (LCF) behavior will be shown later in this section.

Table 6-III gives maximum and minimum temperatures at node 1 in the saturating thermal cycle. In the 5 cm sweeping amplitude case, when the sweeping frequency increases from 0.5 to 1Hz, both the maximum temperature and the minimum temperature decrease.

Table 6-III: Maximum/ Minimum (amplitude) temperatures [$^{\circ}\text{C}$] at node 1 in the saturating thermal cycle.

Sweeping amplitude (cm)		5		20	
Sweeping frequency (Hz)		0.5	1	0.5	1
Peak heat flux density (MW/m^2)	15	1064/643 (421)	948/599 (349)	790/256 (534)	677/314 (363)
	30	2029/1186 (843)	1782/1065 (717)	1442/321 (1121)	1203/446 (757)

As a result, the temperature amplitudes decreases more than 15%. When the sweeping amplitude of 20 cm is applied instead of 5 cm, increasing the frequency from 0.5 Hz to 1 Hz the reduction in the temperature variation amplitude is more than 40%. For the peak heat flux density of $30\text{MW}/\text{m}^2$, the maximum temperatures are above the crystallization temperature of tungsten ($1100\text{-}1400^{\circ}\text{C}$) [6.13]. When tungsten at the surface layer is recrystallized, the strength of tungsten is significantly reduced, and major cracks have been observed in the heat flux tests of divertors [6.15]. Even when the sweeping amplitude of 20 cm is applied, the peak temperatures will not be kept below the recrystallization temperature of tungsten.

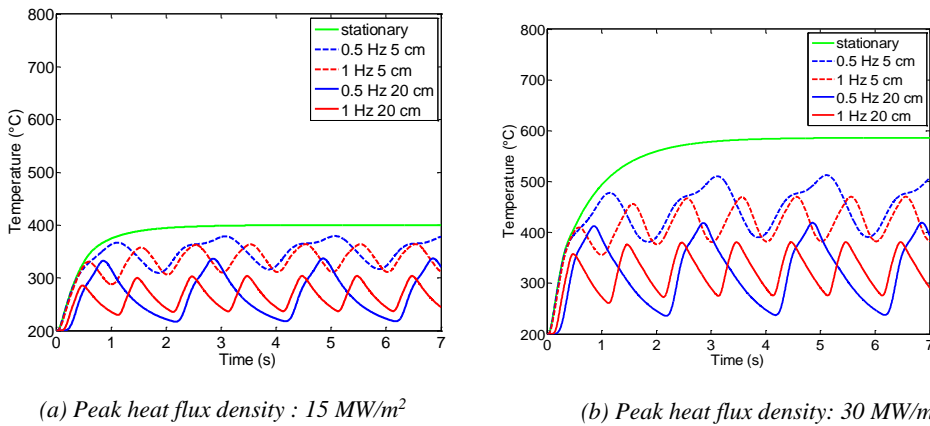


Figure 6.29: Temperature at node 2 as a function of time.

Figure 6.29 shows the temperature at node 2 for peak heat flux densities of $15\text{MW}/\text{m}^2$ (a) and $30\text{MW}/\text{m}^2$ (b). The impact of the sweeping

amplitude and the sweeping frequency on the temperature is similar. By applying a sweeping amplitude of 20 cm for the peak heat flux density of up to 30MW/m^2 , there is possible a maximum temperature reduction in the saturating thermal cycle below 420°C . The high temperature (above 400°C) is critical at the interface between tungsten armor block and copper interlayer, as the copper will become softer. Maximum and minimum temperatures at node 2 are listed in **Table 6-IV**.

Table 6-IV: Maximum / Minimum (amplitude) temperatures ($^\circ\text{C}$) at node 2 in the saturating thermal cycle.

Sweeping amplitude (cm)		5		20	
		0.5	1	0.5	1
Peak heat flux density (MW/m^2)	15	379/317 (62)	364/311 (53)	337/218 (119)	303/237 (66)
	30	513/391 (122)	470/382 (88)	419/237 (182)	381/276 (105)

Compared to the situation at the top surface, the temperature variation at node 2 is less significant and its amplitude is less than 20% of that at node 1. However, the temperature variation in the copper interlayer is more critical, since a large amount of plastic deformation will be generated due to the temperature variation leading to LCF failure [6.16]. Different from the trend at the top surface, the temperature amplitude increases if the sweeping amplitude grows from 5 cm to 20 cm [6.13].

Due to the high yield stress of tungsten, there is no plastic deformation generated in the tungsten block during HHF loading, while the interlayer is expected to experience severe incremental plastic straining due to the low yield stress of copper. As shown in a previous study [6.16], significant plastic deformation accumulation occurs in the interlayer, while nearly no cyclic plastic deformation is accumulated in the cooling tube [6.13]. Therefore, in the following the impact of sweeping parameters on the equivalent total strain in the copper interlayer (the reference node is chosen in the middle of the interlayer at the plane of symmetry) will be analysed.

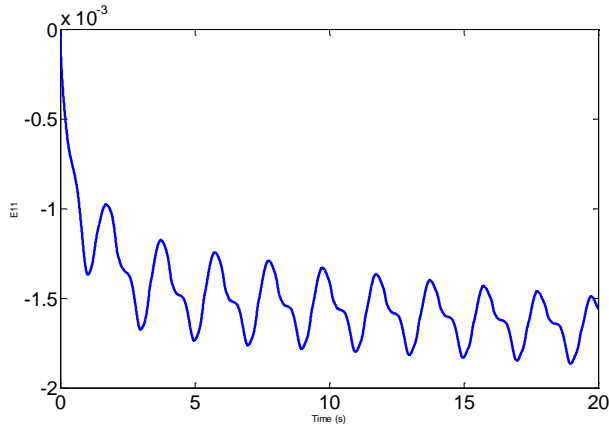
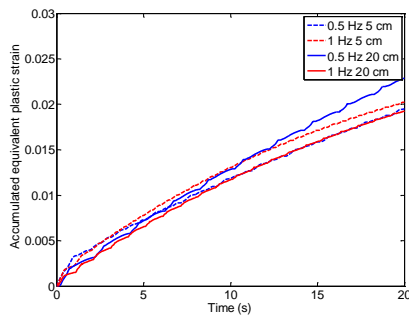
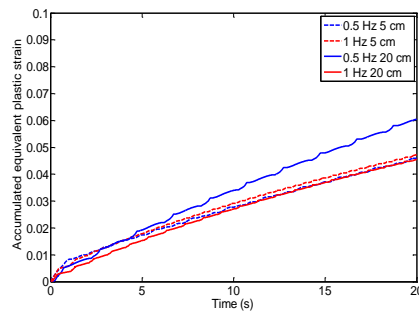


Figure 6.30: Evolution of E_{11} deformation component at the reference position.

Figure 6.30 shows the evolution of the E_{xx} deformation component. All the deformation components show a cyclic variation saturating after about 20 s in the interlayer. Moreover, the plastic strain evolution in the interlayer, whose behavior has been taken into account considering the equivalent plastic strain parameter⁵ (PEEQ [6.17]), clearly indicates a LCF situation with saturation amplitudes (no ratchetting).



(a) Peak heat flux density: 15 MW/m^2



(b) Peak heat flux density: 30 MW/m^2

Figure 6.31: Accumulated equivalent plastic strain in the copper interlayer.

⁵ The equivalent plastic strain parameter, which is a direct output of the ABAQUS® simulation, has also been taken into account in order to compare the presents results with the others obtained in previous studies (i.e. [6.13]).

Most of the LCF data in the literature are obtained from uni-axial cyclic loading tests. The interlayer in the divertor target is loaded by multi-axial stresses. Thus, for the assessment of the LCF lifetime, the multi-axial plastic strain data must be converted into scalar values so that the simulation results can be directly compared with the measured data. To this end, the equivalent strain range $\overline{\Delta\varepsilon}$ is used [6.11].

In the ITER SDC-IC [6.11], the experimental fatigue data are fitted using the strain-life equation that relates the cycles to failure to the applied strain range. The contributing factors are separated into an elastic strain, or high cycle fatigue, component and a plastic strain, or low cycle fatigue, component. This strain-life relation is given as:

$$\Delta\varepsilon_t = 49.89N_f^{-0.57} + 0.40N_f^{-0.75}$$

where $\Delta\varepsilon_t$ is the total strain range, N (N_f) is the number of cycles to failure.

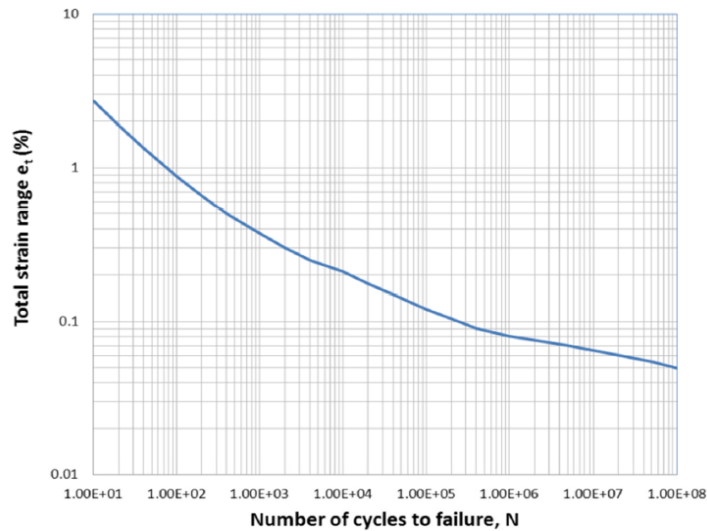


Figure 6.32: Recommended fatigue design curve for the unirradiated pure copper: total strain range e_t (%) as a function of number of allowable cycles (N) in the temperature range of 20 – 300°C

A design fatigue curve for unirradiated pure annealed copper was deduced from the fitted strain-life relation by offsetting the fit by a factor of 20 in number of cycles to failure or offsetting the fit by a factor of 2 in total strain range, whatever is the most conservative. **Figure 6.32**

shows the resulting fatigue design curve for the unirradiated pure copper (interlayer) used in our analysis.

Figure 6.33 shows how the total strain range ($\Delta\varepsilon_t$) and the number of cycles to failure (N) of the interlayer have been evaluated with a MATLAB[®] routine.

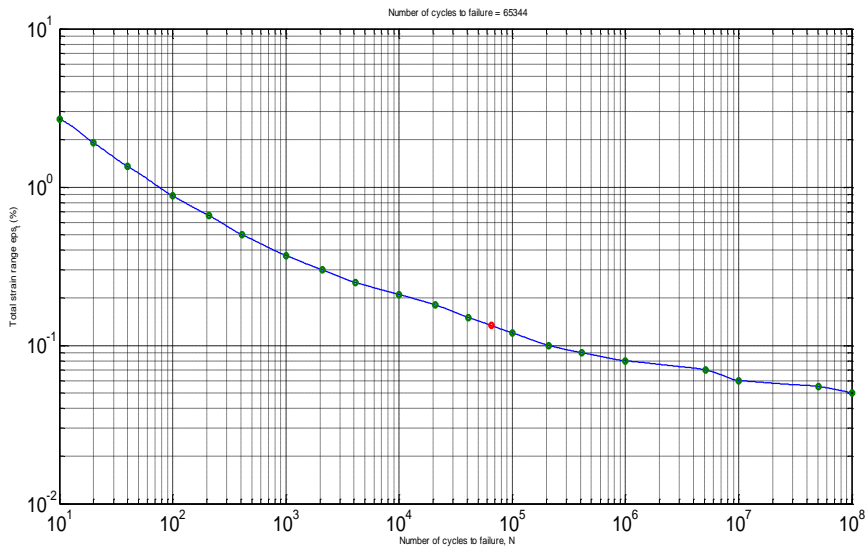


Figure 6.33: Example of the evaluation of $\Delta\varepsilon_t$ and N (15MW/m², 5 cm and 0.5 Hz case).

Table 6-V lists the equivalent strain range at the last thermal cycle and the fatigue lifetime of the interlayer.

Table 6-V: Equivalent strain range (%) / fatigue lifetime (N) in the copper interlayer.

Sweeping amplitude (cm)		5		20	
		0.5	1	0.5	1
Peak heat flux density (MW/m ²)	15	0.13/65344	0.09/356612	0.19/16518	0.10/189324
	30	0.32/1682	0.20/11908	0.45/564	0.22/8508

The fatigue lifetime decreases as the peak flux densities increase. A greater fatigue lifetime is predicted if the sweeping amplitude decreases from 20 cm to 5 cm. If the sweeping frequency is doubled (from 0.5 Hz

to 1 Hz), the fatigue lifetime is increased at least by a factor of 5. Therefore, increasing the sweeping frequency from 0.5 Hz to 1 Hz will increase the actual operating time for the interlayer.

From the results (**Table 6-V**) it is evident that even in the best case scenario (15 MW/m², with 5cm and 1 Hz sweeping parameters), the fatigue lifetime of the copper interlayer, in stationary sweeping conditions, is less than 100 working hours. Moreover, although the strike point sweeping appears a promising technique as an emergency control action, it could be interesting to study the possibility that even after a certain damage degree, the interlayer keeps working properly in reducing the thermal stresses and conducting the heat. After that, further investigations should be necessary to evaluate the fatigue lifetime of the cooling pipe.

6.4 DEMO DN wobbling: a preliminary analysis

Plasma vertical oscillations in tokamaks arise for two main reasons [6.18]:

1. Control of the vertical unstable mode:

- Control strategy

(In JET, for example, the vertical feedback controller can be roughly described as a bang-bang controller with hysteresis that may suffer of oscillations around the target point in case of coupling with the shape controller [6.19]);

- Delays and Measurement noise in the controller quantities

(They cause a multi-frequency movement of the plasma vertical position around the target point);

2. Active wobbling

- Induced oscillation to reduce the power load on the divertor structures.

Active wobbling can be implemented imposing a square wave on the vertical control system. However, it is important to evaluate the

possible frequencies, amplitudes and power requests on the vertical control system.

A preliminary analysis [6.18] has been performed on DEMO focusing on the DN configuration with $k_{95\%} = 1.59$ and $\delta_{95\%} = 0.33$ (already shown in Section 5.4.4) and imposing a square control signal on the imbalance circuit P2-P5.

In particular, the linearized model of the plasma (containing also the passive structures) has been firstly considered in order to evaluate, in open-loop, possible frequencies and amplitudes of the control signal. Indeed:

- the amplitude v [V] of the control signal has been compared to the minimum voltage v_{min} needed to control a VDE of 5cm⁶:

$$\frac{v}{v_{min}} = [0.25 \ 0.5 \ 1 \ 2]$$

- the frequency f [Hz] of the square control signal has been compared to the plasma growth rate γ :

$$\frac{f}{\gamma} = [0.25 \ 0.5 \ 1]$$

Table 6-VI shows the amplitude of the plasma current centroid oscillations in *cm* as a function of frequency f/γ and voltage v/v_{min} .

Table 6-VI: Amplitude of the plasma centroid oscillations in cm as a function of frequency f/γ and voltage v/v_{min} .

f/γ v/v_{min}	0.25	0.5	1.0
0.25	0.8	0.2	0.04
0.5	1.7	0.4	0.06
1.0	3.3	0.8	0.1
2.0	6.6	1.5	0.2

In order to verify the effectiveness of the analysis and to implement a preliminary closed-loop strategy on the non-linear simulations, a focus

⁶ According to the definition of “best achievable performance” given in Chapter 1.

on the case $v/v_{min} = 2$ and $f/\gamma = 0.5$ is illustrated. For the reference DN configuration with $k_{95\%} = 1.59$ and $\delta_{95\%} = 0.33$ having $v_{min} = 17 V$ and $\gamma = 4.14 s^{-1}$, it results $v = 34 V$ and $f \approx 2 Hz$. **Figure 6.34** and **Figure 6.35** show the plasma current centroid vertical position and velocity at regime in open loop given by the linearized model.

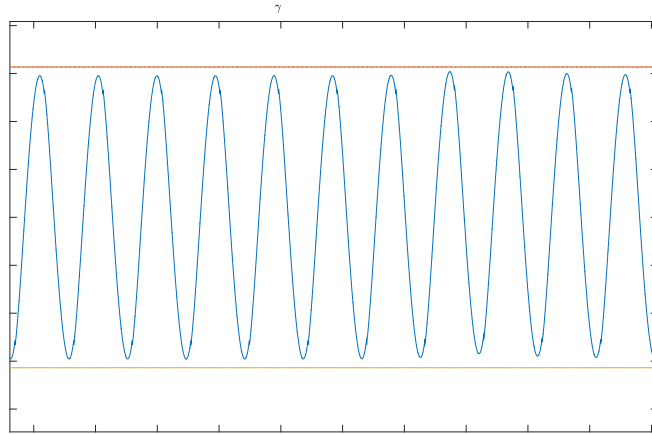


Figure 6.34: Plasma current centroid vertical position at regime in open loop given by the linearized model assuming on the imbalance circuit $v = 34V$ and $f \approx 2Hz$.

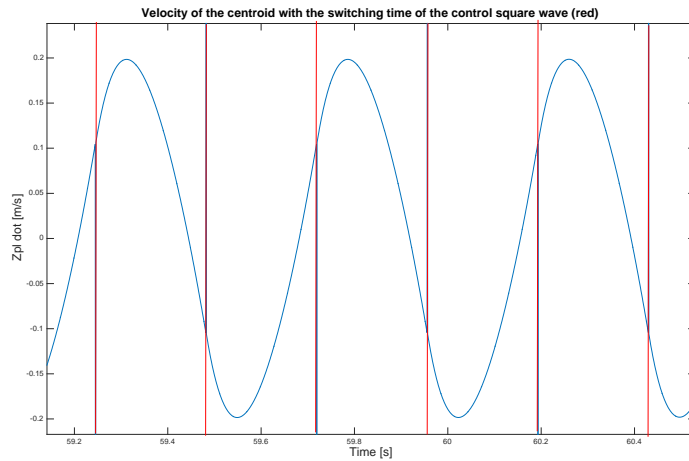


Figure 6.35: Plasma current centroid vertical velocity at regime in open loop given by the linearized model assuming on the imbalance circuit $v = 34V$ and $f \approx 2Hz$.

It can be noted from **Figure 6.34** and **Figure 6.35** that the plasma vertical position reaches its maximum (minimum) when the velocity is around -0.1 ms^{-1} (0.1 ms^{-1}). This information can be used to implement a preliminary closed loop control law on the imbalance circuit.

In particular, a closed loop non-linear simulation imposing a bang-bang controller on the imbalance circuit with a $v = 2v_{min} = 34 \text{ V}$ voltage and a switching condition given by the 0.1 ms^{-1} threshold of the plasma current centroid vertical velocity (**Figure 6.36**) has been performed.

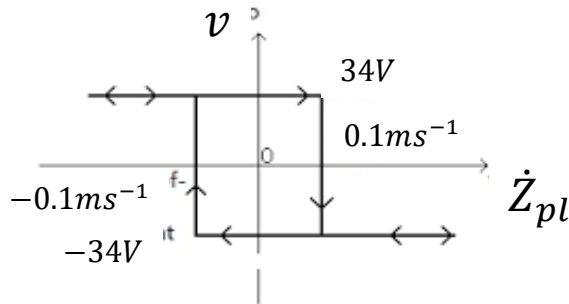


Figure 6.36: Closed loop bang-bang controller with hysteresis implemented on the imbalance circuit.

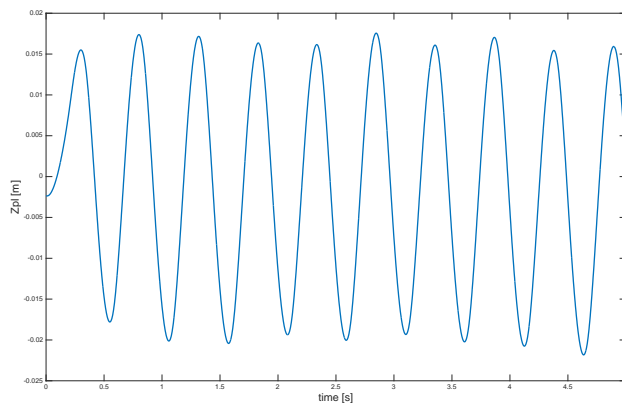


Figure 6.37: Plasma centroid vertical position in closed loop given by the nonlinear simulation model.

Figure 6.37 shows the vertical position of the plasma centroid applying the bang-bang controller. The oscillations of the plasma vertical position have a period of about 0.5 s, as predicted by the linearized model.

Finally, **Figure 6.38** shows the plasma separatrices at the minimum and maximum value of the plasma current centroid vertical oscillations.

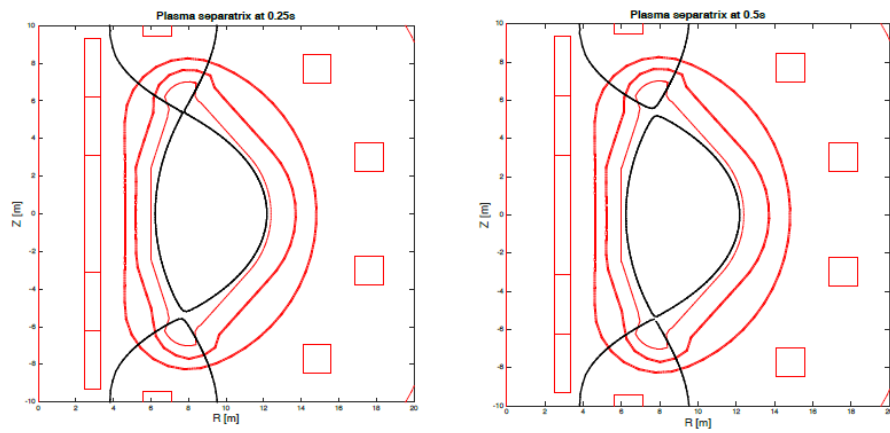


Figure 6.38: Plasma separatrices at the minimum and maximum value of the plasma centroid vertical oscillations

The advantage of the wobbling technique applied to the DN plasma configuration is clear observing **Figure 6.38**: the periodical vertical oscillation imposed to the plasma allows to activate in turn upper and lower X-point. Therefore, in a certain period of time the heat load reaching each Divertor (upper and lower) is the half.

6.5 Final considerations and further developments

The present Chapter introduces the strike-point sweeping technique. This technique resorts to a periodical movement of the plasma strike-point sweeping spreading the thermal load reaching the tokamak divertor region. After a brief description of the method used to perform the strike-point sweeping in experimental machines, the results of a

preliminary assessment of the sweeping power requirements and AC losses for a demonstration fusion reactor (DEMO) is presented.

The main contribution in this Chapter deals with the thermal loading of divertor tiles, and the stresses that develop therein during varying thermal loading due to strike-point sweeping. 2D and 3D FE formulations of the model for the loading of the tiles are presented.

In the 2D case, using a model of lines approach, the system is described as a set of ODEs. A simplified thermal analysis is therefore performed in order to assess the advantages, in terms of maximum temperature reduction, achievable resorting to the strike-point sweeping technique.

A 3D model of the DEMO target tiles is then presented. The periodical heating and cooling of the plasma facing components, in fact, induces the thermal-fatigue phenomenon. The 3D model was, therefore, necessary to investigate more in detail the thermal field and to sequentially evaluate the thermal fatigue of the component.

Finally, a preliminary analysis on the wobbling technique, in which not only the plasma strike-points but all the plasma boundary is periodically moved, applied to a DEMO Double Null plasma magnetic configuration is presented.

The fatigue lifetime of the divertor copper interlayer seems to be, at least for the range of sweeping parameters taken into account in the proposed thermo-mechanical analysis, the limiting factor investigating the strike point sweeping as the ultimate solution in the mitigation of the DEMO power exhaust. Therefore, although the strike point sweeping technique could not be used for the whole pulse length, it can be exploited as an emergency tool in case of unforeseen increase of the heat-flux on the divertor target.

Based on the 3D models proposed in the Section 6.3, further studies have been carried out for different strike-point sweeping parameters [6.5]. For the same cases presented here (sweeping amplitude of 5 cm and 20 cm - sweeping frequency 0.5 Hz and 1 Hz), the best case scenario provides a fatigue lifetime of the copper interlayer, in stationary sweeping conditions, of more than 200 working hours. The increased fatigue lifetime of the copper interlayer in [6.5], more than the double of the result presented in this thesis (100 hours), is probably due to less-conservative assumptions. Based on these assumptions, further analyses [6.5] show that increasing the sweeping frequency up to 4 Hz, with 20 cm amplitude, the predicted fatigue lifetime is 13,812

h. This result is not surprising since an increased frequency involves a reduced difference of temperature, which is the main factor governing the thermal-fatigue phenomenon, and hence remarkable benefits on the target tiles fatigue lifetime. These results may allow considering the sweeping as a steady state control scheme. However, further analyses are necessary to investigate the possibility to reach such frequency with DEMO external coils or, conversely, if it is necessary to design dedicated in-vessel coils (compatibly with the shielding and maintenance constraints).

Moreover, these results, in terms of frequency and amplitude parameters, may represent a starting point also for applying the wobbling technique to a DEMO alternative magnetic configuration, i.e. the Double Null, constituting a candidate solution for the power-exhaust issue.

References

- [6.1] G. Ambrosino, et al. “Plasma Strike-Point Sweeping on JET Tokamak With the eXtreme Shape Controller”, IEEE TRANSACTIONS ON PLASMA SCIENCE, VOL. 36, NO. 3, JUNE 2008
- [6.2] F. Villone and contributors to the EFDA-JET Workprogramme, “A model-based strike point sweeping technique applied to JET”, Plasma Phys. Control. Fusion 46 (2004) 1375–1392
- [6.3] R. Albanese, R. Ambrosino, M. Mattei, “Final Report on Strike point sweeping with internal coils in DEMO”, August 2014, <https://idm.euro-fusion.org/>, EFDA_D_2M8NV8
- [6.4] R. Albanese, et al., The linearized CREATE-L plasma response model for the control of current, position and shape in tokamaks, Nucl. Fusion 38 (1998) 723–738.
- [6.5] F. Maviglia, [...], V. P. Loschiavo, et al., “Limitations of transient power loads on DEMO and analysis of mitigation techniques”, Fusion Engineering and Design 109–111 (2016) 1067–1071
- [6.6] <https://euro-fusion.org/newsletter/handling-extreme-temperature-gradients>
- [6.7] Eich T., et al. “Inter-ELM Power Decay Length for JET and ASDEX Upgrade: Measurement and Comparison with Heuristic Drift-Based Model”, PRL 107, 215001 (2011)
- [6.8] G. Federici et al., “Assessment of erosion of the ITER divertor targets during type I ELMs”, Plasma Phys. Control. Fusion 45 (2003) 1523–1547
- [6.9] E. N. Sarmin; L. A. Chudov (1963), “On the stability of the numerical integration of systems of ordinary differential equations arising in the use of the straight line method”, USSR Computational Mathematics and Mathematical Physics, 3 (6), pp. 1537–1543, doi:10.1016/0041-5553(63)90256-8
- [6.10] F. Crescenzi, et al, “Design study of ITER-like divertor target for DEMO”, Fusion Engineering and Design, Volumes 98–99, October 2015, Pages 1263–1266
- [6.11] “ITER STRUCTURAL DESIGN CRITERIA FOR IN-VESSEL COMPONENTS (SDC-IC) - APPENDIX A”, V.3.3, G 74 MA 8 01-05-28 W 0.2

- [6.12] J. H. You, M. Miskiewicz, “Materials parameters of copper and CuCrZr alloy for cyclic plasticity at elevated temperatures” *Journal of Nuclear Materials*, Volume 373, Issues 1–3, 15 February 2008, Pages 269–274
- [6.13] Muyuan Li, et al., “Sweeping Heat Flux Loads on Divertor Targets: Thermal Benefits and Structural Impacts”, *Fusion Engineering and Design* 102 (2016) 50 – 58.
- [6.14] T. Eich, et al, 2013 *Nucl. Fusion* 53 093031
- [6.15] G. Pintsuk, I. Bobin-Vastra, S. Constans, P. Gavila, M. Rödiger, B. Riccardi, “Qualification and post-mortem characterization of tungsten mock-ups exposed to cyclic high heat flux loading”, *Fusion Engineering and Design* 88 (2013) 1858 – 1861.
- [6.16] M. Li, E. Werner, J.-H. You, “Low cycle fatigue behavior of ITER-like divertor target under demo-relevant operation conditions”, *Fusion Engineering and Design* 90 (2015) 88–96
- [6.17] *Abaqus Analysis User’s Manual 6.12*, Dassault Systèmes Simulia Corp., Providence, RI, USA, 2012.
- [6.18] R. Albanese, R. Ambrosino, V. P. Loschiavo, M. Mattei, “Final Report on DEMO Vertical Stability investigations described in the task specification”, December 2016, <https://idm.euro-fusion.org/>, EFDA_D_2MP7Z8
- [6.19] F. Sartori, R. Albanese, et. Al., “JET Operations and Plasma Control”, EFDA–JET–CP(09)03/03